Ludwig-Maximilians-Universität München

Coherent Phonons and Polaronic Effects in Bismuth Oxyiodide Nanoplatelets

Sebastian Rieger

München, 2022

Coherent Phonons and Polaronic Effects in Bismuth Oxyiodide Nanoplatelets

Dissertation to obtain the
doctoral degree of natural sciences (Dr. rer. nat.)

at the Faculty of Physics of the
Ludwig-Maximilians-Universität München

submitted by
Sebastian Rieger
from Munich

Munich, 27 April 2022

Doctoral committee

First referee:	Prof. Dr. Jochen Feldmann
Second referee:	Prof. Dr. Alexander Urban
Chairman:	Prof. Dr. Jan von Delft
Further meber:	Prof. Dr. Thomas Weitz
Date of the oral exam:	05 July 2022

Kohärente Phononen und Polaronische Effekte in Bismut Oxyiodid Nanoplättchen

Dissertation zur Erlangung des
Doktorgrades der Naturwissenschaften (Dr. rer. nat.)

an der Fakultät für Physik der
Ludwig-Maximilians-Universität München

vorgelegt von
Sebastian Rieger
aus München

München, 27. April 2022

Promotionskommission

Erstgutachter:	Prof. Dr. Jochen Feldmann
Zweitgutachter:	Prof. Dr. Alexander Urban
Vorsitzender:	Prof. Dr. Jan von Delft
Weiteres Mitglied:	Prof. Dr. Thomas Weitz
Tag der mündlichen Prüfung:	05. Juli 2022

dedicated to my parents

Publications, Conferences and Awards

Scientific Publications of Results Presented in This Work

- S. Rieger, T. Fürmann, J. K. Stolarczyk, and J. Feldmann
  Optically Induced Coherent Phonons in Bismuth Oxyiodide (BiOI) Nanoplatelets
  Nano Letters 21.18: 7887 (2021)

- S. Rieger, S. Schönweitz, K. Frank, T. Fürmann, N. M. Kerschbaumer, V. Steidl, J. Fang, M. Döblinger, B. Nickel, J. K. Stolarczyk, and J. Feldmann
  Anisotropic polarons and self-trapping in bismuth oxyiodide (BiOI) nanoplatelets
  ACS Nano, under review

Additional Publications of my Time as a PhD Candidate

- S. Rieger, B. J. Bohn, M. Döblinger, A. F. Richter, Y. Tong, K. Wang, P. Müller-Buschbaum, L. Polavarapu, L. Leppert, J. K. Stolarczyk, and J. Feldmann
  Excitons and narrow bands determine the optical properties of cesium bismuth halides
  Physical Review B 100.20: 201404 (2019)

- B. Charles, M. T. Weller, S. Rieger, L. E. Hatcher, P. F. Henry, J. Feldmann, D. Wolverson, and C. C. Wilson
  Phase Behavior and Substitution Limit of Mixed Cesium-Formamidinium Lead Triiodide Perovskites
  Chemistry of Materials 32.6: 2282 (2020)

- M. Kurashvili, I. Polishchuk, A. Lang, S. Strohmair, A. F. Richter, S. Rieger, T. Debnath, B. Pokroy, and J. Feldmann
  Disorder and Confinement Effects to Tune the Optical Properties of Amino Acid Doped Cu_2O Crystals
  Advanced Functional Materials 32: 2202121 (2022)

- N. M. Kerschbaumer, L. Fochler, M. Reichenspurner, S. Rieger, M. Fedoruk, T. Lohmüller, and J. Feldmann
  Twisted light interferometer for high precision refractive index measurements
  Optics Express, accepted (2022)

- A. Barfüßer, S. Rieger, A. Dey, A. Tosun, Q. A. Akkerman, T. Debnath, and J. Feldmann
  Wannier excitons and biexcitons in spherical-like halide perovskite quantum dots
  Nano Letters, under review

Conferences and Workshops

- **34th International Conference on the Physics of Semiconductors** (Talk)
  Montpellier, France, 07-08/2018

- **4th International Conference on Perovskite Solar Cells and Optoelectronics** (Poster)
  Lausanne, Switzerland, 09-10/2018

- **7th SolTech Conference** (Poster)
  Würzburg, Germany, 10/2018

- **Workshop on Optical Spectroscopy of New Materials** (Talk)
  Haigerloch, Germany, 03/2019

- **DPG Summer School - Exciting Nanostructures: Characterizing Advanced Confined Systems** (Poster)
  Bad Honnef, Germany, 07/2019

- **e-conversion Conference** (Poster)
  Venice, Italy, 09/2019

- **8th SolTech Conference** (Poster)
  Nürnberg, Germany, 09-10/2019

- **CMD2020GEFES** (Poster)
  Madrid, Spain & Online, 08-09/2020

- **Workshop of 9th SolTech Conference** (Talk)
  Bayreuth, Germany & Online, 10/2020
- **Internet NanoGe Conference on Nanocrystals** (Talk)
  Online, 06-07/2021
- **e-conversion Conference** (Poster)
  Munich, Germany, 09/2021
- **SPIE Photonics West** (Talk)
  San Francisco, United States & Online, 02/2022

Awards and More

- **Best Poster Award**
  DPG Summer School - Exciting Nanostructures: Characterizing Advanced Confined Systems, Bad Honnef, Germany, 2019
- **Best Poster Award**
  CMD2020GEFES, Madrid, Spain & Online, 2020
- **Alternative *Nano Letters* Cover**
  Volume 21, Issue 18, published in 2021

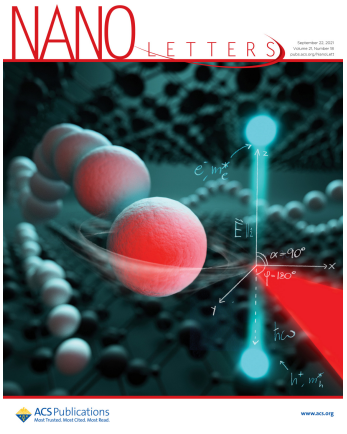

Zusammenfassung

Metallhalogenide haben sich zuletzt als vielversprechende Materialklasse für verschiedene optoelektronische Anwendungen etabliert. Während ihre Wirkungsgrade steil angestiegen sind, sind viele dieser Verbindungen instabil, giftig oder radioaktiv. Andererseits bringt die strukturelle Beschaffenheit der meisten ungiftigen und stabilen Metallhalogeniden eine geringe Leistungsfähigkeit mit sich. Bismut Oxyhalogenide stechen hervor, da sie stabile Verbindungen auf der Basis von ungiftigem Bismut bilden und ihre geschichtete Kristallstruktur gleichzeitig vorteilhaft für die photokatalytische Wasserspaltung zur Erzeugung von Wasserstoff ist. Sie weisen abwechselnd positiv geladene Bismutoxid- und negativ geladene Doppelhalogenidschichten auf. Diese entgegengesetzt geladenen Schichten sind durch ionische Kräfte aneinander gebunden, während die Bindungen innerhalb der Ebenen kovalent sind.

Diese strukturelle Anisotropie bestimmt das Kristallwachstum von Bismut Oxyiodid Nanoplättchen und ermöglicht die präzise Kontrolle ihrer Dicke in Stapelungsrichtung. Außerdem bringt sie nahezu dickenunabhängige optische und elektronische Eigenschaften als direkte Folge lokalisierter Zustände entlang der Ionenbindungen mit sich. Aufgrund dieser Lokalisierung weisen dünnere Nanoplättchen deutlich höhere photokatalytische Umwandlungsraten auf, da weniger Ladungsträger in den inneren Kristallschichten gefangen sind.

Eine Anregung per Femtosekundenlaserpuls induziert eine oszillierende Modulation der optischen Dichte auf der (Sub-)Pikosekundenskala. Dieser liegen zwei Gitterschwingungsmoden entlang der Stapelungsrichtung zugrunde. Sie haben Ihren Ursprung in der Trennung von Elektron-Loch-Paaren in dipolaren elektrischen Feldern in der Richtung der Ionenbindungen. Durch die anschließende ultraschnelle Feldabschirmung werden kohärente Phononen ausgelöst, die nur Schwingungen entlang der elektrischen Feldlinien umfassen. Die kohärente Schwingung und damit auch die oszillierende Modulation der optischen Dichte klingen aufgrund der Dephasierung der kohärenten Phononen ab. Dies belegt die anfängliche Ladungsträgertrennung - ein entscheidender Prozess für photokatalytische Anwendungen.

Die Erzeugung kohärenter Phononen zeigt eine starke Ladungsträger-Phononen-Kopplung in Bismut Oxyiodid. Dementsprechend baut sich nach dem Dephasieren der kohärenten Phononen eine breite photoinduzierte Absorptionsresonanz in den transienten Absorptionsspektren auf, was auf die Bildung von Polaronen zurückzuführen ist.

Abstract

Recently, metal halides have emerged as a promising material class for various optoelectronic applications. While their efficiencies surged in an unprecedented fashion, especially in lead halide perovskites, many of those compounds are unstable, toxic, or radioactive. Then again, non-toxic and stable metal halides mostly suffer from low device performances related to their internal structure. In this context, bismuth oxyhalides stand out as they form stable compounds based on non-toxic bismuth. At the same time, they crystallize in a layered crystal structure which is advantageous for its potential application in photocatalytic water splitting to generate hydrogen. They form alternatingly stacked positive bismuth oxide and negative double halide layers. While the oppositely charged layers are bound by ionic forces, the in-plane bonds are covalent.

That structural anisotropy determines the crystal growth of bismuth oxyiodide nanoplatelets and enables a precise control of their thickness in the stacking direction. Furthermore, it results in virtually thickness-independent optical and electronic properties as a direct consequence of the localized states along the ionic bonds. For that reason, thinner nanoplatelets exhibit significantly higher photocatalytic conversion rates as fewer carriers are trapped in the inner crystal layers.

Optical excitation with a femtosecond laser pulse induces an oscillatory modulation of the optical density on the sub-picosecond timescale. The two underlying frequencies are associated with lattice vibrations along in the stacking direction. This is consistent with the separation of electron-hole pairs in built-in dipolar electric fields along the ionic bonds. Coherent phonons involving only oscillations along the direction of the electric field lines are launched by the subsequent ultrafast field screening. The coherent vibrations induce an oscillatory modulation in pump-probe transients that decays due to dephasing of the coherent phonons and confirm the initial charge separation - a crucial process for photocatalytic applications.

The creation of coherent phonons demonstrates strong carrier-phonon coupling in bismuth oxyiodide. Accordingly, after the dephasing of the coherent phonons, a broad photo-induced absorption resonance builds up in transient absorption spectra, which is consistent with carrier self-trapping through the formation of polarons.

Table of Contents

1 | Introduction

It is a widely accepted fact that we are facing an energy crisis. The symptoms of that crisis are twofold: On the one hand, we are currently burning fossil fuels so quickly and inefficiently that we will soon run out. In the absence of an inherent energy storage capacity, renewable energy sources like solar and wind energy do not provide a steady power output due to their strong daily and seasonal fluctuations.[1] Taken as a whole, this issue addresses the physical unit of energy. On the other hand, burning fossil fuels causes irreversible damage to our environment.[2] According to thermodynamics, this damage accompanies the increase in entropy that we promote by winning energy through transforming highly ordered compounds, like fossil fuels, into products of low order like greenhouse gases.[3] The most prominent and devastating consequence is the resulting global warming. As stated by the second law of thermodynamics, the entropy in isolated systems can never decrease.[3] This underlines the irreversibility of such processes and illustrates that we are experiencing an energy crisis and an entropy crisis - a term that is hardly ever the subject of public debates.[4] Taking the importance of energy and entropy into account, we must be thoughtful and ecological in our use of resources: Truly sustainable solutions fit energy needs in terms of amount and timing, possibly by realizing efficient, CO_2-neutral energy storage like hydrogen for times of need. Preferably, they exploit renewable energy sources like sunlight. In terms of entropy, these solutions must be long-lasting. They cannot depend on unstable compounds reliant on continuous replacement or repair.

These are the requirements for novel materials with potential application in optoelectronic devices. In the last couple of years, ns^2 cation-based metal halides have emerged as novel promising materials for optoelectronic applications.[5–8] Most prominently, the efficiencies of lead halide perovskite solar cells recently skyrocketed to above 25%[9] in an unprecedented fashion approaching the Shockley Queisser limit.[10] Incorporating the heavy metal lead, however, makes the material toxic and unstable when exposed to heat or moisture. In a neighborhood of the periodic table where elements are either toxic (e. g. Pb), unstable in their ionization state (e. g. Sn), or radioactive (e. g. Po and At), bismuth is a promising outlier. Bismuth is not only stable and remarkably harmless (bismuth compounds are often even

less toxic than table salt), as an ion, it is also isoelectric with lead and therefore a suitable replacement.[7,11,12] This naturally places the focus on bismuth halides which are non-toxic and highly stable materials. Therefore, they have the potential to be incorporated into truly sustainable devices. While many bismuth halides fall short of the requirements due to unfavorable structural properties resulting in low device efficiencies,[13,14] bismuth oxyhalides potentially combine the advantages of bismuth halides explained above with a unique and advantageous crystal structure for photocatalytic water splitting. Photocatalysis uses the energy of incoming sunlight to drive chemical reactions, e. g. by splitting water into oxygen and the green fuel hydrogen. That multi-step process relies on charge migration to the reactive sites on the photocatalyst surface. For that reason, nanostructures are often the system of choice, as carrier de Broglie wavelengths are comparable to the extents of the catalyst.[15,16]

This work focuses on bismuth oxyhalide nanostructures examined by time-resolved and time-integrated spectroscopy. It aims to establish links between their structural, catalytical, electronic, and optical properties. Chapter 2 introduces the relevant physical background. Understanding this is necessary to optimize such nanostructures specifically concerning their intended use. For bismuth oxyhalides, this is predominantly the photocatalytic production of hydrogen. Chapter 3 describes the synthesis of the bismuth oxyhalide nanoparticles, the relevant characterization techniques, photocatalytic experiments, and most importantly, time-integrated and time-resolved spectroscopic techniques. Chapter 4 characterizes the investigated bismuth oxyiodide nanoplatelets regarding their shape, structure, and basic photocatalytic, electronic, and optical properties. While there are numerous studies on the use of bismuth oxyhalides as photocatalysts, open questions remained prior to this work: Firstly, the potential formation of dipolar electric fields along the stacking direction of the layered crystal structure might separate charges along that direction. That idea existed as a possible explanation for the high photocatalytic efficiencies before the studies presented here. It was, however, never confirmed experimentally. Chapter 5 studies optically induced coherent phonons in bismuth oxyiodide nanoplatelets to address this question. Secondly, while theoretical simulations and experimental studies are consistent regarding time-integrated properties like the band structure and absorption spectra, a vast gap in our understanding of the respective charge carrier dynamics remained. It was unknown how charge carriers

progress after the initial absorption of light until they either recombine or drive a photocatalytic reaction. Chapter 6 closes that gap by explaining how their strong coupling to the lattice affects charge carrier dynamics and, in particular, gives rise to polaronic effects in bismuth oxyiodide.

2 | Fundamentals

This chapter provides a brief discussion of the fundamental physics studied in this work. It introduces the relevant physical concepts related to the application of bismuth oxyiodide in photocatalysis, its crystal structure, lattice vibrations, and electronic structure. The electronic and structural insights pose a framework for optical transitions and the subsequent charge carrier dynamics in semiconductors for both, free charge carriers in the single-particle picture and (bound) electron-hole pairs in the two-particle picture. The charge carrier dynamics and the underlying physical processes are described with a strong focus on ultrafast processes on the (sub-)picosecond timescale. Finally, this chapter presents the most relevant implications of strong carrier-phonon coupling: the formation of polarons through the distortion of at least partially ionic crystals around introduced charges and the creation of coherent phonons via ultrashort optical excitations like femtosecond laser pulses. The following chapters will revisit these concepts in their analysis and discussion of the experimental data.

2.1 Electronic and Optical Properties of Bismuth Oxyiodide

Bismuth oxyhalides (BiOXs) are a class of semiconductor materials. As for every crystalline solid, their structural, electronic, and optical properties are mutually related. Even though at first sight bismuth oxyhalides differ substantially from many other materials considering these aspects, the same underlying physical concepts apply that have been established in other conventional semiconductors like GaAs, Si, or CdSe. The physical background explained in the following lays a firm foundation for the discussion of the results presented in this work.

2.1.1 Bismuth Oxyiodide - an Efficient Photocatalyst

In recent years BiOXs in general, and bismuth oxyiodide (BiOI) in particular, attracted significant interest from the scientific community due to their photoactivity. Not only could BiOXs prove to be efficient photocatalysts for hydrogen production through water splitting,[17–30] they also found application due to their excellent performance regarding waste degradation,[22,31] their antimicrobial activity[32] and even in cancer treatment via so-called photodynamic ther-

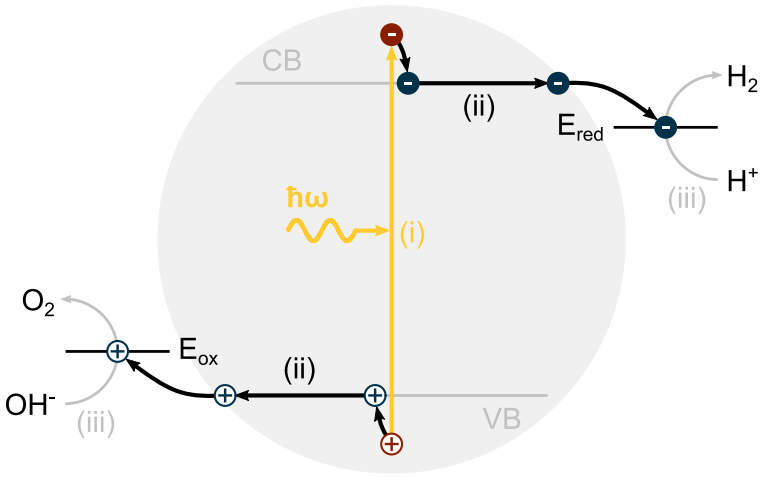

Figure 2.1: Concept of photocatalysis.
The full photocatalytic process in a nanoparticle (gray sphere) involves three critical steps: (i) Creation of an electron-hole pair: After photoexcitation, electrons and holes relax to the energetically favorable band extrema. (ii) Charge separation: Rather than simply recombining or diffusing through the photocatalyst as an exciton, photocatalysis relies on the separation of electrons and holes such that they can reach their respective reactive sites where the final step in photocatalysis occurs. (iii) Photocatalytic reaction: At the surface, electrons and holes are injected into the reducing or oxidizing sub-reaction with sufficient overpotential generating hydrogen or oxygen, respectively.

apy.[33,34] Their band alignment is theoretically suitable to drive full water splitting with small overpotentials.[35] Interestingly, while in many other bismuth-based materials, their tendency to form low-dimensional structures is detrimental to their performance in photocatalysis or photovoltaics,[14,36] the layered crystal structure of BiOX brings about a beneficial anisotropy which will be explained in Chapter 2.1.2.

The photocatalytic reaction that is of interest in this work is the splitting of water into oxygen and hydrogen via the following redox reaction:

$$\begin{aligned} &\text{Reaction:} && 2H_2O + 4e^- + 4h^+ \longrightarrow 2H_2 + O_2 \\ &\text{Reduction:} && 4H_2O + 4e^- \longrightarrow 4OH^- + 2H_2 \\ &\text{Oxidation:} && 4OH^- + 4h^+ \longrightarrow O_2 + 2H_2O \end{aligned}$$

It spans a potential difference of $\Delta E^0 = 1.23\,\text{eV}$ which sets the lower limit for the band gap of a semiconducting photocatalysts capable of driving both steps of the redox reaction.

Photocatalysis relies on three steps: (i) the optical excitation of an electron hole pair, (ii) the separation of electrons and holes and their migration to the respective reactive site at the surface of the photocatalyst, and (iii) the final chemical reaction involving both, electrons and holes separately. These will be explained in the following using water splitting into hydrogen and oxygen as an example: Firstly, photocatalysis typically aims to utilize solar light. The band gap of any semiconducting photocatalyst should be sufficiently low to harvest as much solar light as possible while at the same time it must be wide enough to guarantee sufficient overpotentials for the reduction and oxidation of water. The absorption of a photon (step (i) in Figure 2.1) creates an electron-hole pair that quickly relaxes to the band edges. At this point, it is not trivial that the charge carriers finally contribute to the intended catalytic reaction: It is crucial that the charges do not recombine but separate to reach different reaction sites at the surface of the photocatalyst where it is in contact with the surrounding water (step (ii) in Figure 2.1). That is a challenging step, as it must overcome the attractive Coulomb interaction between electron and hole. Besides the schematically shown separation, other mechanisms like radiative or non-radiative recombination occur in parallel. Lastly, electrons and holes reach the surfaces where, due to the overpotentials between the band positions and the respective redox energy levels, it is energetically beneficial for electrons and holes to drive the photocatalytic reaction (step (iii) in Figure 2.1).[15,16] The ratio between optically excited

electron-hole pairs and the catalytically produced hydrogen molecules defines the quantum efficiency of the catalyst. Often, in an intermediate step, charge carriers are transferred to a co-catalyst like gold, platinum, or nickel at the surface of the absorber material.[37–45] This work focuses on (i) the optical excitation and the crucial subsequent (ii) charge separation. The (iii) photocatalytic reaction itself and options like surface modifications are not studied in depth.

2.1.2 Crystal Structure and Electrostatics

Crystalline solids feature a long-range order in their structure mathematically described by the concept of the crystal lattice. It stipulates an array consisting of all points defined by the lattice vector

$$\mathbf{R} = n_1\mathbf{a}_1 + n_2\mathbf{a}_2 + n_3\mathbf{a}_3 \tag{2.1}$$

with the integers n_i and the primitive vectors $\mathbf{a}_\mathrm{i}$ defining the principal axes of the crystal. This spans a so-called Bravais lattice which ideally expands infinitely in space such that all lattice points are equivalent.[46,47] For real crystals, though, the expansion ends at the surfaces.[48] These are particularly relevant for nanocrystals which are solids that measure less than 100 nm in at least one dimension. Precisely such nanocrystals were studied in this work.

Bismuth oxyhalides, which will be introduced in the following, exhibit an anisotropic crystal structure. Therefore, it is critical to pay attention to the respective crystal direction of interest.

Crystal Structure and Composition of Bismuth Oxyhalides

BiOX is known to crystallize in a matlockite crystal structure (see representative crystal structure of BiOI in Figure 2.2). They are comprised of alternating positively charged bismuth-oxide $[Bi_2O_2]^{2+}$ and negatively charged double halide $2 \times X^-$ layers. The in-plane bonds are covalent while in stacking direction oppositely charged neighboring layers are bound to each other via weak ionic forces.[49–51] Therefore, dipolar electric fields may form between the charged layers.[52] As for other metal halides,[53] the halide X can typically be either fluoride, chloride, bromide, or iodide.[54] While their choice does not change the fundamental structure

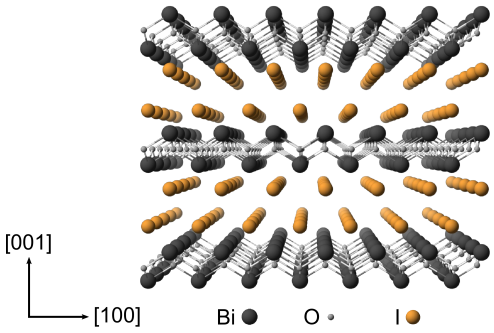

Figure 2.2: BiOI crystal structure.
BiOI is comprised of mutually stacked oppositely charged layers: positive $[Bi_2O_2]^{2+}$ and negative double iodide $2 \times I^-$ layers. The planes form covalent in-plane bonds and are bound to neighboring layers via ionic forces.

of the material, its band gap shifts from the ultraviolet (UV) into the visible regime for increasing atomic number.[50,54–56]

The anisotropy introduced by the crystal structure translates to the crystal growth of BiOX. The in-plane growth by forming covalent bonds exceeds the out-of-plane growth by far.[57,58] Thus, BiOX preferentially forms nanoplatelets (NPs)[59] which often agglomerate in larger microspheres.[60–62] For such NPs, it is crucial to know the elemental character of the terminating [001]-surfaces. It is claimed that both sides of each NP are exposed $[Bi_2O_2]^{2+}$-layers.[20]

Reciprocal Lattice

Importantly, that anisotropy translates into reciprocal space. The reciprocal lattice is defined by the set of vectors $\mathbf{G}$ that yield plane waves with the periodicity of the given Bravais lattice $e^{i\mathbf{G}\cdot\mathbf{r}} = e^{i\mathbf{G}\cdot(\mathbf{r}+\mathbf{R})}$ $\mathbf{G}$ thus fulfills the known condition[47,48]

$$e^{i\mathbf{G}\cdot\mathbf{R}} = 1. \tag{2.2}$$

Therefore, it is critical to note how the axes of the Brillouin zone relate to the crystal axes in later discussions involving e. g. the band structure.

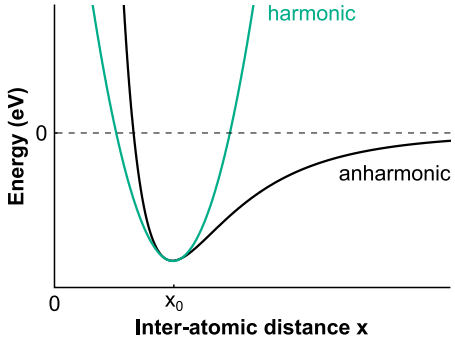

Figure 2.3: Lennard Jones potential for atomic interaction.
The anharmonic model potential involves repulsive and attractive contributions resulting in an equilibrium position x_0. For small dislocations from x_0, a harmonic approximation describes the actual potential reasonably well.

2.1.3 Lattice Vibrations: Phonons

So far, crystals were treated as static systems with clearly defined atomic positions. That approximation is not sufficient: The finite stiffness of crystalline bonds allows macroscopic elastic deformations and microscopic atomic oscillations.[63] It is critical to recognize atomic motion in solids for ample understanding of their electronic and optical properties.

Phonon Basics

Each atom finds itself in its equilibrium position relative to its neighboring atoms x_0 exposed to attractive (e. g. covalent or ionic bonds) and repulsive forces (e. g. Pauli exclusion). The superposition of all such interactions yields an anharmonic potential with a minimum at the atomic equilibrium position. The Lennard-Jones potential in Figure 2.3 is one of the best known model potentials for anharmonic interactions.[64–67] For small dislocations around x_0, this potential is well approximated to be harmonic and thus described by Hooke's law $F = \kappa x$ ($x_0 \equiv 0$).[68] In analogy, this picture refers to the bond stiffness κ when describing the next-neighbor interaction. Accordingly, in the classical harmonic oscillator model, the atoms can oscillate around their equilibrium position with a frequency affected by the atomic bond stiffness κ and mass M

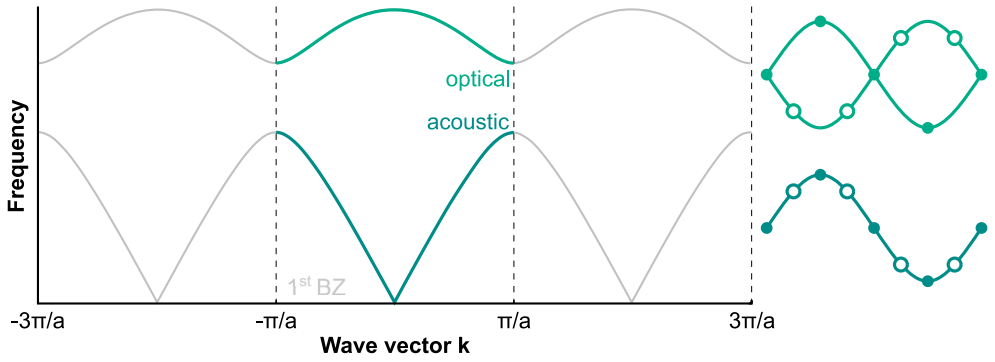

Figure 2.4: Theoretical phonon dispersion of acoustic and optical phonons of a linear chain of atoms with a diatomic basis.
All information beyond the first Brillouin zone is redundant. While for acoustic phonons all atoms of the basis are involved in one collective oscillation, for optical phonons they swing against each other.

$$\omega = \sqrt{\frac{\kappa}{M}} \tag{2.3}$$

that is typically in the THz range or lower. Quantum mechanics treats such lattice vibrations as quasi-particles, so-called phonons. Phonons are bosons that obey Bose-Einstein statistics:

$$f_{\mathrm{BE}}(\hbar\omega, T) = \left[\exp\left(\frac{\hbar\omega - \mu}{k_{\mathrm{B}}T}\right) - 1\right]^{-1} \tag{2.4}$$

with the chemical potential μ.[69,70] In one dimension, they are described by the Hamiltonian

$$\mathcal{H} = \frac{p^2}{2M} + \frac{1}{2}\kappa x^2 = \frac{p^2}{2M} + \frac{1}{2}M\omega^2 x^2. \tag{2.5}$$

One must differ between low energetic acoustic phonons, which involve a collective oscillation of all atoms of the unit cell, and optical phonons, which have higher energies and describe individual atomic vibrations within the basis (see Figure 2.4). For any phonon, one can define an annihilation and a creation operator $\hat{a}$ and $\hat{a}^\dagger$, respectively:

$$\hat{a} = \frac{\hat{p} - iM\omega\hat{x}}{\sqrt{2\hbar\omega M}} \text{ and } \hat{a}^\dagger = \frac{\hat{p} + iM\omega\hat{x}}{\sqrt{2\hbar\omega M}} \tag{2.6}$$

with the momentum operator $\hat{p}$ to express the harmonic Hamiltonian as

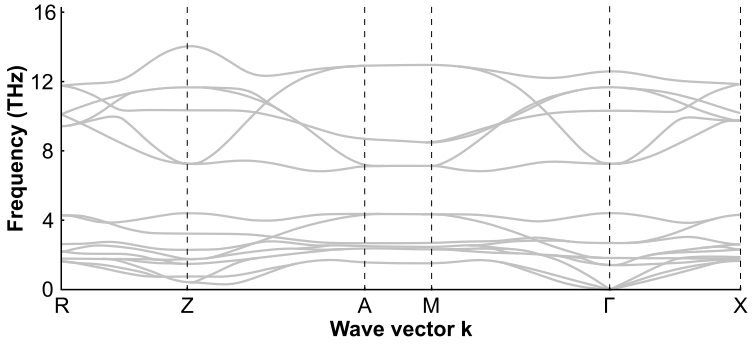

Figure 2.5: Phonon dispersion of BiOI.
Adapted from Reference [74] with permission from the PCCP Owner Societies.

$$\mathcal{H} = \hbar\omega\left(\hat{a}\hat{a}^{\dagger} + \frac{1}{2}\right). \tag{2.7}$$

Using creation and annihilation operators illustrates that, just like for photons, only discrete quanta of phonon energy can be created or annihilated.[71] Figure 2.3 shows clearly how the harmonic potential is only a first approximation. More profound models require higher, anharmonic terms.[72,73] These are subject of Section 2.3.2.

Phonons in Bismuth Oxyiodide

The unit cell of BiOI contains two atoms of each incorporated element. Thus, the six atoms allow 18 (three acoustic and 15 optical) vibronic modes. The theoretically predicted phonon dispersion relation shown in Figure 2.5 is consistent with experimental Raman experiments matching the frequencies of selected phonon modes.[74] The energetically highest optical phonon modes reach frequencies of around 15 THz.[74,75]

2.1.4 Electronic Band Structure

Mobile electrons in a crystal structure, with nuclei moving around their equilibrium position, yield a complex many-body problem. It is crucial to disentangle electronic and atomic motion to solve the Schrödinger equation of such systems.

Hamiltonian of a Solid

The Hamiltonian of a solid includes electrons and the nuclei in their individual motion as well as mutual interaction

$$\begin{aligned}\mathcal{H} = \quad & \underbrace{-\frac{\hbar^2}{2m_e}\sum_{\mathrm{i}}\nabla_{\mathrm{i}}^2}_{\substack{\text{kinetic energy}\\ \text{of electrons}}} \quad \underbrace{-\frac{1}{4\pi\varepsilon_0}\sum_{\mathrm{i}}\sum_{\mathrm{I}}\frac{Z_{\mathrm{I}}e^2}{|\mathbf{r}_{\mathrm{i}}-\mathbf{R}_{\mathrm{I}}|}}_{\substack{\text{electron-nucleon}\\ \text{Coulomb interaction}}} \quad \underbrace{+\frac{1}{8\pi\varepsilon_0}\sum_{\mathrm{i}}\sum_{\mathrm{i}\neq\mathrm{j}}\frac{e^2}{|\mathbf{r}_{\mathrm{i}}-\mathbf{r}_{\mathrm{j}}|}}_{\substack{\text{electron-electron}\\ \text{Coulomb interaction}}} \\ & \underbrace{-\sum_{\mathrm{I}}\frac{\hbar^2}{2M_{\mathrm{I}}}\nabla_{\mathrm{I}}^2}_{\substack{\text{kinetic energy}\\ \text{of nuclei}}} \quad \underbrace{+\frac{1}{8\pi\varepsilon_0}\sum_{\mathrm{I}}\sum_{\mathrm{I}\neq\mathrm{J}}\frac{Z_{\mathrm{I}}Z_{\mathrm{J}}e^2}{|\mathbf{R}_{\mathrm{I}}-\mathbf{R}_{\mathrm{J}}|}}_{\substack{\text{nucleon-nucleon}\\ \text{Coulomb interaction}}}\end{aligned} \tag{2.8}$$

with i, j labeling the electrons and I, J the nuclei and M_{I}, Z_{I}, and $\mathbf{R}_{\mathrm{I}}$ denoting mass, atomic number, and position of nucleus I. It is important to note that the masses of the nuclei are much higher than those of the electrons. As a consequence, the contribution of the kinetic energy to the total Hamiltonian is minor. This allows a separate treatment of atomic and electronic motion. As of this adiabatic (Born-Oppenheimer) approximation, the electronic Hamiltonian is

$$\mathcal{H}_{\mathrm{e}} = -\frac{\hbar^2}{2m_{\mathrm{e}}}\sum_{\mathrm{i}}\nabla_{\mathrm{i}}^2 - \frac{1}{4\pi\varepsilon_0}\sum_{\mathrm{i}}\sum_{\mathrm{I}}\frac{Z_{\mathrm{I}}e^2}{|\mathbf{r}_{\mathrm{i}}-\mathbf{R}_{\mathrm{I}}|} + \frac{1}{8\pi\varepsilon_0}\sum_{\mathrm{i}}\sum_{\mathrm{i}\neq\mathrm{j}}\frac{e^2}{|\mathbf{r}_{\mathrm{i}}-\mathbf{r}_{\mathrm{j}}|} \tag{2.9}$$

with $\mathbf{R}_{\mathrm{I}}$ treated as constants.[69] This work will reach the limits of this model where electronic and ionic motion is not sufficiently decoupled but rather mutually dependent.

Bloch's Theorem

The periodicity of the lattice translates into the lattice potential $V(\mathbf{r})$, the superposition of all atomic core potentials:[47]

$$V(\mathbf{r}) = V(\mathbf{r}+\mathbf{R}). \tag{2.10}$$

This periodicity is of the same order of magnitude as the typical de Broglie wavelength of electrons in the Sommerfeld free electron model.[76] It thus substantially affects electronic motion in the crystal as it enters the time-independent Schrödinger equation in the single electron approximation as a part of the Hamiltonian[48]

$$\mathcal{H}(\mathbf{r})\psi(\mathbf{r}) = \left[-\frac{\hbar^2}{2m_0}\nabla^2 + V(\mathbf{r})\right]\psi(\mathbf{r}) = E\psi(\mathbf{r}). \tag{2.11}$$

As a crystal typically contains around 10^{23} atoms per cm^3, it is pragmatic to express this many-body problem mathematically through the periodicity of their arrangement.[77] The periodicity has further decisive consequences on the wave functions as Felix Bloch discovered:[78] All eigenstates can be expressed by a wave function

$$\psi_{n\mathbf{k}}(\mathbf{r}) = e^{i\mathbf{kr}}u_{n\mathbf{k}}(\mathbf{r}) \tag{2.12}$$

where for all $\mathbf{R}$ of the Bravais lattice

$$u_{n\mathbf{k}}(\mathbf{r}+\mathbf{R}) = u_{n\mathbf{k}}(\mathbf{r}). \tag{2.13}$$

Consequently, for any translation by the Bravais lattice vector, there is a wave vector $\mathbf{k}$ associated with each eigenstate ψ such that

$$\psi_{n\mathbf{k}}(\mathbf{r}+\mathbf{R}) = e^{i\mathbf{kR}}\psi_{n\mathbf{k}}(\mathbf{r}). \tag{2.14}$$

For the results presented in this work, it is critical to account for both the plain wave $e^{i\mathbf{kr}}$ contribution and the influence of the lattice $u_{n\mathbf{k}}(\mathbf{r})$ on the states in bismuth oxyhalides. The fact that an energy eigenstate of an electron in a crystal is a function of the spatial coordinate has far-reaching consequences, especially in anisotropic materials like BiOI.

Band Structure of Solids

The eigenvalues of a system provide the energetic structure of a solid, the so-called band structure. The band structure $E(\mathbf{k})$ is the dispersion relation linking energy E and wave vector $\mathbf{k}$ with the same quasi-momentum $\hbar\mathbf{k}$ associated with the Bloch wave functions above.

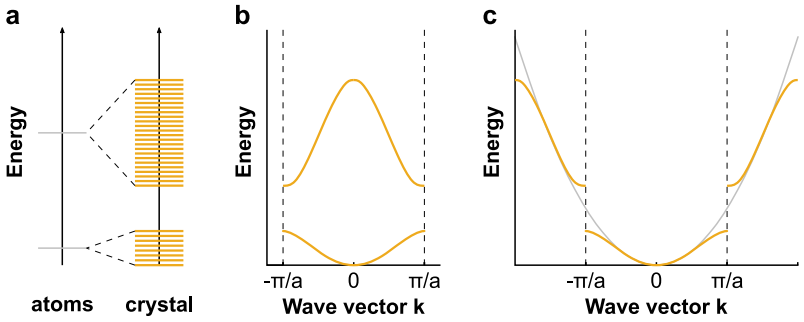

Figure 2.6: Tight binding vs. nearly-free electron model.
(a) Coupling of atomic states in the tight-binding model, **(b)** band structure in the reduced zone scheme, **(c)** extended zone scheme in the nearly-free-electron model with the dispersion of free carriers in gray.

There are two models that, approaching the solution from two opposite limits, lead to an intuitive understanding of the band structure of solids, namely the *tight-binding model* and the *nearly-free-electron model*.

The tight-binding model accounts for the construction of a solid by the periodic arrangement of atoms. These atoms themselves all have well-defined energy levels E_0 associated with the eigenstate wavefunction $\phi_{\mathbf{k}}(\mathbf{r}-\mathbf{r}_\mathrm{m})$ of the atomic potential $W(\mathbf{r}-\mathbf{r}_\mathrm{m})$ at an atom denoted by the index m. In a crystal, the constituent atomic potentials add up in the Hamiltonian. The according time-independent Schrödinger equation

$$\mathcal{H}\psi_{\mathbf{k}}(\mathbf{r}) = \left[-\frac{\hbar^2}{2m_0} + \sum_m W(\mathbf{r}-\mathbf{r}_m)\right]\psi_{\mathbf{k}}(\mathbf{r}), \tag{2.15}$$

considering only next-neighbor interaction, yields the solution

$$E(\mathbf{k}) = E_0 - A - \sum_{\mathbf{R}\neq 0} B e^{i\mathbf{k}\cdot\mathbf{R}} \tag{2.16}$$

with the Coulomb energy A and the exchange energy B. The initially $\mathbf{k}$-independent, well-defined energy levels gain a dispersion $E(\mathbf{k})$ through mutual coupling of the constituent atoms. As of the linear combination of atomic orbitals (LCAO) theory, the number of states scales with the number of incorporated atoms (see Figure 2.6 a & b).[48,69]

In the opposite limit, instead of starting from the atomic potential, the nearly-free electron model treats it as a small perturbation, meaning that it only marginally affects the parabolic

dispersion relation for free electrons

$$E(\mathbf{k}) = \frac{\hbar^2 \mathbf{k}^2}{2m_0}. \tag{2.17}$$

Importantly, while $|\mathbf{k}| < \pi/a$ yields running waves, standing waves are described by $\mathbf{k} = \pm\pi/a$ at the boundaries of the Brillouin zone. Standing waves have a group velocity $v_g = \partial E(k)/\partial k = 0$. This implies that the dispersion relation $E(\mathbf{k})$ must deviate from the free carrier dispersion near the Brillouine zone boundaries as shown in Figure 2.6 b & c. As a consequence, gaps open up in which there are no electronic states.[63,69]

Density of States

The band structure itself does not provide any information about the occupation of the states. Rather, it can be used to determine the density of states

$$\rho(E) = dN(E)/dE. \tag{2.18}$$

Assuming perfectly parabolic bands, as of the effective mass approximation $E(k) = \hbar^2 k^2/2m^\star$ where $m^\star$ describes the effective mass of a carrier, yields simple solutions for zero- to three-dimensional systems: This allows to express k as $k = (2m^\star E/\hbar^2)^{1/2}$ and finally leads to

$$\rho_{\mathrm{3D}}(E) = \frac{1}{2\pi^2}\left(\frac{2m^\star}{\hbar^2}\right)^{3/2} E^{1/2} \tag{2.19}$$

$$\rho_{\mathrm{2D}}(E) = \frac{m^\star}{\pi\hbar^2} \tag{2.20}$$

$$\rho_{\mathrm{1D}}(E) = \frac{m^\star}{\pi\hbar}\left(\frac{m^\star}{2E}\right)^{-1/2} \tag{2.21}$$

$$\rho_{\mathrm{0D}}(E) = 2\delta(E) \tag{2.22}$$

denoting the density of states as a function of energy for each band.[69,79] The total density of states of a semiconductor is the superposition of all such contributions.

The Occupation of Electronic States

At zero temperature, the limited number of electrons in a solid state occupies the available states starting at the energetically lowest state. Electrons are fermions, indistinguishable particles with half-integer spin, and thus obey fermionic statistics. The Fermi-Dirac distribution

$$f_{\mathrm{FD}}(E) = \left[\exp\left(-\frac{E - E_F}{k_B T}\right) + 1\right]^{-1} \tag{2.23}$$

describes the distribution of electrons as a function of energy.[80,81] The Fermi energy E_F defines the energy up to which these bands are filled by electrons in the ground state at $T = 0\,\mathrm{K}$. The Fermi energy in semiconductors, per definition, is in a band gap. Thus, the states below E_F form the so-called valence band (VB) that is filled completely by electrons while the empty states above form the conduction band (CB). Altogether, the probability to find an electron in an energy interval from E to $E + dE$ in thermal equilibrium

$$\rho(E) f(E, T) dE \tag{2.24}$$

depends on both, the density of states as well as the statistics describing the occupation of the available states.[69,80,81] In contrast, metals have partially filled bands due to their Fermi energy being within one band. The energy difference between the valence band maximum (VBM) and the conduction band minimum (CBM) defines the band gap E_G of a semiconductor. Semiconductors with $\mathbf{k}_{\mathrm{VBM}} = \mathbf{k}_{\mathrm{CBM}}$ are so-called direct semiconductors while those with $\mathbf{k}_{\mathrm{VBM}} \neq \mathbf{k}_{\mathrm{CBM}}$ are indirect.

Electronic Band Structure of Bismuth Oxyiodide

Figure 2.7 displays the in-plane band structure of BiOI, the halide compound of interest in this work. The bands in-plane along the strong covalent bonds are well-dispersed. In contrast, due to the weak coupling between the neighboring layers mutually bound to each other via ionic forces, there is no out-of-plane dispersion. The VB consists of many relatively flat bands which are energetically close to each other. The bands in the CB have a significantly higher dispersion. Thus the electrons have lower effective masses than the holes.[28,82] The

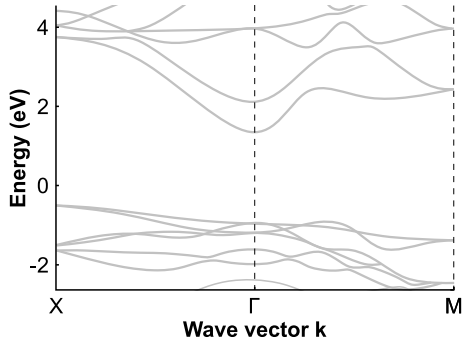

Figure 2.7: Band structure of BiOI.
BiOI is an indirect semiconductor with the VBM at the X-point and the CBM at the Γ-point. Due to the weak ionic out-of-plane bonds, only the in-plane dispersion is shown (adapted from Wang *et al.*[28] - published by The Royal Society of Chemistry).

band structure of BiOI shows the indirect nature of the band gap with the VBM at the X-point and the CBM at the Γ-point. The energy threshold for direct transitions is much higher at the X-point ($\sim$ 4.1 eV) than at the Γ-point ($\sim$ 2.3 eV).

Generally, BiOXs are indirect semiconductors. By a suitable choice of the halide X, their band gap is tunable from approximately 3.6 eV (BiOF) to 1.8 eV (BiOI) as shown in Table 2.1.[54,56,83–90]

Table 2.1: Band gaps of bismuth oxyhalides[54,56,83–90]

	BiOF	BiOCl	BiOBr	BiOI
Band gap (eV)	3.5 - 3.6	2.9 - 3.4	2.3 - 2.9	1.8 - 2.1

Bond Formation in Bismuth Oxyiodide

At this point, it is crucial to connect the band structure and the crystal structure of BiOI. This requires a profound understanding of the role of bismuth that participates in both, in-plane and out-of-plane bonds. Bismuth generally forms bonds by partial oxidation from $6s^2 6p^3$ to $6s^2 6p^0$. The resulting Bi^{3+} possesses a stable electron pair $6s^2$. Other elements like tin can have different oxidation states (Sn^{2+} and Sn^{4+}) and are thus not stable in the 2+ state.[91]

The 6p-orbital transfers its three electrons to the neighboring elements, e. g. halides, where electrons fill the outer p-orbitals. Covalent bismuth-oxygen interaction dominates in-plane bonding while the out-of-plane bonds in BiOI arise predominantly from ionic forces between bismuth and iodide ions (see Figure 2.8) as explained in the following:

The covalent in-plane bonds in BiOI result from the s-p interaction between bismuth and oxygen: In detail, the Bi-6s and the O-2p orbitals hybridize in a complex pattern shown in the bottom left panel of Figure 2.8. The antibonding orbital formed between Bi-6s and O-2p subsequently hybridizes with the Bi-6p orbitals which results in the final energetic structure that lifts the VBM compared to a hypothetical scenario without bismuth-oxide interaction.[16,92–94] Although, the lone Bi 6s electron pair is often regarded as inert, such interaction of post-transition metals with oxygen has been proposed for other p-block metal oxides.[95–105] The resulting in-plane bonding orbitals originate from mixing of Bi-6p and O-2p and contribute to the top of the VB,[106] which is potentially advantageous for the defect-tolerance of BiOI. Further, it was proposed play a beneficial role in photocatalysis due to the lifted VB edge.[16,94]

In contrast, the out-of-plane bonds are ionic and have only a very small covalent contribution. As a consequence of the electron exchange between bismuth and iodide, the ions are bound to each other by Coulomb forces (see Figure 2.8).[82] That interaction is weak compared to the covalent in-plane bonds and is consistent with the extraordinarily high effective out-of-plane masses in BiOI.[8] Additionally, there is a minor covalent contribution to the out-of-plane bonds. Even though that contribution is small, it might bring along advantageous properties in terms of stability and defect-tolerance which is known to be true in other bismuth halides: Antibonding orbitals from cation-s and anion-p state hybridization form the VBM.[107,108] The top right panel of Figure 2.8 shows the schematic orbital interaction of typical bismuth and iodide.[109] It differs significantly from other semiconductors like GaAs where bonding orbitals form the VBM.[110] The dominant contribution of the s-orbital to the top of the VB further brings along a stabilization effect of the 6s electron pair: The occupied antibonding orbital lifts the VBM compared to the contributing orbitals.

Both, the involvement of oxygen and the binding mechanism yielding the small covalent contribution to the out-of-plane bonds decrease the band gap into the visible range by lifting

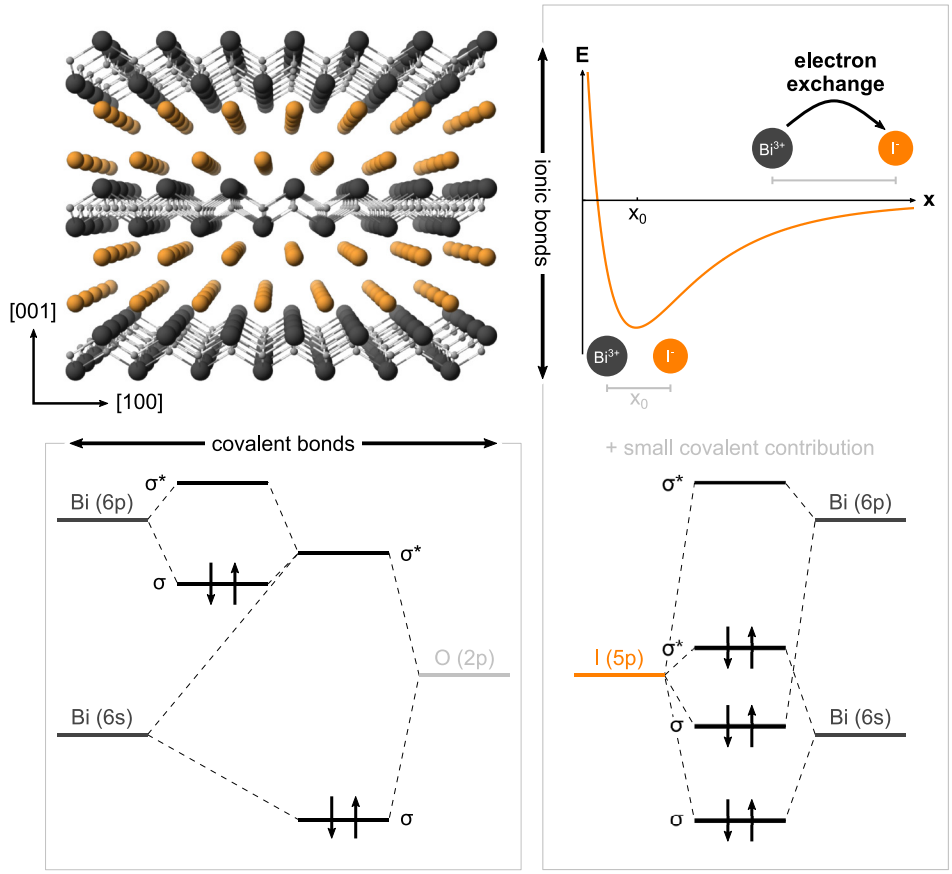

Figure 2.8: Covalent in-plane bonds and predominantly ionic out-of-plane bonds in BiOI. The anisotropy of the BiOI crystal structure (Bi: dark gray, O: light gray, I: orange) involves the nature of the in-plane and out-of-plane bonds: The in-plane bonds arise predominantly from bismuth-oxygen interaction involving the Bi-6s, Bi-6p and O-2p orbitals. It results in covalent bonds in that direction. Out-of-plane bonds are mostly ionic. The electron transfer from bismuth to iodide gives rise to Coulomb forces between the alternatingly charged stacked layers in BiOI. Besides that ionic force, there is a small covalent contribution from the hybridization of I-5p orbitals with Bi-6s and Bi-6p orbitals like in other metal halides.

the VB. Thereby, they play a critical role concerning defect tolerance. Interstitials, antisite defects, and defects leading to dangling bonds (like vacancies, nanocrystal surfaces, or grain boundaries) introduce additional energy levels close to the valence atomic orbitals. Due to the lifted VB top, these resonances typically lie within the band or might form only shallow defects leading to a high defect-tolerance of such materials.[36,107,110] Therefore, only external impurities may form deep traps. Furthermore, relativistic effects such as spin-orbit coupling increase the width of the 6p conduction band.[111,112] As a consequence, the CB reaches sufficiently low energies such that dangling bonds, associated with e. g. halide

vacancies, lie within the CB or form only shallow defects.[107] Apart from the low toxicity, these considerations also apply to other, similar heavy metals, like lead.[6] For most applications, deep traps limit efficiencies.[113] Defect-assisted Shockley-Read-Hall recombination yields a loss mechanism that is associated with a reduced carrier lifetime.[114] A lifetime of one nanosecond is a typical benchmark for commercial applications[110] which materials with high deep trap densities can most likely not reach. Shallow defects, on the other hand, may even play a beneficial role in photocatalysis. Its defect tolerance further makes bismuth-based semiconductor materials, and BiOI in particular,[115,116] an appealing choice for applications that use nanocrystals, especially considering the role of surface defects.[107]

2.2 Optical Transitions in Semiconductors

A semiconductor in the ground state has a fully occupied VB and an empty CB. An incoming photon can be absorbed by the material and promote the system from the ground state into an excited state either by creating free electron hole pairs or excitons. This section gives a comprehensive overview of the charge carrier dynamics triggered by the initial photoexcitation in both, the single particle picture (free charge carriers) and the two-particle picture (electron hole pairs: excitons) with a focus on the involved optical transitions.

2.2.1 Single-Particle Picture: Free Charge Carrier Dynamics

In semiconductors, due to the completely filled bands, electrons are not mobile in the ground state. When in the ground state, the VB is completely filled and the electrons have a net velocity of zero and therefore do not conduct a current. It is, however, possible to promote electrons from the VB to the CB or to create excitons, electron-hole pairs bound by the Coulomb force, via e. g. thermal or optical excitation across the band gap.[117] An excited electron leaves behind an unoccupied state in the VB, a hole. The holes are quasiparticles that behave like positively charged carriers. Both, electrons and holes are mobile after excitation. Generally, a semiconductor, like any other body, will reach a thermal equilibrium with its surrounding after a sufficient time period. Both, electron and hole then undergo a series of relaxation processes until the semiconductor returns to its thermal equilibrium, the ground state.[118]

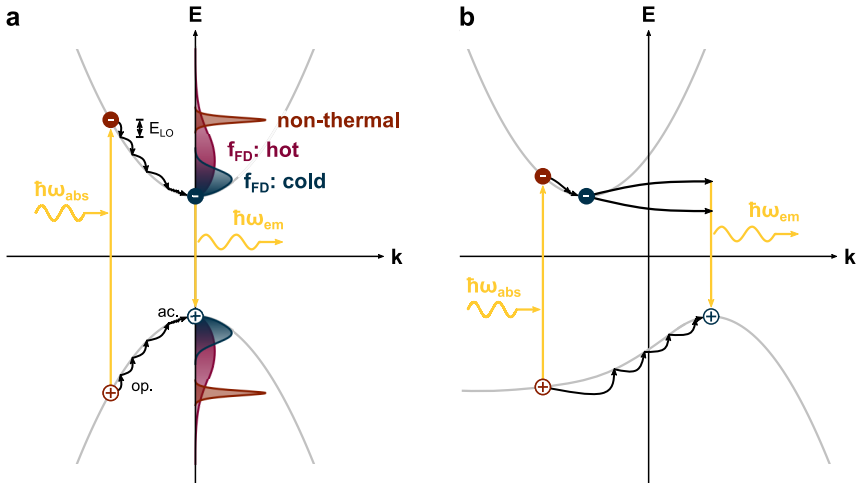

Figure 2.9: Charge carrier dynamics and optical transitions in the single particle picture. **(a)** Charge carrier relaxation in a direct semiconductor. The initial optical excitation of an electron-hole pair in a semiconductor by a photon with energy $\hbar\omega_{\mathrm{abs}} > E_{\mathrm{G}}$ creates a non-thermal charge distribution, namely a normal distribution at the respective electron and hole energies. It quickly transitions into a hot thermal distribution characterized by a temperature higher than that of the lattice. The carriers then exchange heat with the lattice via phonon emission (black solid arrows) and relax to the band extrema. Typically, the relaxation first involves optical phonons which are high in energy and only the final relaxation in the energy range smaller than the optical phonon energy involves acoustic phonons. After that, electrons and holes occupy the available states according to a thermal distribution of the lattice temperature until electrons and holes finally recombine. The recombination can either occur radiatively and emit a photon with the energy $\hbar\omega_{\mathrm{em}}$ to conserve energy or non-radiatively via carrier-lattice interactions. **(b)** Charge carrier relaxation in an indirect semiconductor. Generally the same dynamics occur in indirect semiconductors. The final recombination, however, requires either the absorption or the emission of a phonon.

When an ultrashort femtosecond laser pulse excites the semiconductor, the moment of excitation is well-defined and allows to measure ultrafast subsequent processes in spectroscopic experiments. In the following charge carrier dynamics as well as phonon dynamics will be explained shortly by temporally following their evolution beginning with the initial excitation, as described by Shah.[119] It must, however, be noted that charge carrier and phonon dynamics are closely connected and must thus be discussed in relation to each other.

Optical Excitation

At the beginning of that series of events, there is the initial excitation. The optical excitation of a semiconductor by an incoming photon creates free charge carriers (or excitons which will be discussed in Section 2.2.2). An accurate quantum mechanical model describing the absorption of light and the creation of photoexcited charge carriers considers the interaction

of matter and light in the time-dependent Schrödinger equation

$$[\mathcal{H}(\mathbf{r}) + \mathcal{H}'(t)]\,\psi = \left[\frac{\mathbf{p}^2}{2m_0} + V(t) - \frac{e}{m_0}\mathbf{p}\cdot\mathbf{A}\right]\psi = i\hbar\frac{\partial\psi}{\partial t} \tag{2.25}$$

with the momentum operator $\mathbf{p} = -i\hbar\nabla$ and the first-order time-dependent perturbation $\mathcal{H}'(t) = -e\mathbf{p}\cdot\mathbf{A}/m_0$ through the incoming electromagnetic field[79,120]

$$\mathbf{A}(\mathbf{r},t) = \mathbf{A}_0\left[\exp i\cdot(\mathbf{k}\cdot\mathbf{r} - \omega t) + \text{c.c.}\right]. \tag{2.26}$$

Optical excitations are capable of promoting charge carriers from their ground state to an excited state. Such a process can involve states in the bands, excitonic states, and even defect states. An incoming photon, providing an energy $\hbar\omega$ that matches the energy difference $E_f - E_i$ between the initial $|i\rangle$ and final state $|f\rangle$ of an electron, can be absorbed by the electron to undergo the respective transition between these states. The associated rate of such a transition is given by Fermi's golden rule

$$\Gamma_{i\to f} = \frac{2\pi}{\hbar}\left|\langle f|\mathcal{H}'|i\rangle\right|^2\delta(E_f - E_i - \hbar\omega) \tag{2.27}$$

which follows from the time-dependent perturbation theory and links the initial and the final state according to the perturbation in form of an incoming photon mathematically expressed through $\mathcal{H}'$. The probability for a photon to be absorbed by a semiconductor is proportional to the sum of all transitions of that energy weighted by the transition probability given above.[121]

It is important to differentiate clearly between direct and indirect optical transitions (see Figure 2.9). The **k**-values of photons in the visible range are negligible compared to the extent of the Brillouin zone.[69] Thus, a direct optical transition induced by absorption of a photon appears as virtually vertical in the band structure $E(\mathbf{k})$. There are, however, also indirect optical transitions which are of interest especially in indirect semiconductors. Such transitions promote a carrier to a state with a different **k** than its initial state. In contrast to photons, which provide energy but virtually no momentum, absorption or emission of a phonon with large k and small energy compared to the photon can conserve energy and momentum in indirect transitions. Such indirect transitions, as in the reverse process of the emision schematically

shown in Figure 2.9 b, have a significantly lower transition strength than direct transitions. In indirect semiconductors, there is an E^2-like absorption onset below the energy threshold for direct optical transitions.[117] Therefore, direct transitions dominate in the absorption spectra.

The optical excitation of an electron-hole pair poses the starting point for subsequent charge carrier dynamics which are explained in the following.

Coherent Regime

An incident ultrashort laser pulse creates excitations with a well-defined phase relation in their polarization. They are thus initially coherent for times of up to around 200 fs and begin to dephase.[122] Multiple scattering mechanisms occurring on ultrashort time scales involving momentum scattering, carrier-carrier scattering, intervalley scattering, and carrier-optical phonon scattering drive the dephasing.[119,123]

Non-Thermal Regime

As implied by the name, shortly after the initial excitation ($\lesssim 2$ ps), the carriers pose a non-thermal distribution, meaning that the distribution function does not simply correspond to a temperature (see Figure 2.9 a). It rather centers around the energy of the initial excitation. Processes like carrier-carrier scattering, carrier-optical phonon scattering, intervalley and intersubband scattering lead to a transfer from a non-thermal distribution to a thermal distribution.[119] Fermi-Dirac distribution functions then describe both electrons and holes.[80,81] Especially for excitations well above the band gap, the excess energy leads to a *hot* thermalized distribution corresponding to a carrier temperature T_c much higher than the lattice temperature.[124,125]

Hot-Carrier Regime

That distribution of *hot* carriers then continuously cools down by exchanging heat with the crystal lattice until finally the thermal carrier distribution is described by the lattice temperature. This is schematically shown in Figure 2.9 a. Accordingly, more carriers relax to states at or close to the VBM and CBM. Once a carrier is so close to the band edge that emission

of an optical phonon is not possible anymore ($k_B T_c \lesssim E_{\mathrm{LO}}$), less efficient carrier-acoustic phonon scattering plays an important role for the final cooling mechanism as it involves smaller energies. As a consequence, the process of cooling can take approximately from 1 ps to 100 ps for different materials. Eventually, carriers occupy the energetically lowest states, the band edges, and can potentially form bound states in the form of excitons at an energy below the band gap.[119,124,126,127]

Isothermal Regime: Charge Carrier Recombination

The final relaxation step, the (radiative) recombination of electron and hole, is typically a significantly slower process than the initial relaxation. Like the excitation, recombination must conserve energy and momentum. Thus, it is crucial to recognize the dominant charge carrier species, whether they form excitons, which are likely to recombine quickly, or free carriers. Free carriers in direct semiconductors can recombine by simply emitting a photon with the energy $\hbar\omega = E_{\mathrm{CBM}} - E_{\mathrm{VBM}}$ (see Figure 2.9 a) while in indirect semiconductors, recombination additionally requires emission or absorption of a phonon (see Figure 2.9 b). As a consequence, indirect recombination is generally much slower. Only those electron-hole pairs will recombine that occupy states in the radiative window.[128] Their empty phase-space volume will quickly be re-occupied by electron-hole pairs energetically higher in the thermal distribution.[119,129]

The exact charge carrier dynamics in semiconductors strongly depend on the carrier species, the charge carrier density $n(t)$, and the defect density in the material. Excitonic and defect-assisted recombination are associated with a charge carrier density-independent recombination described by $dn(t)/dt = -k_1 n(t)$ and thus undergo so-called monomolecular decay. The recombination of two carriers or exciton-exciton annihilation, generally processes involving two particles follow bimolecular recombination with a charge carrier density-dependent rate $dn(t)/dt = -k_2 n(t)^2$. In analogy, many-body processes like Auger-recombination involving three particles obey $dn(t)/dt = -k_3 n(t)^3$. Altogether, the recombination rate

$$r(n(t)) = k_1 + k_2 n(t) + k_3 n(t)^2 \tag{2.28}$$

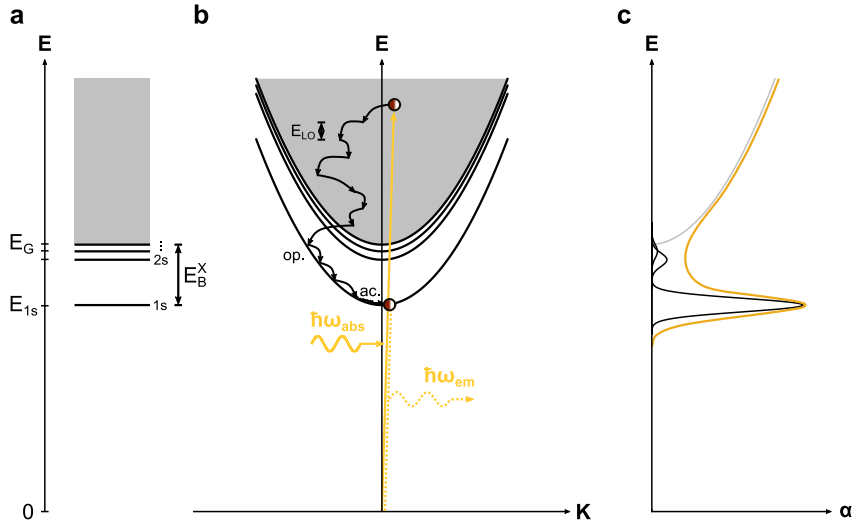

Figure 2.10: Charge carrier dynamics and optical transitions in the two-particle picture. **(a)** The attractive Coulomb interaction of electrons and holes yields additional excitonic states at energies below the band gap energy E_{G}. In analogy to the hydrogen atom, above the energetically lowest 1s exciton state, there are further 2s, 3s, etc. states. **(b)** In the two particle picture an incoming photon can create an electron hole pair with an energy E and a momentum $\mathbf{K} = \mathbf{k}_{\mathrm{e}} + \mathbf{k}_{\mathrm{h}}$. That electron-hole-pair then relaxes preferrably via longitudinal optical (LO) phonon scattering to the energetically lowest state on the 1s exciton branch. **(c)** The two-particle picture in (b) illustrates that photons (E, $\mathbf{K}$) can be absorbed by a semiconductor if their virtually vertical dispersion relation $\omega = ck$ crosses an exciton branch or lies within the continuum (gray) with the respective energy and momentum. This directly explains the emergence of sharp resonances at the respective exciton energies followed by a broad continuum absorption, following a square-root course for the example of a direct 3D semiconductor.

changes with time as the carriers recombine.[114,130]

2.2.2 Two-Particle Picture: Excitons

Up to this point, Coulomb interaction between the negatively charged electron and the positively charged hole has been neglected. This interaction gives rise to bound states, so-called excitons. It is important to note that generally exciton wave functions are combinations of electron and hole single particle wave functions.[131] Thus, the following two-particle picture must not be understood as a replacement of the single particle picture but it builds up on it. It can describe both, free electron-hole pairs and bound electron-hole pairs, so-called excitons.

Formation of Excitons

In the two-particle picture one treats the attractive force between electrons and holes as a perturbation. Due to this interaction, an exciton with a wave vector $\mathbf{K} = \mathbf{k}_e + \mathbf{k}_e$ is formed from electron and hole wave packets with wave vectors $\mathbf{k}_\mathrm{e}$ and $\mathbf{k}_\mathrm{h}$, respectively.[132,133] Conceptually, it is reasonable to differentiate between two scenarios:

Firstly, so-called Wannier-Mott excitons with a radius that spans multiple unit cells are typically found in crystalline inorganic semiconductors. For low effective masses and a large dielectric constant ε, this scenario is mathematically analogous to the hydrogen problem.[134] The Wannier-Mott model yields the Hamiltonian

$$\mathcal{H} = -\frac{\hbar^2}{2m_\mathrm{e}^\star}\nabla_\mathrm{e}^2 - \frac{\hbar^2}{2m_\mathrm{h}^\star}\nabla_\mathrm{h}^2 - \frac{e^2}{4\pi\varepsilon R} \tag{2.29}$$

with the electron-hole distance $R = |\mathbf{r}_\mathrm{e} - \mathbf{r}_\mathrm{h}|$.[69] The resulting exciton binding energy

$$E_\mathrm{B,n}^\mathrm{X} = \frac{\mu}{m_0\varepsilon^2}\mathrm{Ry}\frac{1}{n^2} = \frac{\mathrm{Ry}^\star}{n^2} \tag{2.30}$$

is much smaller than the Rydberg constant $\mathrm{Ry} = 13.6\,\mathrm{meV}$ for two reasons: Firstly, the effective mass μ in many semiconductors is smaller than the free electron mass m_0. Secondly, the Coulomb interaction between electron and hole is screened by the medium penetrated by the electric field, the semiconductor itself. The higher the (static) dielectric constant ε, the more effeciently it screens the electron-hole interaction and lowers the exciton binding energy. The integer n is the principal quantum number denoting the excitonic sublevels in analogy to the hydrogen series. As a consequence of the attractive interaction between electron and hole, they are bound to each other spatially. This is reflected in their exponential wavefunction

$$\phi(R) = \frac{1}{\sqrt{\pi a_\mathrm{X}^3}}\exp\left(-R/a_\mathrm{X}\right) \tag{2.31}$$

in three dimensions. The so-called exciton Bohr radius

$$a_\mathrm{X} = \frac{m_0}{\mu}\varepsilon n^2 a_\mathrm{H} \tag{2.32}$$

with the Bohr radius of the hydrogen atom a_{H} defines the mean distance between electron and hole.[121,135,136]

Secondly, bound Frenkel excitons are confined to a volume of the same order of size as the unit cell which is the case in many insulators and molecular crystals. Therefore, the surrounding crystal cannot be matematically treated as a continuous background medium. One important consequence of that is the localization of Frenkel excitons at their respective sites in the crystal.[71,137]

Both kinds of excitons yield energetically well-defined states below the band gap energy E_{G} as shown in Figure 2.10 a for Wannier-Mott excitons. They are uncharged particles with a mass $m_{\mathrm{e}}^{\star} + m_{\mathrm{h}}^{\star}$ and translational center-of-mass motion as described in the following.

Electron Hole Pair Dynamics in the Two-Particle Picture

Figure 2.10 b illustrates the dynamics of electron hole pairs in the two-particle picture. Optical excitations either induce free or bound electron-hole pairs (excitons). The gray area is the phase space of free electron-hole pairs with enough excess energy to overcome the mutual Coulomb interaction. The discrete branches at lower energy describe excitonic states. Transferring concepts from the single particle picture, an electron-hole pair with some excess energy relative to the 1s exciton energy $E_{1\mathrm{s}}$ relaxes to the energetically lowest state, the 1s exciton state. That relaxation occurs predominantly via LO phonon emission and then via slow acoustic phonon scattering once the energy difference of the electron-hole pair to the 1s exciton is less than the energy of an optical phonon. While the relaxation mechanism in general follows the same steps as described in Section 2.2.1, there is one major difference such that the transition from the continuum in gray to one of the exciton branches in Figure 2.10 b is accompanied by the formation of a bound excitonic state of the electron-hole pair.[124]

Further, Figure 2.10 c displays in reference to b how the absorption spectrum of a semiconductor relates to the two-particle picture. That description includes continuum absorption as well as sharp excitonic resonances. Generally, the dispersion relation of light $c = \omega k$ is virtually vertical compared to the dispersion relation of an electron-hole pair. Where this line crosses excitonic branches in Figure 2.10 b, excitonic resonances appear in the absorption spectrum.

According to Elliott, the intensities of those peaks are not equal but decrease in intensity like n^{-3} with branch number n.[138] At higher energies, the light dispersion crosses the full range describing free electron-hole pairs. It is intuitive that in this range the absorption spectrum follows a $\sqrt{E}$-like continuous rise for the 3D example shown in Figure 2.10 c. The continuum absorption is related to the density of states discussed in Section 2.1.4.[122,139]

Quantum Confinement

Usually, electronic and optical properties of semiconductors do not depend on the size of the crystal. That, however, is only true as long as the crystal is large in terms of the following: The Heisenberg uncertainty principle claims that confining a particle with a mass m in a space Δx gives rise to an uncertainty in its momentum

$$\Delta p_x \sim \frac{\hbar}{\Delta x} \tag{2.33}$$

which results in a confinement energy

$$E = \frac{\Delta p_x^2}{2m} \sim \frac{\hbar^2}{2m\Delta x^2}. \tag{2.34}$$

That confinement energy becomes significant when it exceeds the thermal energy of the system. In other words, confinement effects occur when the dimensions of a semiconductor nanoparticle are comparable to the de Broglie wavelength λ_{dB} which is typically in the nanometer range. The effects of quantum confinement affect both, free carriers and excitons.[121]

First, the continuum absorption spectra change from 3D (bulk) to 0D systems (quantum dots) in analogy to the density of states (DOS) given in the Equations 2.19-2.22. The effect on excitons is more complex and explained in the following.

Due to the importance of electric field screening explained above, excitons are susceptible to changes in their dielectric environment. While in 3D bulk semiconductors, the Coulomb interaction is fully screened by the semiconductor itself (see Figure 2.11 a), that assumption is not true for systems with reduced dimensionality in one or more directions. Figure 2.11 b shows that the electric field lines of an exciton confined in a 2D system penetrate both, the

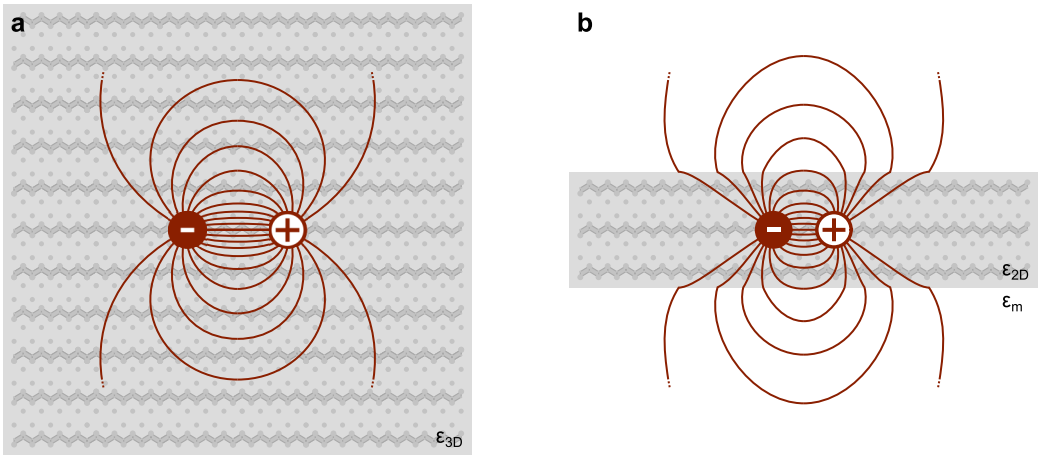

Figure 2.11: Excitons in 3D and 2D.
(a) Exciton formation in bulk semiconductors. The electric field built up between electron and hole is screened by the semiconductor itself with a dielectric constant characterizing the 3D semiconductor ε_{3D}. **(b)** Exciton formation in a 2D semiconductor NP. The electric field is not only screened by the semiconductor but with decreasing thickness, the field is partially screened by the surrounding medium. The dielectric constant of any surrounding medium ε_m is typically much smaller than that of the 2D semiconductor ε_{2D}.

semiconductor and the surrounding medium with a usually significantly smaller dielectric constant $\varepsilon_m < \varepsilon_{2D}$. Therefore, the field is increasingly screened by the low-ε surrounding when the thickness of the 2D semiconductor decreases. The less efficient screening leads to an increase in the exciton binding energy and a decrease in the exciton Bohr radius.[140] That trend is apparent from absorption spectra as the increase in exciton binding energy manifests itself in sharper and more pronounced excitonic resonances.[124,141,142] Finally, the Coulomb interaction, which is a function of electron-hole distance, is much stronger when electron and hole are brought closer together and thus the exciton binding energy increases. In the extreme case, a perfectly 2D system, the Coulomb potential yields a smaller exciton Bohr radius as illustrated by the 2D exciton wave function

$$\phi_{2D}(R) \propto \exp\left(-2R/a_X\right) \tag{2.35}$$

compared to the 3D case in Equation 2.31. Analogously, the exciton binding energy in a 2D system is four times larger compared to the respective 3D system.[136]

2.3 Polaronic Effects and Coherent Phonons

Section 2.2 illustrated the importance of carrier-phonon scattering for charge carrier dynamics. There are, however, effects that go beyond such scattering events. These include polaronic effects and coherent phonons. Both phenomena are consequences of strong carrier-phonon or carrier-lattice interactions and are described in the following.

2.3.1 Carrier-Lattice Interaction: Polarons

The above considers electrons and holes as free charges in a quasi-rigid lattice. Any lattice, however, with at least partially ionic bonds responds to the introduction of a charge carrier by re-positioning the atoms in the lattice. Electrons attract positively charged ions and repel negatively charged ones as exemplarily shown in Figure 2.12 a. The opposite is true for holes. Only when the energetic gains in terms of the ionic Coulomb interaction prevail over the energetic costs for inducing strain in the lattice, stable polarons are formed (see Figure 2.12 b).

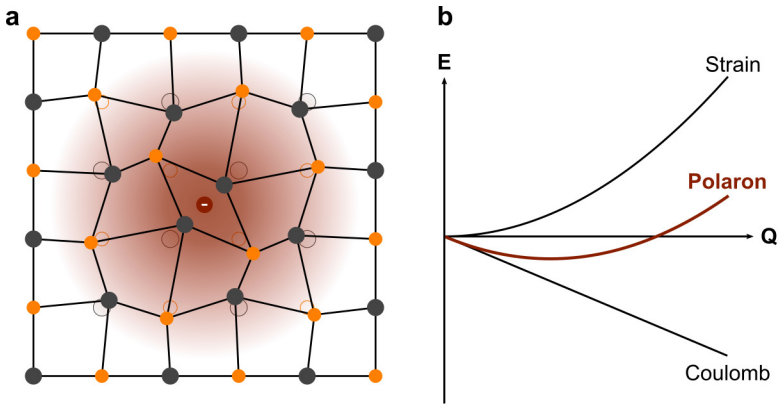

Figure 2.12: Polarons in inorganic crystals.
(a) A charge, an electron in this example, distorts its surrounding lattice when the bonds are (partially) ionic. It repels negatively charged ions (orange) and attracts positively charged ones (gray). The opposite applies for holes. The open circles indicate the atomic position in the ground state. **(b)** A stable polaron forms for the relative spatial distortion Q at which the energy gains due to Coulomb terms exceed the energy cost for the strain induced by repositioning the ions in the lattice.

Polaron Basics

Such a polaronic lattice distortion is mathematically equivalent to a superposition of typically longitudinal optical phonons. Therefore, any free carrier in such a lattice surrounds itself with a virtual phonon cloud that follows its motion.[143–145] The dimensionless quantity

$$\alpha_{\mathrm{e,h}} = \frac{e^2}{8\pi\varepsilon_0\hbar\omega_{\mathrm{LO}}}\sqrt{\frac{2m_{\mathrm{e,h}}^{\mathrm{r.\,l.}}\omega_{\mathrm{LO}}}{\hbar}}\left(\frac{1}{\varepsilon_{\mathrm{b}}}-\frac{1}{\varepsilon_{\mathrm{s}}}\right) \tag{2.36}$$

expresses the strength of the underlying Fröhlich coupling of carriers to LO phonons with the carrier masses in a hypothetical rigid lattice $m_{\mathrm{e,h}}^{\mathrm{r.\,l.}}$, the LO phonon energy $\hbar\omega_{\mathrm{LO}}$, and the low- and high-frequency dielectric constants ε_{s} and ε_{b}, respectivley. For non-polar crystals like Si, these are equal $\varepsilon_{\mathrm{s}} = \varepsilon_{\mathrm{b}}$ and $\alpha = 0$.[121] Coupling constants of typical inorganic semiconductors lie in the range of moderate polaronic interactions $0 \leq \alpha \leq 1$ and increase from partly covalent III-V over II-VI to highly ionic I-VII compounds as shown for selected examples in Table 2.2.

A polaron, dragging the lattice distortion along with itself, has a higher effective mass than a charge carrier in a hypothetical rigid lattice (r. l.):

$$m_{\mathrm{e,h}} = m_{\mathrm{e,h}}^{\mathrm{r.\,l.}}\frac{1}{1-\alpha_{\mathrm{e,h}}/6} \tag{2.37}$$

The distorted volume and thus the polaron radius r_{p} is given by

$$r_{\mathrm{p}}^{\mathrm{e,h}} = \sqrt{\frac{\hbar}{2m_{\mathrm{e,h}}^{\mathrm{r.\,l.}}\omega_{\mathrm{LO}}}}. \tag{2.38}$$

Table 2.2: Fröhlich coupling constants of Si, GaAs, ZnSe, and AgCl[146]

	Si	GaAs	ZnSe	AgCl
α_{e}	0	0.06	0.40	2.2

Polaron Formation

The relaxation associated with the lattice distortion lowers the self-energy of the system.[147–149] It does so by digging its own potential well described by the potential[150]

$$V_{\mathrm{p}}(r) = -\frac{e^2\,(1/\varepsilon_{\mathrm{s}} - 1/\varepsilon_{\mathrm{b}})}{r}. \tag{2.39}$$

That relaxation to an energetically favorable state brings along a reduction of the band gap E_{G} by

$$\Delta E_{\mathrm{G}}^{\mathrm{e,h}} = \alpha_{\mathrm{e,h}} \hbar\omega_{\mathrm{LO}}. \tag{2.40}$$

Altogether, polaron formation renormalizes mass and energy in (partially) ionic semiconductors.[69]

Such a formation takes its time. Typical formation times lie in the (sub-)picosecond timescale.[151,152] Generally, larger Fröhlich coupling constants α theoretically lead to longer polaron formation times.[153] This is also observed experimentally[151] and consistent with the fact that larger coupling constants lead to further dislocations of the individual atoms and the relaxation to lower energies. It is intuitive that this is associated with longer formation times.

In typical III-V semiconductors like GaAs, $\alpha_{\mathrm{e}} = 0.06$ is small, the polaron radius is much larger than the dimensions of the unit cell, and polaronic corrections to the carrier mass and the band gap are negligible (in the order of $\sim 0.1\,\%$).[146] They form so-called large polarons that spread over multiple unit cells. For polar materials with large coupling constants and small polaronic radii, the mathematical model used to derive the above fails as it assumes the medium to be a polarizable continuum. While it describes large polarons well, the small polaron effect in highly ionic crystals lead to self-trapping. The carriers get trapped in their own strong local lattice distortions.[121]

2.3.2 Coherent Phonons

The same coupling of carriers to their surrounding lattice that gives rise to polaron formation can potentially launch coherent phonons in polar semiconductors. Most mechanisms, like e. g. thermal excitation, create incoherent phonons. Under certain experimental conditions,

however, it is possible to obtain coherent phonons, especially by the use of femtosecond laser pulses with a pulse duration shorter than typical phonon periods. Such coherent phonons are often referred to as in-phase vibronic motion of atoms which helps for an intuitive understanding.[154] In a quantum mechanical description one treats coherent phonons in terms of coherent quantum states.

Coherent Phonon Basics

A single mode ($\mathbf{q}$) coherent phonon state is an eigenstate of the annihilation operator introduced in Equation 2.6:[155]

$$\hat{a}_{\mathbf{q}} \left|\alpha_{\mathbf{q}}\right\rangle = \alpha_{\mathbf{q}} \left|\alpha_{\mathbf{q}}\right\rangle . \tag{2.41}$$

Consequently, a general phonon coherent state is a phase-coherent superposition of number states[156,157]

$$\left|\alpha_{\mathbf{q}}\right\rangle = \exp\left(-\frac{\left|\alpha_{\mathbf{q}}\right|^2}{2}\right) \sum_{n_{\mathbf{q}}=0}^{\infty} \frac{\alpha_{\mathbf{q}}^{n_{\mathbf{q}}}}{\sqrt{n_{\mathbf{q}}!}} \left|n_{\mathbf{q}}\right\rangle . \tag{2.42}$$

Such coherent phonons can be created via different creation mechanisms, e. g. impulsive Raman scattering or displacive excitation.[154,158–160] Ultrashort laser pulses are a useful tool for this as the driving force must be faster than the oscillation period of the material.[161] Accordingly, from a mathematical point of view, applying the displacement operator $\hat{D}_{\mathbf{q}}\left(\alpha_{\mathbf{q}}\right)$ to the phonon vacuum state yields a coherent state

$$\hat{D}_{\mathbf{q}}\left(\alpha_{\mathbf{q}}\right)\left|0\right\rangle = \left|\alpha_{\mathbf{q}}\right\rangle . \tag{2.43}$$

They are Gaussian wavepackets with minimum-uncertainty travelling back and forth in the atomic potential which is approximated to be harmonic.[162]

Phonon dynamics obey similar concepts like charge carrier dynamics, including especially the conservation of energy and momentum. Many of the underlying processes involve the interaction of phonons and charge carriers which implies that their dynamics act on similar time scales. One of the most important differences is the fact that phonons do not obey fermion but boson statistics.[69]

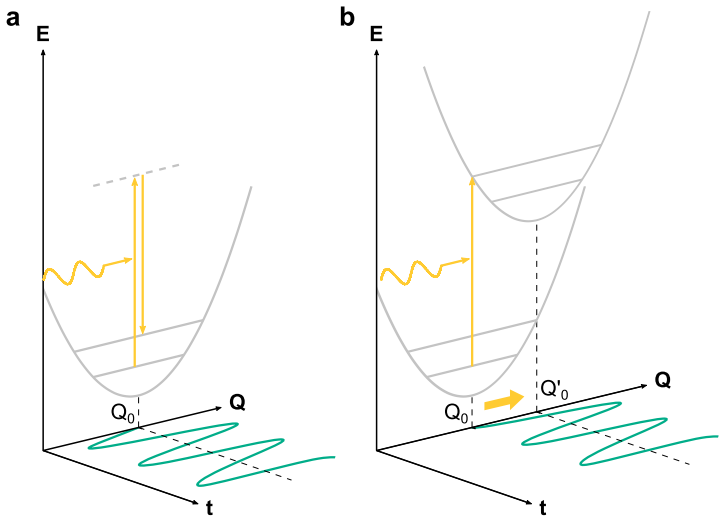

Figure 2.13: Excitation of coherent phonons.
(a) Impulsive excitation of coherent phonons through coupling to a virtual charge carrier population leads to a sine-like oscillation around the ground state equilibrium position Q_0. **(b)** Displacive excitation of coherent phonons creates a cosine-like lattice oscillation around the excited state equilibrium position Q'_0 as the atomic equilibrium position is shifted due to coupling to the photoexcited carriers.

Excitation of Coherent Phonons

There are two kinds of events that can create coherent phonons mathematically described by a phase-coherent superposition of number states (Equation 2.42).

First, impulsive excitation describes events in which an external force acts on the atoms in a crystal. Thus, the atoms are pushed out of their equilibrium position and oscillate around it. As the starting point is at the equilibrium position, the phonon amplitude follows a sine-like oscillation as illustrated in Figure 2.13 a. The most prominent example for an impulsive excitation of coherent phonons is impulsive Raman scattering reported in a large number of materials: The ions in a lattice are directly affected by the electric field of the incoming light.[158,163–166]

Second, displacive excitation creates coherent phonons in a different mechanism shown in Figure 2.13 b. An external stimulus, like e. g. an optical excitation, repositions the equilibrium positions of the atoms in a crystal lattice as described in Equation 2.43. When that repositioning is faster than the atoms can follow, they suddenly find themselves out of equilibrium and start oscillating around their new equilibrium position in phase with each other. The atoms

describe a cosine-like oscillation as their path begins at the position of full dislocation. Possible examples for displacive excitation include displacement via the deformation potential and surface field screening.[158,167–169]

In analogy to any other oscillation, the initial driving force in both mechanisms must act on shorter timescales than the oscillation itself to provide a coherent state. This is often the case as nuclei due to their high mass move quite slowly compared to the pulse length of femtosecond laser pulses.[170] Any mechanism that does not occur on such short timescales creates incoherent phonons. These involve most processes mentioned in Section 2.2.1, especially phonon emission during charge carrier relaxation. Generally, every initially coherent population dephases with time. Two pathways lead to the loss of coherence: inelastic scattering leading to the extinction of phonons described by a lifetime T_1 and elastic scattering during which the phase of a phonon changes associated with the lifetime $T_2^\star$. Altogether, this yields the dephasing rate[171]

$$\Gamma = \frac{1}{T_2} = \frac{1}{2T_1} + \frac{1}{T_2^\star}. \tag{2.44}$$

The underlying mechanisms will be introduced in the following.

Inelastic Phonon Scattering

Once created, phonons can decay. However, unlike optically excited electrons, no counterpart comparable to holes exists. Thus, their decay requires the interaction with other quasi-particles to conserve energy and momentum.

First, phonons can be absorbed through *phonon-carrier scattering* as shown in Figure 2.14 a. That describes the reverse process of emission of a phonon through scattering with a charge carrier. In the annihilation of a phonon in such a scattering event its full energy and momentum is transferred to the charge carrier (see Figure 2.14 b). The associated probability for such a scattering event increases with the charge carrier density.

Second, one phonon $(\omega, \mathbf{k})$ can decay into two (or more) phonons, $(\omega', \mathbf{k}')$ and $(\omega'', \mathbf{k}'')$, of smaller energy under the condition of conservation of energy $\omega = \omega' + \omega''$ and momentum $\mathbf{k} = \mathbf{k}' + \mathbf{k}''$ in a process called *anharmonic decay* (see Figure 2.15). As the name suggests, the harmonic approximation layed out in Section 2.1.3 is not sufficient to describe such

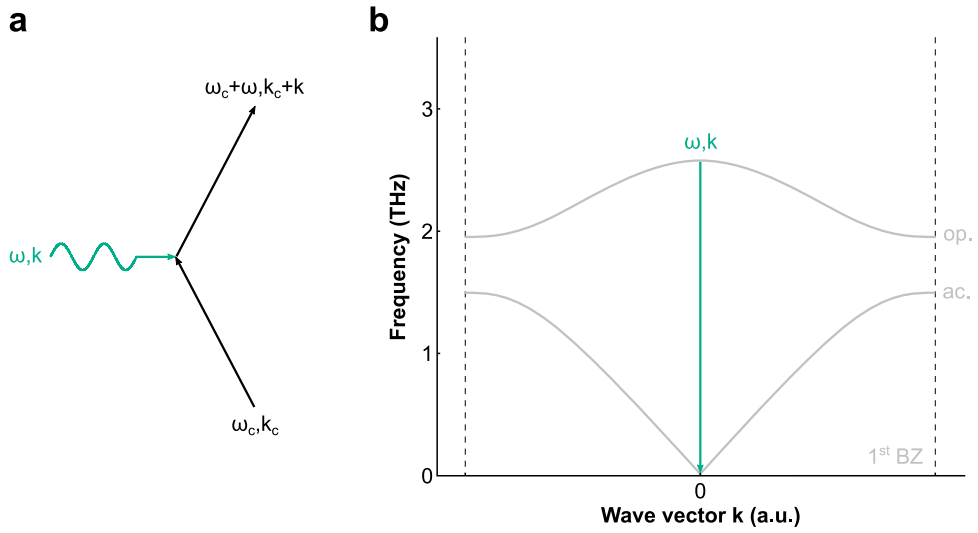

Figure 2.14: Phonon-carrier scattering.
(a) The example of the annihilation of a phonon (wave-like arrow) through absorption by a charge carrier (straight arrow) involves **(b)** the full transfer of energy and momentum to the charge carrier.

interactions. Processes involving three or more phonons are mathematically described by higher anharmonic terms of the Hamiltonian, including at least one annihilation and two creation operators. Typically, the first anharmonic term considering the decay of one optical phonon into two acoustic phonons describes anharmonic decay at temperatures at or below room temperature reasonably well:[172,173] The associated perturbation Hamiltonian

$$\mathcal{H}' = \sum_{\mathbf{q},\mathbf{q}',\mathbf{q}'',x} e^{i(\mathbf{q}+\mathbf{q}'+\mathbf{q}'')\cdot\mathbf{x}} V(\mathbf{q},\mathbf{q}',\mathbf{q}'')\, \hat{a}(\mathbf{q})\hat{a}^\dagger(\mathbf{q}')\hat{a}^\dagger(\mathbf{q}'') \tag{2.45}$$

includes the creation operator $\hat{a}^\dagger(\mathbf{q})$ $(N \to N{+}1)$ and the annihilation operator $\hat{a}(\mathbf{q})$ $(N \to N{-}1)$. Higher terms (quartic, quintic, ...) become dominant at much higher temperatures.[173–175] It is important to account for the occupation of phonon states in termal equilibrium: A perturbation can create an out-of-equilibrium occupation of the optical phonons $N = N_o + n$ with the equilibrium occupation N_o while acoustic states stay in equilibrium (N_a', N_a''). The relaxation rate of the out-of-equilibrium population n, which can be coherent phonons, is

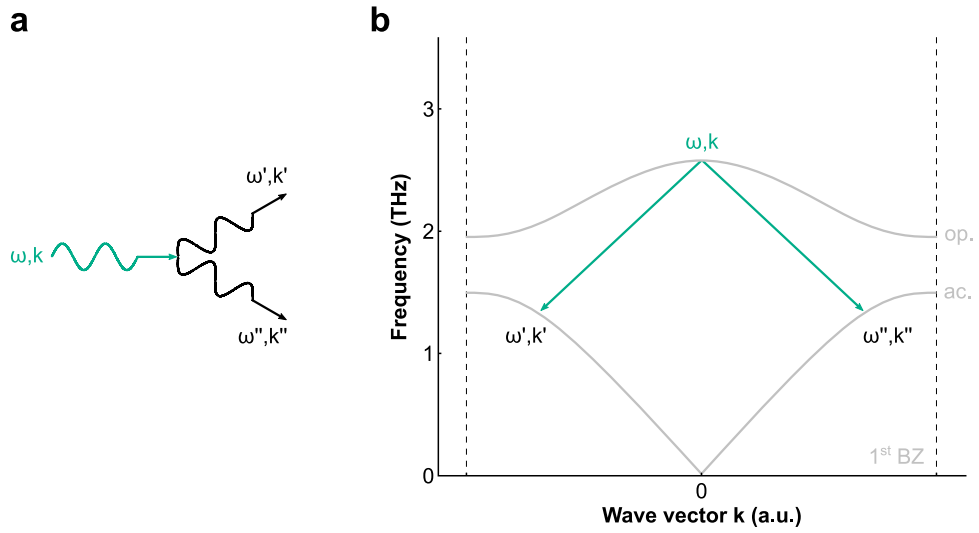

Figure 2.15: Anharmonic decay of one optical phonon into two acoustic phonons.
(a) Simplified schematic of a three-phonon scattering process as in **(b)** a Klemens-type (symmetric) decay[172] of one optical phonon into two acoustic phonons of equal energy and opposite wave vector.

given by[172]

$$\frac{dn}{dt} \propto \left[\left(N_o + n\right)\left(N_a' + 1\right)\left(N_a'' + 1\right) - \left(N_o + n + 1\right) N_a' N_a''\right] \tag{2.46}$$

$$\frac{dn}{dt} \propto n\left(1 + N_a' + N_a''\right) + \underbrace{\left[N_o\left(N_a' + 1\right)\left(N_a'' + 1\right) - \left(N_o + 1\right) N_a' N_a''\right]}_{\text{thermal equilibrium} = 0}. \tag{2.47}$$

Consequently, the anharmonic correction to phonon frequency ν and phonon dephasing rate Γ, mathematically represent the real and imaginary parts of the proper self-energy of a system, respectively:[176–179]

$$\nu(T) = \nu_0 - \nu_1 \times \left[1 + \frac{2}{\exp\left(\frac{\hbar\omega}{2k_B T}\right) - 1}\right] \tag{2.48}$$

$$\Gamma(T) = \Gamma_0 + \Gamma_1 \times \left[1 + \frac{2}{\exp\left(\frac{\hbar\omega}{2k_B T}\right) - 1}\right]. \tag{2.49}$$

As the name implies, understanding anharmonic decay relies on going beyond the approximation of perfectly parabolic (harmonic) interatomic potentials. Anharmonic terms introduce an asymmetry in the potential. Thus, according to the thermal distribution of bosons, these parameters are temperature dependent.

Absorption of a phonon through phonon-carrier scattering or the anharmonic decay of phonons abruptly decreases the amplitude of the collective oscillation. Thus, pure phonon decay in the absence of other dephasing mechanisms brings about a slow diminishing of the total oscillation amplitude with the rate $\frac{1}{2T_1}$.[154]

Elastic Phonon Scattering

Besides dominant inelastic scattering, elastic scattering poses a pathway for pure dephasing. Any defect introducing a perturbing potential, like point defects, grain boundaries and crystal surfaces, can act as a scattering center for phonon-defect scattering.[180] Especially point defects are known to make a significant contribution to the over-all phonon dephasing. The phonon-defect scattering rate

$$\frac{1}{\tau_{\text{defect}}} = N_{\text{defect}}\gamma(\omega_{\mathbf{q}}) \tag{2.50}$$

depends linearly on the number of point defects N_{defect} and the phonon-defect scattering rate $\gamma(\omega_{\mathbf{q}})$.[181] It is associated with the pure dephasing lifetime $T_2^{\star}$.

At this point, one cannot help but wonder what role charge-lattice interactions play in materials like BiOI. The possibly formed intrinsic electric fields indicate a strong coupling, which should decisively influence the charge carrier and lattice dynamics. A large number of effects in condensed matter physics are related to strong carrier lattice interaction, including superconductivity that relies on the formation of Cooper pairs.[182] There have also been reports linking Dember-fields[167,168,183] and surface fields[159,161,168,184] to the creation of coherent phonons. Additionally, the above raises the question how complex carrier-lattice interactions in anisotropic structures like BiOI affect charge carrier dynamics in terms of potential polaronic and many other effects related to carrier-phonon coupling.

3 | Materials and Methods

This chapter introduces the synthetic protocol of the studied materials, the light sources and experimental setups used for sample characterization, and especially the spectroscopic experiments of this work.

Firstly, it explains the synthesis of the BiOI nanoparticles and the characterization of their morphology and crystal structure via electron microscopy and X-ray scattering techniques. Secondly, it presents the method to measure their photocatalytic performance in terms of hydrogen evolution rate in a light-induced water-splitting experiment. Finally, this thesis, at its core, aims to answer relevant questions regarding the charge carrier dynamics, in particular in their interaction with light, via optical spectroscopy. This requires time-resolved spectroscopic techniques and ultrashort laser pulses. The following describes the time-integrated and time-resolved absorption spectroscopy in a so-called pump-probe configuration used in this work.

3.1 Materials and BiOX (X = Cl, Br, I) Synthesis

The synthesis of the bismuth oxyhalide nanoplatelets was developed and performed by my colleagues Viola Steidl and Tim Fürmann. The reagents bismuth (III) nitrate pentahydrate ($Bi(NO_3)_3 \cdot 5\,H_2O$, CAS: 10035-06-0), D-mannitol ($C_6H_{14}O_6$, CAS: 69-65-8), polyvinylpyrrodine (PVP K-25, $(C_6H_9NO)_n$, CAS: 9003-39-8), potassium chloride, -bromide, and -iodide (KX; X = Cl, Br, I; CAS: 7447-40-7, 7758-02-3, 7681-11-0), methanol (CH_3OH, CAS: 67-56-1), and ethanol (C_2H_5OH, CAS: 64-17-5) were purchased from Merck KGaA and used without further purification.

The BiOX NPs were prepared via a hydrothermal synthesis based on the protocol of Guan *et al.*[20] which optimized the approach of Xiong *et al.*[57] 197.2 mg of $Bi(NO_3)_3 \cdot 5\,H_2O$, the bismuth source, and a variable amount of PVP between 0 mg and 160 mg were dissolved in 5 mL of 0.1 M D-mannitol solution under vigorous stirring at 1200 rpm for 10 min. PVP is a water-soluble polymer made from the monomer N-vinylpyrrolidone[185] and acts as a surface ligand in this synthesis. 200 µL of half saturated potassium iodide solution (0.086 mmol KI) were added under further stirring for 15 min (1000 rpm). In a second step, the solution was transferred into a 20 mL autoclave to heat the sample at 160 °C for 3 h. After cooling to room temperature, the product was purified in four washing cycles, each followed by sedimentation via centrifugation at 10 000 rpm. The first washing cycle was performed in a 50:50 mixture of ethanol and de-ionized water. Pure de-ionized water was used for the washing cycles two to four. The product was then dispersed in 7 mL de-ionized water. In preparation for further experiments, the as-prepared dispersion was drop-casted onto a sapphire substrate.

3.2 Structural Characterization

The following section gives a brief overview of the methods used to characterize the samples investigated in this study regarding their composition, morphology, and crystal structure. A precise characterization of the morphology and the crystal structure is essential for the understaning of the findings from the spectroscopic experiments described in Sections 3.4 and 3.5. To determine various structural parameters, this work applied a combination of electron

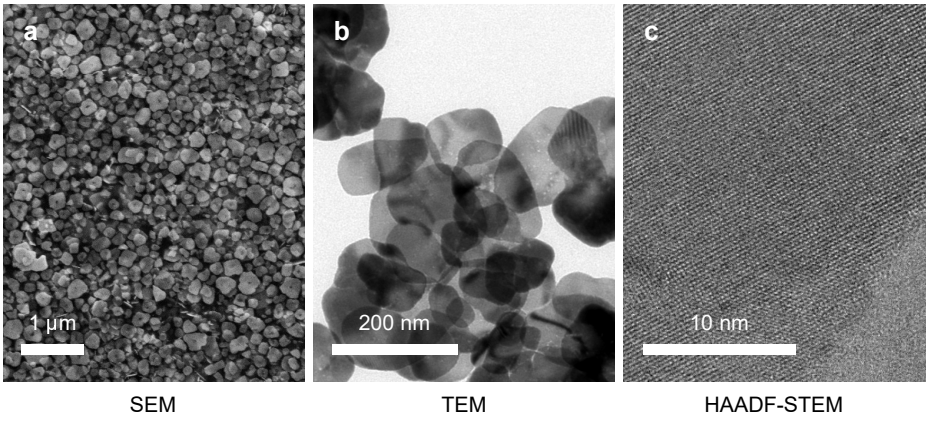

Figure 3.1: Electron microscopy.
(a) SEM image **(b)** TEM image and **(c)** HAADF-STEM image of the same BiOI NP sample showing the differences in the used microscopic techniques. Imaging the BiOI NPs from a comparable angle illustrates the strengths of each method: SEM images provide a surface scan that yields information on the clustering of the NPs. In contrast, TEM techniques, especially HAADF-STEM, lack that depth information but yield a significantly higher resolution. They can even reveal the crystal structure when the lattice planes are orthogonal to the electron beam axis.

microscopy and X-ray scattering techniques. In combination, they provide information from the micrometer-scale down to atomic resolution.

Nanoparticles measuring a few nanometers in each dimension are subject to this work. Abbe's diffraction limit with the numerical aperture NA postulates that light-based microscopes cannot resolve objects smaller than

$$d = \frac{\lambda}{2\mathrm{NA}} \tag{3.1}$$

with the numerical aperture NA.[186,187] To achieve a sufficient spatial resolution, transmission electron microscopy (TEM) was used in this study. The use of electrons instead of photons is crucial as they possess much shorter wavelengths. The de Broglie wavelength of an electron is given by

$$\lambda_{\mathrm{dB}} = \frac{h}{\sqrt{2mE}} \tag{3.2}$$

and measures 1 Å for a potential of 150 V.[72]

3.2.1 Scanning Electron Microscopy

Scanning electron microscopy (SEM) illuminates a film of the sample material on a silicon wafer and detects the so-called secondary electrons and back-scattered electrons from the surface of the substrate. Two different detectors detect these electrons: The in-lens detector collects directly scattered electrons, and a second detector the secondary electrons (see Figure 3.2 a). The following process creates such secondary electrons: The incident electron beam can remove electrons from the inner shell of single atoms in the sample. The remaining empty state is quickly re-occupied by an electron from an energetically higher state. That process releases energy that is often enough to emit weakly bound electrons from outer shells.

For any chosen mixture of the in-lense and secondary electron detector signals, a section of the sample is scanned in a raster plan to combine the information of position and signal intensity in a topographical image of the sample film surface with a resolution of down to 2 nm. Figure 3.1 a shows an exemplary SEM image of BiOI NPs.

A *Gemini Ultra Plus* (Zeiss) field emission scanning electron microscope with a nominal resolution of 2 nm was used. All SEM images shown herein were taken by my colleague Nicola M. Kerschbaumer.

3.2.2 Transmission Electron Microscopy

A *JEOL JEM-1011* TEM operating at acceleration voltages from 80 to 100 kV irradiates the sample, a thin nanocrystal film on a copper grid with an electron beam. TEM follows this fundamental working principle: An electron source accelerates an electron beam via a cathode and an anode. The collimated beam illuminates a specimen where the sample absorbs and scatters part of the electrons (see Figure 3.2 b). The 2D projection of the transmitted intensity profile is the measured by a CCD camera (see Figure 3.1 b for an example TEM image of BiOI NPs).[188,189]

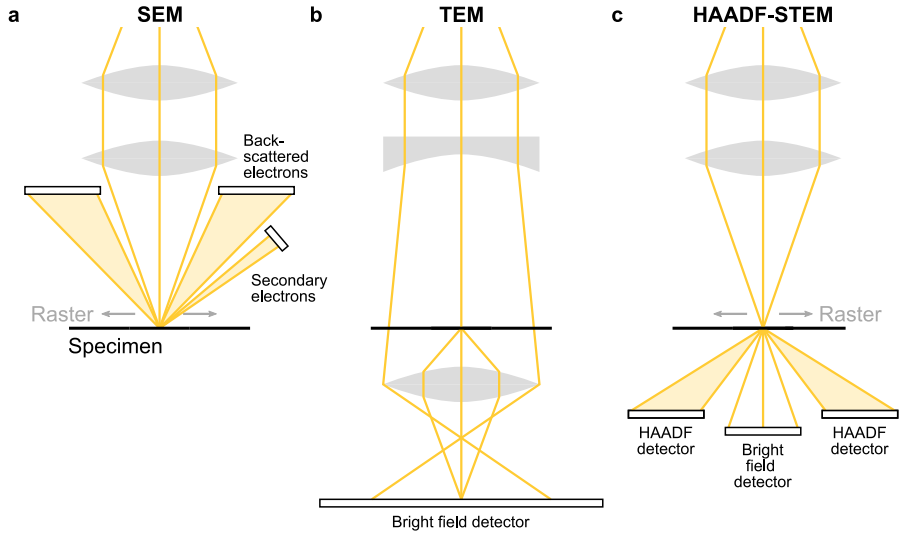

Figure 3.2: Electron microscopy techniques SEM, TEM, and HAADF-STEM.
Schematics of **(a)** SEM, **(b)** TEM, and **(c)** HAADF-STEM microscopes including the electron beam path (yellow), the specimen and the relevant detectors.

3.2.3 High-Angle Annular Dark-Field Scanning Transmission Electron Microscopy

High angle annular dark field scanning transmission electron microscopy (HAADF-STEM) works at a higher voltage of up to 300 kV and thus has shorter wavelengths and better resolution than a conventional TEM. The *Titan Themis* used for this work scans the region of interest following a raster plan to acquire the position-dependent intensity profile. It can even achieve atomic resolution when the electron beam is orthogonal to the crystal planes of the sample, as can be seen in Figure 3.1 c, the HAADF-STEM of an individual BiOI NP. All HAADF-STEM images shown in this work were taken by Dr. Markus Döblinger.

Generally, it acquires two sets of information as the incident electron beam interacts with the specimen via elastic and inelastic scattering: Besides elastically scattered electrons that contribute to the bright field image in analogy to conventional TEM, there are additional detectors in the wide-angle regime at up to 200 mrad to collect inelastically scattered electrons. As the intensity of those scattered electrons scales with the squared atomic number (Z^2), it contributes to high compositional sensitivity (see Figure 3.2 c).[190]

3.2.4 Wide-Angle X-ray Scattering

Wide-angle X-ray scattering (WAXS) experiments were conducted by my collaboration partners Kilian Frank and Dr. Bert Nickel at a combined wide- and small-angle X-ray scattering (WAXS & SAXS) molybdenum microfocus setup. After drying aqueous BiOI dispersion in an O-ring mask on a 25 µm Kapton foil, a second foil covers the remaining powder for transmission measurements: X-rays with an energy of 17.4 keV (0.710 748 4 Å) illuminate the as-prepared sample. A *Pilatus 100K* detector (Dectris) 22 to 26 cm behind the sample collects the signal by scanning a raster perpendicular to the incident beam covering a large q-range.

The *pyFAI* software package was used for azimuthal integration. The data were further analyzed in *python* 3.8.12 (*numpy, scipy, lmfit,* and *jupyter notebook* packages). The peak positions from Kandanapitiye, *et al.*[191] were taken for reference.

3.3 Photocatalytic Experiments

The photocatalytic efficiency of the samples studied herein is expressed in terms of evolved product per time and mass of the photocatalyst.

The photocatalytically active nanoparticles were dispersed in a mixture of water and the hole scavenger methanol in a 90:10 ratio and kept in a sealed cuvette (Hellma Analytics, *Type 117F-QS*). Prior to the experiment, the filled cuvette was purged with argon for three minutes through open-top screw caps with a rubber septum. A magnetic stirrer rotating at 500 rpm prevented sedimentation and kept the nanoparticles well dispersed.

The photocatalysts were tested under illumination with a xenon arc lamp (Horiba John Yvon GmbH). Its color temperature of 6200 K matches the solar temperature of 6500 K reasonably well. The lamp has an output power of 140 W and was placed 25 cm from the sample yielding a beam intensity of 140 mW cm^{-2}.

The photocatalytic reaction triggered by the incoming light produces gases like hydrogen and oxygen such that, after some time, the initially pure argon atmosphere in the cuvette contains a mixture of those gases. The exact composition, and therefore the hydrogen yield, was measured in time intervals of one to two hours. For that, a part of the cuvette atmosphere

was extracted through the rubber septum in the cuvette cap. It was then injected into a gas chromatograph *Shimadzu GC-2014* which guides the gases through porous columns. These columns separate the gases according to their different diffusion times through the walls of those columns. The final detection can then distinguish between and quantify the injected gases in terms of their respective fraction in the whole sample volume.

3.4 Time-Integrated Optical Absorption Spectroscopy

Optical spectroscopy is the central tool to study the optical properties of the BiOI NPs. Linear absorption spectroscopy investigates the initial absorption of light that stands at the beginning of any following process discussed in the context of this work. It is crucial to gain precise knowledge of that process, as it determines the subsequent charge carrier dynamics. Generally, the absorption of a photon excites an electron-hole pair. According to Fermi's golden rule (see Equation 2.27), such an optical transition is allowed when there is an initial and a final state with an energy difference corresponding to the photon energy. Photons with an energy higher than the band gap can excite so-called free electron-hole pairs leading to a continuous contribution to the absorption at energies above E_G. Bound electron-hole pairs, called excitons, manifest themselves in resonances at slightly lower energies, as explained in Section 2.2.2.

All absorption measurements discussed in this study are measured in transmission with a *Cary 60 UV-Vis* (Agilent Technologies) absorption spectrometer. A xenon flash lamp (80 Hz) provides a white light spectrum covering the spectral range from 190 to 1100 nm. A rotating grating (1200 lines/mm) is used to successively illuminate the sample with only one center wavelength with a band with of 1.5 nm at a time to scan the spectral range of interest (see Figure 3.3). The optical density (OD)of the sample, a dried thin film on a sapphire substrate or a nanoparticle dispersion in water, was controlled to be between 0.1 and 1. Using monochromatic light minimizes disturbances like scattering or emission. A sample detector and a reference detector simultaneously measure the transmitted intensity through the sample $I_S(\lambda)$ and the initial reference intensity $I_{ref}(\lambda)$, respectively. To correct for absorption of the substrate or the cuvette and the solvent, a baseline measurement of the transmitted intensity through a blank sample is taken, a clean substrate in this study. This baseline $I_B(\lambda)$ defines a

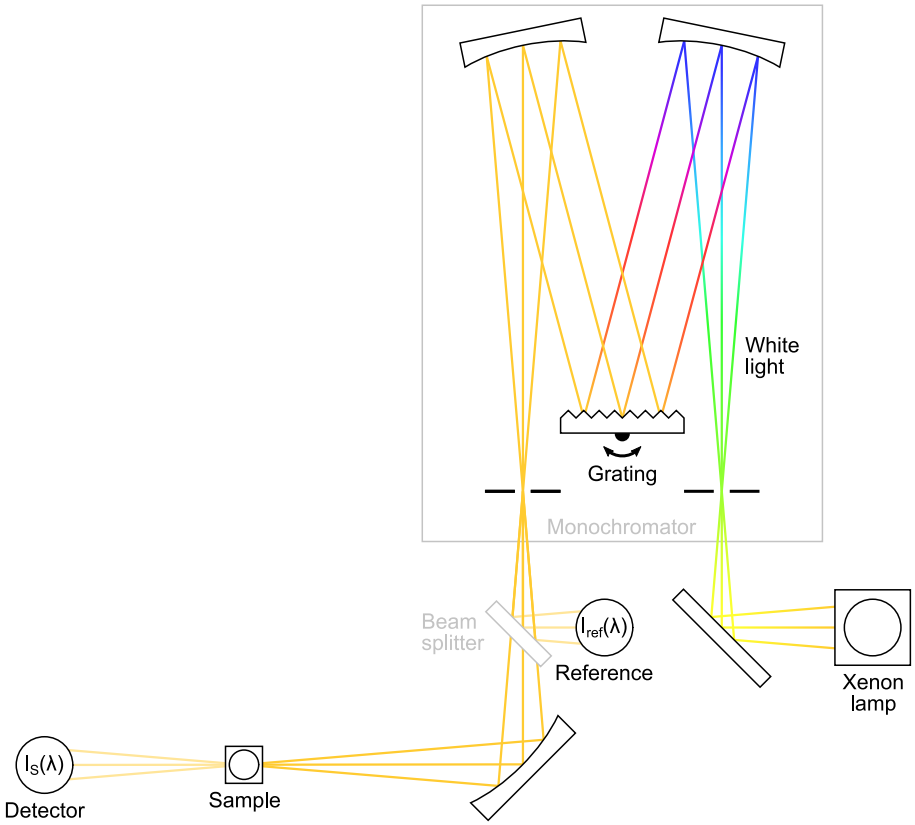

Figure 3.3: Time-integrated absorption spectroscopy.
For every wavelength, the initial intensity irradiating the sample $I_{\mathrm{ref}}(\lambda)$ is measured by a reference silicon diode detector and decreases in transmission through the sample, typically particles in solution or a film on a substrate. The final intensity $I_{\mathrm{S}}(\lambda)$ is measured by a second silicon diode detector.

correction $\beta(\lambda) = I_{\mathrm{B}}(\lambda)/I_{\mathrm{ref}}(\lambda)$. The baseline-corrected OD is defined by

$$OD(\lambda) = -\log_{10}\left(\frac{I_{\mathrm{S}}(\lambda)}{I_{\mathrm{ref}}(\lambda)\beta(\lambda)}\right). \tag{3.3}$$

It is important to note that in transmission experiments, besides optical absorption, also scattering and reflection contribute to the measured intensity. As a consequence, the term *optical density* is more accurate than *absorption* referring to the spectra discussed in this work. However, assuming scattering and reflection to be negligible, both expressions are interchangeable.

3.5 Sub-Picosecond Transient Absorption Spectroscopy

Besides time-integrated optical absorption spectroscopy, the experimental techniques include time-resolved measurements, often in combination with a cryostat for a controlled sample temperature. Precise temperature control over a wide range, especially reaching cryogenic temperatures, is necessary to gain insight into phonon-related effects.

In transient absorption spectroscopy, a so-called pump-probe experiment probes the change in OD as a function of the delay time between the pump and the probe pulse. A femtosecond pump pulse excites the sample and induces the charge carrier dynamics probed in that experiment. The high temporal resolution of the setup relies on ultrashort laser pulses.

The Light Source: Femtosecond Laser Pulses

In this study, a *Libra HE+* (Coherent) amplifier laser system emits ultrashort ($\sim$ 85 fs) laser pulses with a wavelength of 800 nm at a repetition rate of 1 kHz and a pulse energy of around 5 mJ. The whole amplifier laser system consists of five building blocks: a seed laser, a pump laser, a stretcher, an amplifier, and a compressor.

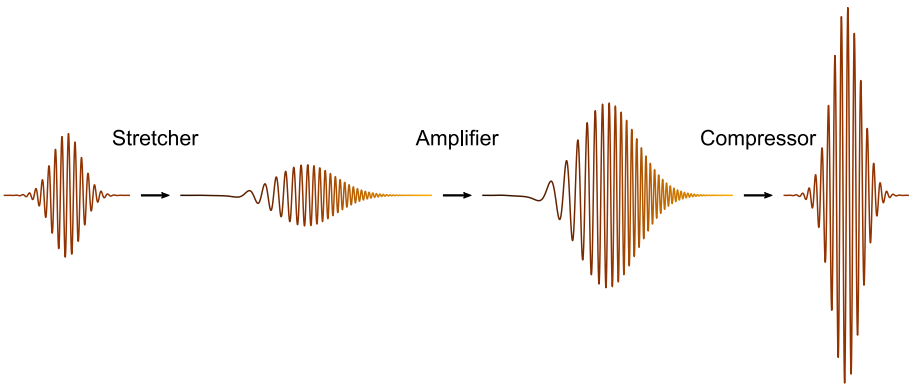

Figure 3.4: The concept of chirped pulse amplification.
Chirped pulse amplification consists of three steps: First dispersive optics, typically a grating or a prism, stretch an incoming laser pulse temporally by guiding different wavelengths along optical paths of different lengths. That reduces the pulse peak power and allows for amplification in a second step without losses due to non-linear effects. Finally, a second set of dispersive optics reverse the stretching and compress the amplified pulse to its original duration. Both, relative width and amplitude changes are depicted only schematically and are much larger in the amplifier laser system used in this work.

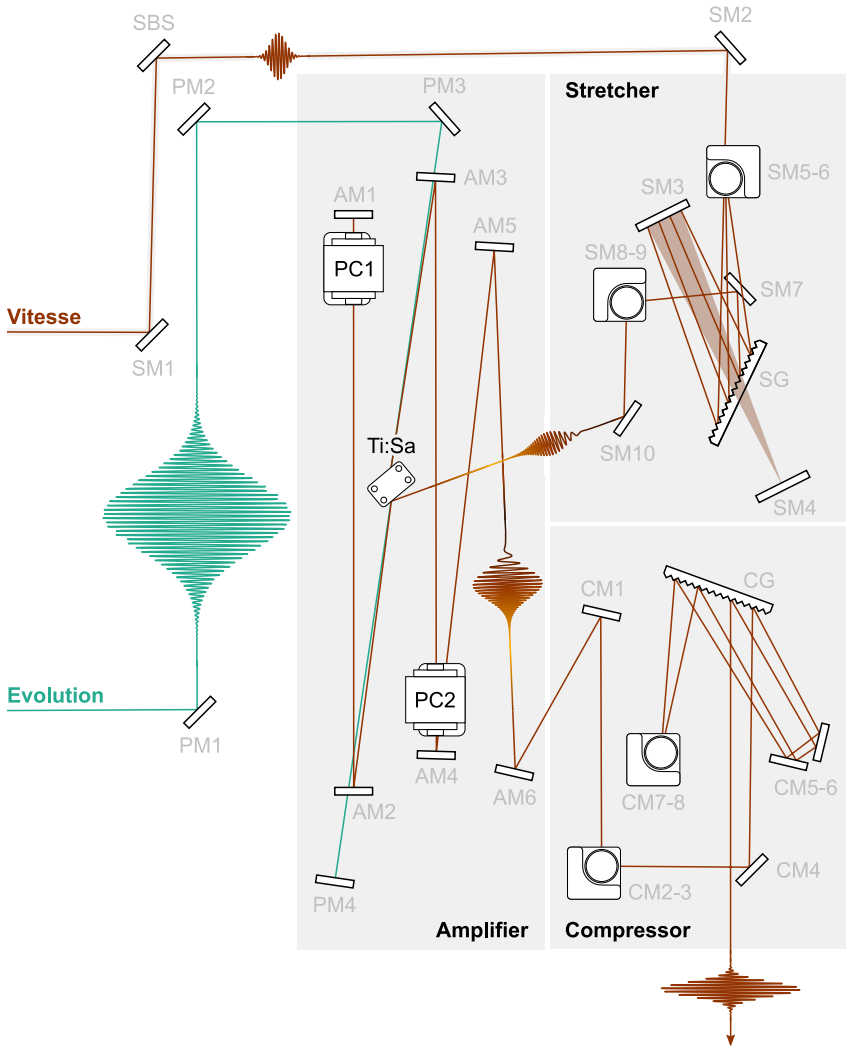

Figure 3.5: Ti:Sa amplifier laser.
The *Libra HE+* is comprised of five subunits to provide ultrashort laser pulses with a puls energy of 5 mJ and a repetition rate of 1 kHz: The 800 nm Ti:Sa seed laser *Vitesse* (red), the Q-switched 527 nm pump laser *Evolution* (green), a grating based stretcher unit, an amplifier cavity and a grating pased compression unit.

A titanium-sapphire (Ti:Sa) seed laser *Vitesse* (Coherent) provides a train of 800 nm ultrashort laser pulses with a repetition rate of 80 MHz. Within the *Vitesse*, a 532 nm continuous wave (CW) diode laser *Verdi* (Coherent), pumps a sapphire (Al_2O_3) crystal doped with Ti^{+3} ions. The Ti:Sa laser with the active Ti^{+3} ions in the transparent host material (sapphire) is a typical example for a solid-state laser. These pulses will be modified, as explained in the following, to fulfill the experimental requirements.

Table 3.1: Libra HE+ beam path by labels from Figure 3.5.

Unit	Beam path
Stretcher	SM1, SBS, SM2, SG, SM3, SM4, SM3, SG, SM5, SM6, SG, SM3, SM4, SM3, SG, SM7, SM8, SM9, SM10
Amplifier	AM1, PC1, AM2, Ti:Sa, AM3, PC2, AM4
Compressor	CM1, CM2, CM3, CM4, CG, CM5, CM6, CG, CM7, CM8, CG, CM6, CM5, CG, output port

This is done via chirped pulse amplification (CPA),[192] a technique that was awarded with the 2018 Nobel Prize in Physics.[193] This process is comprised of three steps, namely stretching, amplifying and compressing the pulse to its original length. This is schematically shown in Figure 3.4. In detail, a grating stretches each pulse to a length in the picosecond range by guiding the different wavelengths of the incoming laser pulse along optical paths of different lengths. The beam passes the grating four times, as shown in Figure 3.5. Thus, the pulse peak power decreases significantly, allowing further amplification in a second cavity, the femtosecond amplifier unit of the *Libra He+*. A Pockels cell (PC) selects only one out of 80,000 incoming pulses from the seed laser that enters that cavity. All other pulses are blocked which effectively reduces the repetition rate from 80 MHz to 1 kHz. The amplifier cavity contains a Ti:Sa crystal that is pumped by a Q-switched pump laser *Evolution* (Coherent) emitting 527 nm pulses with a duration of 120 ns and pulse energy of 20 mJ at a repetition rate of 1 kHz that matches the frequency of ultrashort laser pulses entering the cavity. Each seed pulse thus completes multiple round-trips in the cavity during which the temporally long pump pulse arrives and creates population inversion in the Ti:Sa crystal of the amplifier cavity. This lasting interaction leads to a step-wise amplification with every transmission of the seed pulse through the Ti:Sa crystal. When its pulse power saturates at ~ 5 mJ, a second PC releases the amplified pulse into the compression unit. There, in a process reverse to the stretching to the pulse, a grating compresses it to its original pulse duration of ~ 85 fs. Table 3.1 explains the exact beam path within the amplifier laser.

Ultrafast Optical Parametric Amplifier

The 800 nm pulses are typically not the wavelength of choice to excite the sample in a pump-probe experiment. An ultrafast optical parametric amplifier (OPA), the *OPerA Solo* (Coherent) is used to convert those pulses into other wavelengths in the range from 190 nm to 12 μm. The complex layout employs a succession of nonlinear effects to obtain the aspired wavelength. These include white light generation, sum and difference-frequency generation, and second harmonics generation (SHG). The beam path and the exploited effects vary depending on the output wavelength. Reference [194] explains the working principle in further detail. For this work, however, direct SHG that transforms the 800 nm pulses into 400 nm covers the narrow spectral range between the multiple resonances in the pump-probe spectra. Therefore, the OPA was only used for control measurements.

The Experimental Setup for Pump Probe Spectroscopy

Figure 3.6 schematically shows the whole transient absorption spectroscopy setup. The beam is split into two separate beams, the pump beam, and the probe beam: The pump beam is then either directed through a barium borate (BBO) crystal that converts the 800 nm pulses into 400 nm by SHG or the OPA as described above to access other wavelengths, in this work e. g. 300 or 500 nm. A chopper running at a frequency of 500 Hz transmits only every second pump pulse. A movable gray filter sets the excitation density of the pump pulses. Like in linear absorption spectroscopy, these measurements must keep the OD of the sample in the range between 0.1 and 1. At lower densities, the signal-to-noise ratio may decrease, and at higher values, it is not reasonable anymore to assume the excitation density to be constant along the direction of the beam in the excited sample volume. That assumption is, however, critical for the understanding of the signal as described in the next subsection. Consequently, the pump pulse excites the sample, onto which it is aligned, before, at the same time as, or after every second measurement of the OD by an incoming probe pulse, depending on the time delay set by the motorized delay stage. The population excited by the pump pulse then fully decays until, 1 ms later, the next pump pulse arrives. The sample is mounted onto an xyz-stage with micrometer screws to adjust the sample position in all three dimensions in

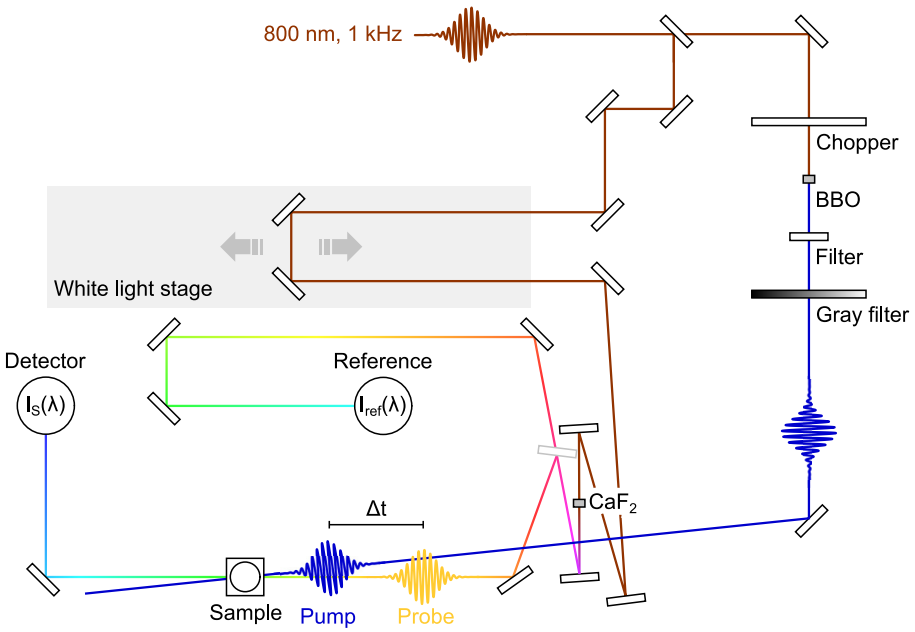

Figure 3.6: Transient absorption spectroscopy setup.
The transient absorption spectroscopy setup used in this work uses 800 nm femtosecond laser pulses with a repetition rate of 1 kHz. The incoming beam is split into two: the pump and the probe beam. The probe pulses are guided past a motorized white light stage that allows precise control of the time delay between the pump and probe pulse between ca. -500 fs and $3,000$ fs. Time $t = 0$ defines the moment when pump and probe pulse arrive at the same time. A CaF_2 crystal converts the monochromatic pulses into white light pulses shortly before it passes the sample. Every second pump pulse, on the other hand, is blocked by a chopper with a frequency of 500 Hz before a BBO crystal converts the incoming 800 nm pulses into 400 nm pulses via frequency-doubling. This guarantees that the sample is excited only every second time that the absorption is probed. The difference between each pair of measurements, one with and one without an excitation by the pump pulse, yields one data point $\Delta OD(\lambda, t)$. An additional filter blocks the remaining 800 nm light of the pump pulse and a gray filter is used to control the pump pulse energy.

measurements at room temperature. For temperature-controlled measurement, the sample as a dried film on a sapphire substrate sits inside a cryostat (Advanced Research Systems) that is controlled by a *Model 335 Cryogenic Temperature Controller* (Lake Shore Cryotronics).

The probe beam, on the other hand, is guided through a retroreflector mounted onto a movable stage. This allows for control of the time delay between pump and probe pulse of up to approximately 3 ns. The time at which the pump and probe pulse overlap temporally defines $t = 0$. The delay stage can move away from that position in controlled steps of ~ 0.13 fs, steps much smaller than the pulse width-limited time resolution of approximately 85 fs. In a CaF_2 crystal, the incoming 800 nm pulses are converted into a white light spectrum in the range from 350 to 900 nm (see Figure 3.7). At lower wavelengths, there is no sufficient light intensity

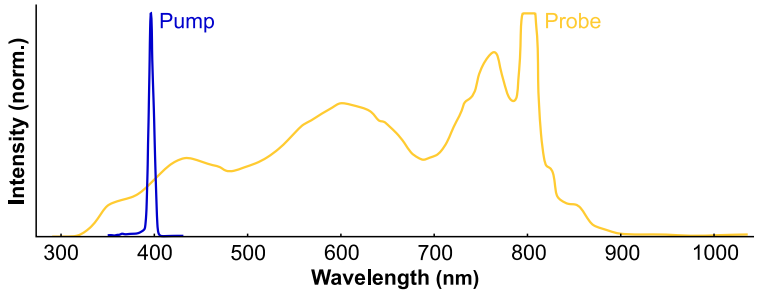

Figure 3.7: Pump and probe pulse spectra.
The CaF_2 crystal converts the 800 nm pulses into a spectrally broad white light probe pulse between 350 and 900 nm. The SHG in the BBO crystal provides the narrow spectrum of the pump pulse centered at 400 nm.

and at 800 nm the detector saturates due to the remaining high intensity of the Ti:Sa laser. The ultrashort probe pulses are focused onto the sample by a curved mirror and collected by an optical fiber leading to a spectrometer for the spectral intensity read-out. It is crucial to note that the cross-section of the probe beam at the sample is much smaller than that of the pump beam. Therefore, the excitation density is laterally virtually constant in the whole probed volume.

The Underlying Physics of Pump-Probe Spectroscopy

The pump pulse creates an electron density f_e in the CB and a hole density f_h in the VB (see Figure 3.8 a). Accordingly, due to phase-space filling (PSF), the presence of photoexcited electrons and holes reduces the absorption coefficient

$$\alpha = \alpha_0 \left(1 - f_\mathrm{e}\right)\left(1 - f_\mathrm{h}\right) = \alpha_0 \left(1 - f_\mathrm{e} - f_\mathrm{h} - f_\mathrm{e} f_\mathrm{h}\right) \tag{3.4}$$

compared to the ground state absorption α_0 (see Figure 3.8 b). In addition, stimulated emission is possible in the presence of photoexcited charge carriers (see Figure 3.8 c). As Fermi's golden rule does not specify any direction in terms of the coupling strength of two states, the associated transition probability is the same as for absorption and the contribution from stimulated emission is given by

$$e = \alpha_0 f_\mathrm{e} f_\mathrm{h}. \tag{3.5}$$

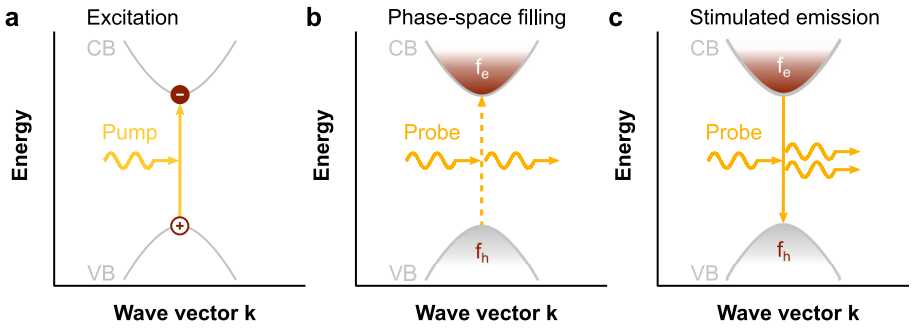

Figure 3.8: Fundamental physical phenomena in transient absorption spectroscopy. **(a)** excitation, **(b)** phase-space filling and **(c)** stimulated emission in semiconductors.

Therefore, the change in absorption

$$\Delta\alpha = \alpha - \alpha_0 - e = -\alpha_0 \left(f_\mathrm{e} + f_\mathrm{h}\right) \tag{3.6}$$

is directly proportional to the sum of electron and hole density for each wavelength λ and time t. In analogy to the change in absorption, the differential optical density ΔOD measures the change in OD induced by the excitation through the pump pulse. It is the difference between the signal measured by the probe pulse when the pump pulse is transmitted and the measured signal when it is blocked:

$$\begin{aligned}
\Delta OD(\lambda, t) &= OD_\mathrm{pump}(\lambda, t) - OD_\mathrm{no\ pump}(\lambda, t) && (3.7)\\
&= \log_{10}\left(\frac{I_\mathrm{no\ pump}(\lambda, t)}{I_0(\lambda)}\right) - \log_{10}\left(\frac{I_\mathrm{pump}(\lambda, t)}{I_0(\lambda)}\right) && (3.8)\\
&= \log_{10}\left(\frac{I_\mathrm{no\ pump}(\lambda, t)}{I_\mathrm{pump}(\lambda, t)}\right) && (3.9)
\end{aligned}$$

While that calculation may appear trivial, it illustrates why, in contrast to linear absorption spectroscopy, no baseline correction is required. Theoretically, one such pair of measurements would be sufficient to provide a complete dataset. In a typical measurement, however, hundreds to thousands of such pairs add up to one data point to guarantee a high signal-to-noise ratio. Furthermore, measuring $I_\mathrm{no\ pump}(\lambda, t)$ for each such pair at a frequency of 500 Hz reduces potential errors due to laser power fluctuations.

Further, there are additional effects beyond the considerations above. These include effects like band gap renormalization, photoinduced absorption (absorption of photons by photoexcited charge carriers), oscillatory modulations originating from the coupling of charge carriers to coherent phonons, etc. They can potentially give rise to additional contributions in the ΔOD spectrum that spectrally overlap with the PSF-induced resonances.

4 | Structural and Optical Characterization of BiOI Nanoplatelets

This chapter introduces the analyzed BiOI NPs which are known for their photocatalytic activity.[19,23–30] Despite the tremendous efforts the scientific community has undertaken to apply bismuth oxyhalides as photocatalysts, there is little understanding of the underlying fundamental physics. In particular, many theoretical predictions regarding their electronic and optical properties are yet to be tested experimentally.

Besides an indirect band gap[54,82] tunable in the visible range by varying the incorporated halide (see Table 2.1) bismuth oxyhalides bring along intriguing structural properties: Few experimental studies hint at the importance of the structural anisotropy of bismuth oxyhalides and how it translates to their optical and electronic properties.[8,116,195] This work exploits that layered crystal structure and its effect on the crystal growth to precisely control the morphology of BiOI NPs. On that basis, the electronic and optical properties, and finally the photocatalytic activity of BiOI are investigated with due regard to the underlying crystal structure.

This chapter revisits the physical concepts introduced in the first part of Chapter 2 with a focus on time-independent properties. It reports outcomes from Reference [196] that lay the foundation for the results presented in the two subsequent chapters.

4.1 Structure, Crystal Growth and Thickness Control

This work investigates BiOI NPs that were synthesized in a hydrothermal reaction as described in Section 3.1. Figure 4.1 a shows a HAADF-STEM image of stacked BiOI NPs in parallel orientation to the carrier substrate. Their semi-transparency indicates their small thickness of only a few nanometers. The Moiré-patterns[197] emerging from stacked, mutually rotated NPs show the high in-plane crystallinity despite being ultrathin. The NPs exhibit thicknesses in the nanometer range and lateral widths of up to hundreds of nanometers. In combination, this may be a first hint that the anisotropy introduced by the layered crystal structure of BiOI results in anisotropic crystal growth. HAADF-STEM images with atomic resolution provide insight into the in-plane structure of a NP (see Figure 4.1 b). The overlayed theoretical crystal structure matches the HAADF-STEM intensity profile extraordinarily well, which proves that the crystal layers are parallel to the large NP surfaces. Furthermore, this identifies the $[Bi_2O_2]^{2+}$ layers as the terminating surface layers, which is consistent with theoretical predictions[20,198] and the known binding mechanism of PVP as a surface ligand.[199] Apparently, the structural anisotropy translates into anisotropic crystal growth such that the in-plane growth along the strong covalent bonds significantly exceeds out-of-plane growth in the direction of the weak ionic bonds between the oppositely charged crystal layers.

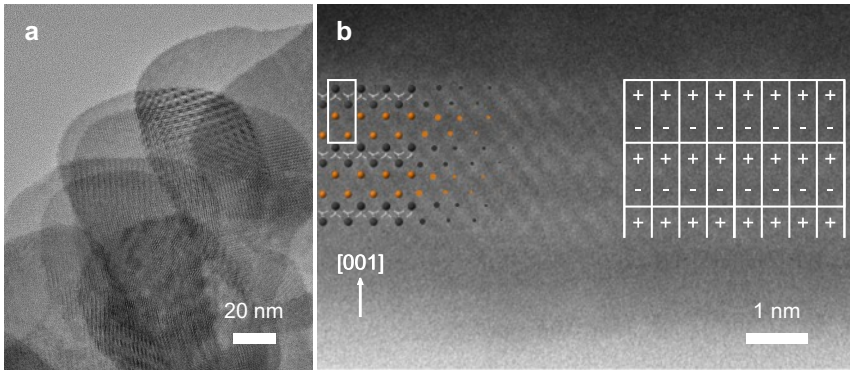

Figure 4.1: HAADF-STEM images of ultrathin BiOI nanoplatelets.
(a) A large scale image of multiple ultrathin BiOI NPs shows their lateral extents of hundreds of nanometers. They are extremely thin, which is apparent from the semi-transparency of the imaged NPs. Mutually rotated NPs exhibit Moiré patterns. **(b)** Imaging an individual NP standing normal to the substrate with a higher magnification reveals the in-plane crystal structure as indicated by the overlaid structure (with dark gray bismuth, light gray oxygen, and orange iodide atoms) and the inserted illustration of highlighted unit cells and their partial charges.

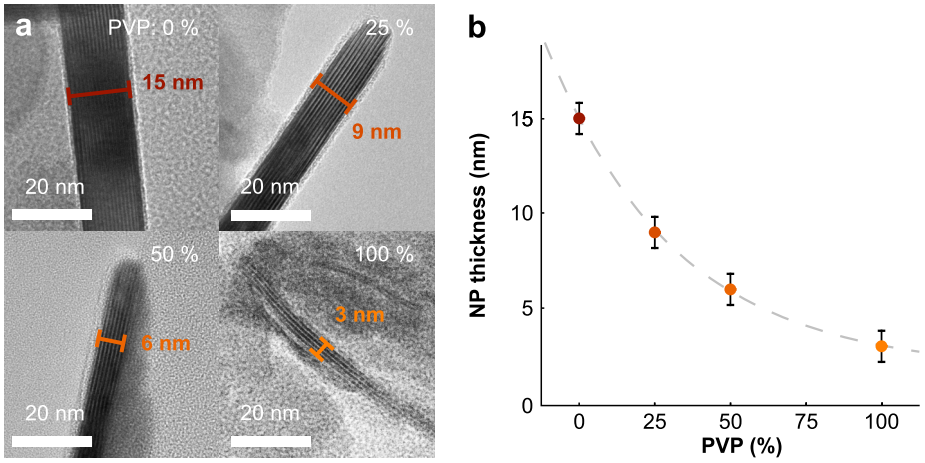

Figure 4.2: Thickness control of BiOI nanoplatelets.
(a) HAADF-STEM images of BiOI NPs standing normal to the substrate reveal the reduction of the NP thickness with increasing ligand content. **(b)** Ligand-controlled NP thickness read out from HAADF-STEM images with the gray dashed line as a guide to the eye.

To understand the connection between the crystal structure and the electronic and optical properties, it is crucial to gain control over the parameter of interest. In this work, the synthesis protocol enabled thickness tuning of the BiOI NPs on the nanometer-length scale by ligand passivation. PVP acts as a surface ligand that terminates crystal growth along one axis to obtain thinner NPs for higher amounts of ligand available during the hydrothermal reaction. The amount of ligand added to the synthesis controls the thickness in the order of some few unit cells. This is apparent from the TEM images of individual BiOI NPs in Figure 4.2 a standing normal on the substrate. The images reveal the NP thickness of only a few unit cells. In detail, the thickness ranges between 3 and 15 nm, which is equivalent to $\sim$ 3 to 17 monolayers (ML), and decreases with increasing PVP content as shown in Figure 4.2 b.

WAXS could provide further insight into the structural properties of BiOI NPs. Here, the important fact is that in contrast to TEM images, WAXS yields ensemble-averaged signals. Figure 4.3 a shows the WAXS spectra of NPs of different thicknesses for incident X-rays with $\lambda = 0.7107484$ Å as a function of scattering vector $q = 4\pi \sin(\theta)/\lambda$ with the scattering angle 2θ. Most significantly, the experimentally acquired spectra of the thick NPs match the simulated WAXS pattern for the tetragonal P4/nmm crystal structure of bulk BiOI (gray) in terms of peak positions and relative intensities.[191] For the highest PVP concentrations, a broad background

signal arises. The deviation from the theoretical prediction is associated with excess PVP. The black line in Figure 4.3 a shows the signature of pure PVP powder for the ease of reference.

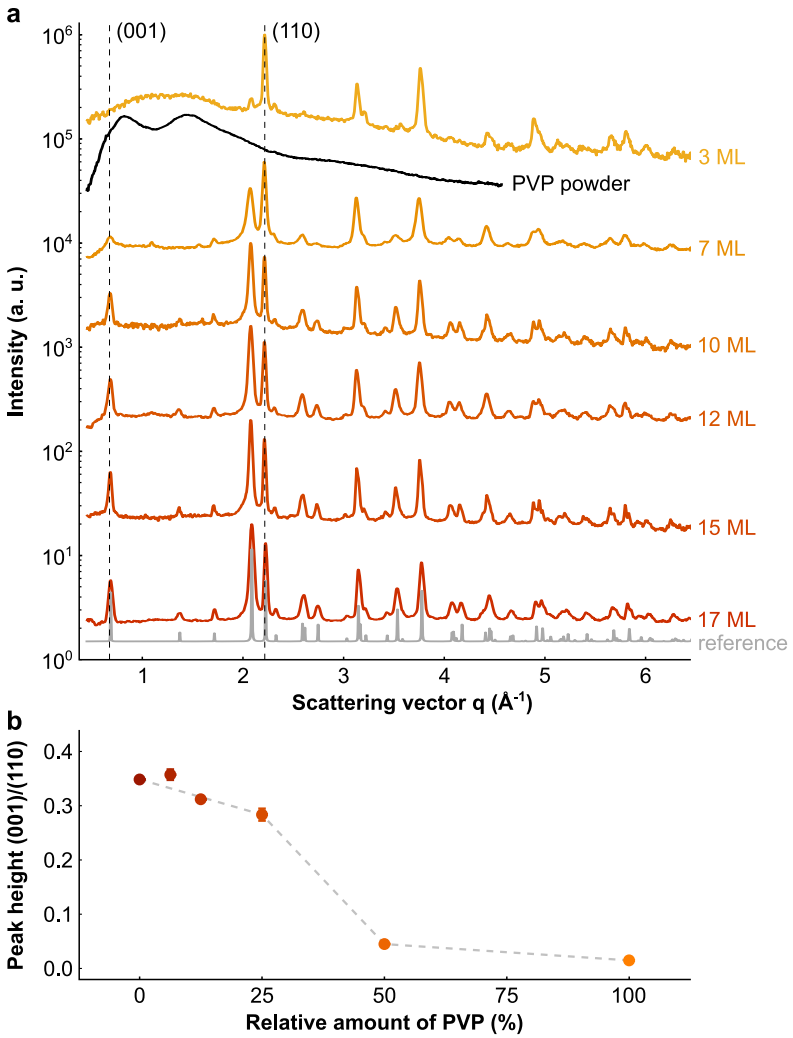

Figure 4.3: WAXS spectroscopy of BiOI nanoplatelets.
(a) WAXS spectra of BiOI NPs of thicknesses from 3 to 17 nm on a logarithmic scale. In addition, the reference in gray shows the theoretical prediction for bulk BiOI and the broad signal of PVP powder is shown in black. **(b)** The ratio of the out-of-plane (001) to the in-plane (011) peak height shows a decrease for an increasing amount of PVP available in the synthesis and thus thinner NPs. 0 % and 100 % define the range from 0 to 160 mg PVP used in the synthesis as described in the synthetic protocol.

A sophisticated analysis of the relative peak heights, namely the thickness dependence of the (001)/(110)-peak height ratio, sheds light on the ensemble-averaged relative thickness change. While the (001)-peak is a measure for the periodicity along the [001]-axis, the stacking direction in BiOI, the (110)-peak is linked to the in-plane periodicity. When the size of a

periodic system is reduced along one direction, the respective peak diminishes and broadens. Therefore, the (001)/(110)-ratio is a measure for the size along the [001]-axis normalized to the in-plane signal. That normalization is adequate as, due to the lateral size of the NPs, the (110)-signal strength is likely to reach the bulk limit for all NP thicknesses. For an increasing PVP concentration the ratio steadily decreases (see Figure 4.3 b) which substantiates two findings: Firstly, the average thickness of the BiOI NPs changes with the surface ligand amount for the whole ensemble. Secondly, the thickness is controlled selectively along the [001]-axis, the direction along which the oppositely charged layers are stacked and mutually bound to their neighboring layers by weak ionic bonds.

4.2 Absorption Spectra

Typical semiconductor NPs (e. g. CdS, CdSe, CdTe, or lead halide perovskites) of comparable thicknesses exhibit quantization effects: Charge carrier confinement in the direction orthogonal to the large NP surface results in a blue shift of the band gap and an increased exciton binding energy due to screening by the surrounding medium where the dielectric constant is significantly lower.[130,139,142,200]

The OD spectra of BiOI NPs of all thicknesses examined in this work are shown in Figure 4.4 a. The spectra exhibit a gentle absorption onset at the indirect band gap and a steeper rise at higher energies at which direct optical transitions from the VB to the CB are allowed. Generally, energetic bands in the band structure of BiOI are close to each other with typical energy differences of a few hundreds meV (see Figure 4.4 b). The absorption spectra are a superposition of multiple band-to-band continuum absorption contributions and the associated excitonic resonances.[138] These superpositions manifest themselves in two broad resonances in the energy range between 3 and 5 eV. Surprisingly, their positions are virtually thickness-independent (see Figure 4.4 a). This is in stark contrast to the pronounced blue shifts due to quantum confinement along that axis in other semiconducting NPs.[130,139,142,200] The resonances do, however, broaden with increasing NP thickness. Thicker NPs tend to accumulate in micron-sized agglomerates (see Figure 4.5). That is why they exhibit a more pronounced

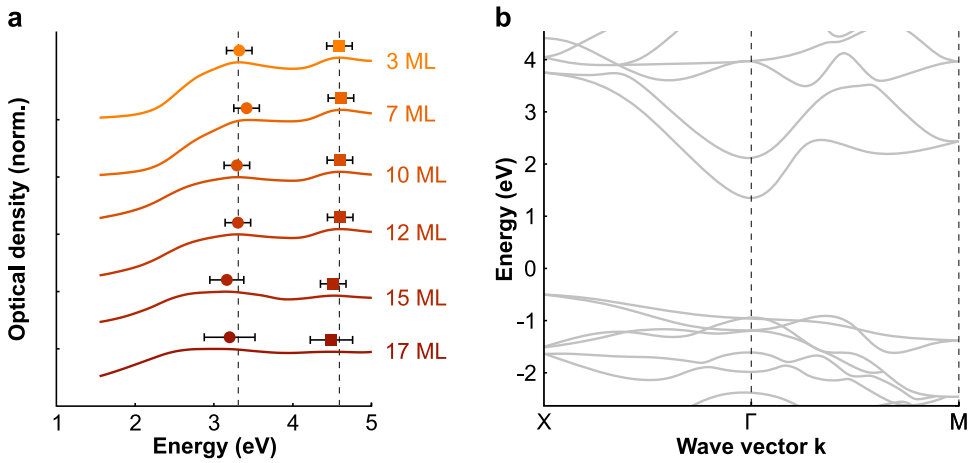

Figure 4.4: Thickness dependence of electronic and optical properties of BiOI nanoplatelets. **(a)** Thickness-dependent absorption spectra of BiOI nanoplatelets. BiOI NPs exhibit a gentle absorption onset at the indirect band gap followed by a steeper rise at energies of direct transitions between the VB and the CB. These manifest themselves in two broad resonances between 3 and 5 eV marked by a circle or square, respectively. The positions of these resonances are not thickness-dependent (see vertical dashed lines). Their width decreases with decreasing thickness. **(b)** In-plane band structure of BiOI (adapted from Wang *et al.*[28] - published by The Royal Society of Chemistry).

scattering-related tail in their OD spectra. Potentially, surface passivation by PVP reduces the mutual attractive interaction between the NPs and thus prevents their agglomeration.

It is crucial to put this into context with the in-plane band structure of BiOI from Figure 4.4 b which shows only in-plane bands. The electronic states are localized along the direction of the ionic bonds and therefore there is virtually no out-of-plane dispersion along the [001]-axis.[82,195] For that reason, size-reduction along the [001]-axis does not confine the localized charge carriers further and does not affect band positions. The decrease in the width of the absorption resonances might have two underlying reasons: Firstly, simulations from Wang *et al.* predict that the weak coupling between neighboring layers in BiOI induces an increasing number of in-plane bands proportional to the number of stacked layers rather than a dispersed out-of-plane band.[28] That would cause broader resonances for thicker NPs as experimentally observed. Secondly, in thinner NPs, the Coulomb interaction between electrons and holes is increasingly screened by the surrounding medium (water or air) with a significantly lower dielectric constant ε than BiOI. Less efficient screening brings about an increase in the exciton binding energy associated with sharper resonances in the absorption

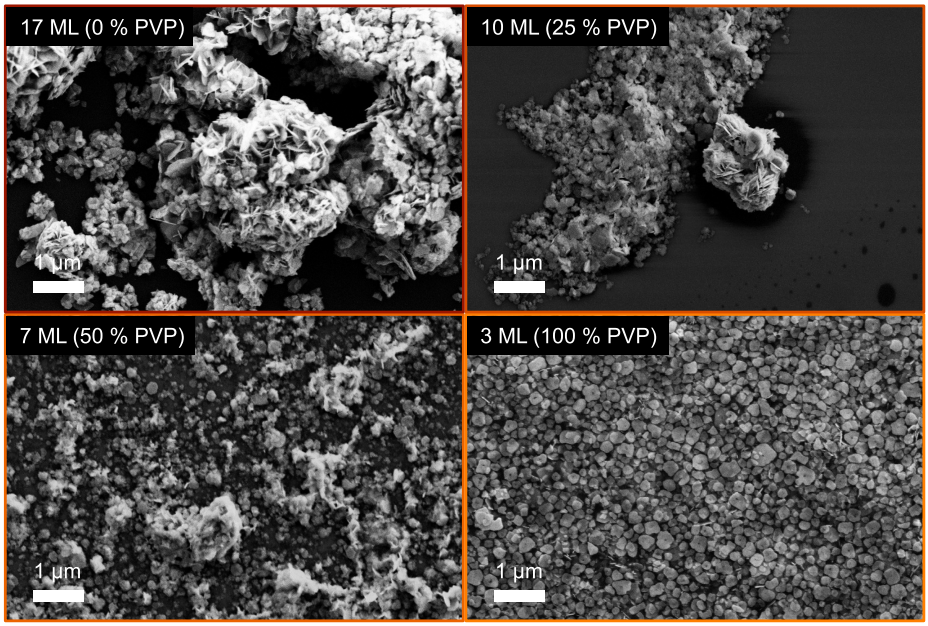

Figure 4.5: SEM images of thickness-controlled BiOI nanoplatelets.
Large-scale SEM images of BiOI NPs with 0, 25, 50, and 100 % PVP show that large agglomerates (>1µm) of many NPs form when no ligands are attached to the NP surface. These are reduced in quantity and size with increasing ligand concentrations until only individual NPs remain at 100 % PVP.

spectrum. The exciton binding energy of excitons confined to two dimensions

$$E^{\mathrm{X}}_{\mathrm{B,2D}} = 4E^{\mathrm{X}}_{\mathrm{B,3D}} < 5\,\mathrm{meV} \tag{4.1}$$

is four times larger than the respective 3D binding energy as explained in Section 2.2.2. This calculation takes the effective masses and dielectric constants calculated by Ran *et al.*[8] Such small bulk exciton binding energies in BiOI are the reason why no sharp excitonic resonances are to be seen in any of the OD spectra. While the charge carriers are confined to two dimensions, screening of their interaction occurs in all three dimensions. In the thinnest NPs, however, that picture ceases to apply as the screening increasingly occurs in the surrounding medium and sharper resonances become evident.

At this point, it is crucial to highlight that not only Ran *et al.*[8] but also Hoye *et al.*[116] consistently report extraordinarily high phonon contributions to the dielectric function resulting in a value of around 45. This leads to the small exciton binding energy as the ions can efficiently screen

Coulomb interactions[201] and further indicates that carrier-phonon coupling is strong in BiOI. Chapters 5 and 6 will investigate the importance of that coupling of carriers to the lattice.

In summary, the absorption spectra reflect that BiOI is a system of stacked 2D layers mutually bound by weak ionic forces. For that reason, quantum confinement-induced blue shifts do not occur with NP thickness reductions down to 3 nm. Despite the 2D character that brings along a fourfold increase of the exciton binding energy compared to a 3D system, the exciton binding energy is small due to the small effective in-plane masses and, most importantly, the large phonon contribution to the dielectric function of BiOI.

4.3 Photocatalysis

After the initial absorption of incoming light, BiOI can act as a photocatalyst when dispersed in water and produce hydrogen. Photoexcited charge carriers in most semiconducting nanoparticles in the size range of a few nanometers easily reach the surfaces. That is underlined by the fact that quantization effects occur in that size range.[202] In this context, size variations on that scale should have moderate effects on the photocatalytic activity of the system: Theoretically, the catalytical activity of a NP should not be limited by its thickness in the range from 3 to 17 MLs. Rather, it is expected to scale with the number of photons absorbed per NP and the accessible surface area not covered by the long ligands. If all that is true, the 17 ML NPs should outperform the 3 ML NPs in photocatalytic experiments.

In experiments testing BiOI NPs of different thicknesses, however, the opposite occurs. The photocatalytic results are normalized by mass of the catalysts, therefore by the absorption of the photocatalyst. Clearly, the thicker platelets use the absorbed photons less efficiently than the thinner ones (see Figure 4.6). Even though a 17 ML NP absorbs approximately five times more photons than a 3 ML NP, the H_2 evolution rate per platelet is only 1.65-times better. The thinner NPs obviously have a larger surface area. So the better performance of the thin NPs might originate either from the presence of more surface sites or an easier access to the surface (or both). However, the thin platelets are prepared at the higher concentration of PVP, that is expected to occupy the surface sites more effectively in the thin platelets, inhibiting the growth it the [001] direction. On this basis, one could anticipate worse photocatalytic activity of the

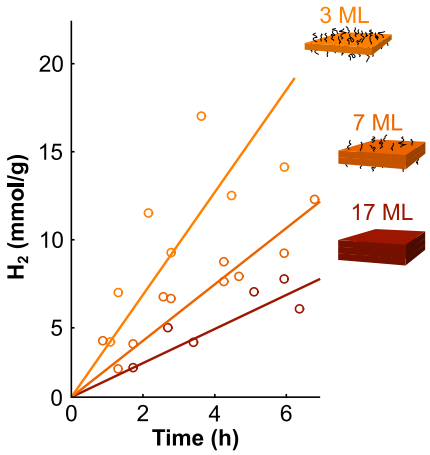

Figure 4.6: Photocatalytic hydrogen evolution of BiOI nanoplatelets.
The hydrogen (H_2) production per gram BiOI NPs shows a strong dependence on the NP thickness. Despite an increasing surface coverage by the ligand PVP, thinner NPs produce more H_2. The open circles indicate the measured data points fitted by the respective solid lines. For each NP thickness, multiple photocatalytic experiments were conducted which is why more than one data point may exist per point in time.

thin platelets. This is not observed in the experiments, implying that the strong thickness effect likely stems from the access to the surfaces of the NPs, wherein in thick particles the initial charge separation cannot promote the charges from the NP center to the particle surface. To understand this behavior, it is important to account for how the anisotropy of the crystal structure and bond character affects the charge carrier dynamics in BiOI NPs. These findings indicate that optically induced charge carriers in the bulk body of thick NPs rarely reach the reactive sites on the NP's surface where they can drive the photocatalytic reaction. This is consistent with the previously claimed carrier localization in [001]-direction. In thin NPs, however, most charge carriers are excited near the surface and are therefore not hindered from reaching the reactive surface sites in the absence of out-of-plane carrier delocalization. Consequently, these results show how BiOI unfolds its full potential as a photocatalyst in the form of ultrathin nanostructures.

5 | Optically Induced Coherent Phonons in BiOI Nanoplatelets

The preceding chapters explained that charge separation of optically excited electrons and holes is crucial for semiconductor applications in solar cells or photocatalysis.[15,203] That charge separation is a key process that must not only overcome their Coulomb interaction,[204] it must also be maintained for sufficiently long times for the carriers to reach the sites to fulfill their purpose, e. g. to drive a chemical reaction at the reactive sites for photocatalysis. In particular, it is crucial to prevent geminate recombination of photoexcited charge carriers. Heterostructures that separate carriers across interfaces are a typical approach to achieve this goal.[205–208] However, this may also introduce additional recombination pathways due to complicated system architectures.[205] This naturally brings the focus to semiconductors that are capable of the intrinsic separation of electrons and holes.

Alternating oppositely charged $[Bi_2O_2]^{2+}$ *and double* X^- *layers stack along the [001]-axis of BiOX with ionic bonds between these layers and covalent in-plane bonds. This structure might build up an electric field between neighboring layers,[49,51,54,83,209,210] which could have the potential to separate photoexcited electrons and holes, a process beneficial to catalytic reactions. Bismuth oxyhalides are indeed often used for photocatalytic water splitting,[211,212]* CO_2*-reduction,[213] and waste degradation.[18,213,214] Due to their photoactivity, bismuth oxyhalides are even applied in cancer photodynamic cancer therapy.[33,34] In BiOX NPs, charge separation would be especially beneficial as their large surfaces are orthogonal to the [001]-axis, the direction of the potential built-in field. Thus, field-induced charge separation would direct the charges to the closest reactive surface sites.[30,52,210,211,215,216] Even though the idea had emerged that electric fields might play that advantageous role in BiOX photocatalysts, there was no proof of that phenomenon, yet. Spectroscopic techniques like Terahertz spectroscopy[217] or pump-probe spectroscopy[218,219] are potential tools to gain insight into such phenomena. This chapter addresses the question of whether an electric field-induced separation of electrons and holes occurs in BiOI NPs and is based on the work published in Reference [220].*

5.1 Linear and Transient Absorption Spectra

Linear Absorption Spectrum

The previous chapter explained thickness-dependent changes in the absorption spectra of the indirect semiconductur BiOI (see the band structure in Figure 5.1 a). For the following discussion, it is expedient to recall the absorption spectrum of the 3 ML BiOI NPs shown in Figure 5.1 b. It exhibits a gentle absorption onset at below 2 eV followed by two broad resonances in the energy range between 3 and 5 eV.

These observations can be directly linked to the band structure in Figure 5.1 a. The initial rise starts at the energy of the indirect band gap of approximately 1.8 eV. It agrees well with the theoretically predicted E^2-like onset for indirect semiconductors. At the energy threshold for direct transitions, a steeper rise follows which marks the onset of the broad resonances that seem to be incompatible with the band structure at first sight. However, the close-lying bands in the band structure, especially in the valence band, result in energetically close-lying

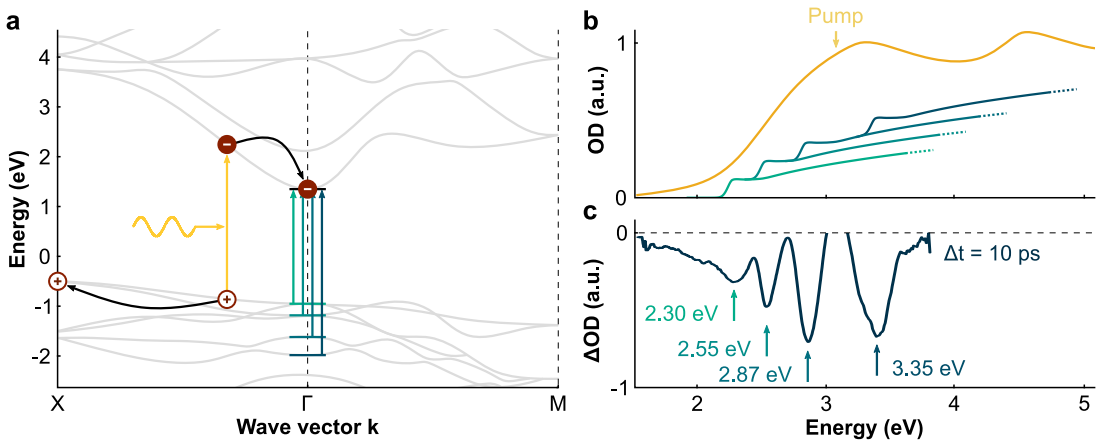

Figure 5.1: Absorption in bismuth oxyiodide.
(a) Band structure of BiOI with a corrected band gap (adapted from J. Wang *et al.*, Reference [28] - published by The Royal Society of Chemistry.) with an illustration of the electron-hole separation in k-space after optical excitation. The blue to green arrows indicate the four lowest energetic transitions that are affected by the occupation of the CBM by excited electrons at the CBM. **(b)** The linear absorption spectrum as well as potential underlying contributions relating to the band-to-band transitions sketched in (a) are plotted to illustrate how the band structure relates to the measured absorption. **(c)** The differential optical density spectrum at $T = 4$ K, probed 10 ps after excitation by a 400 nm pulse, reveals four resonances due to photobleaching of the four optical transitions shown in (a) by photoexcited electrons at the CBM.

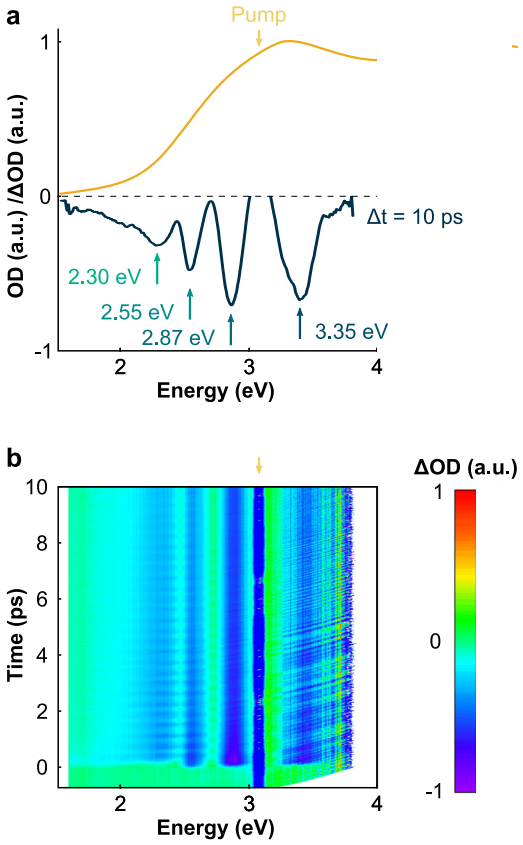

Figure 5.2: Chirp-corrected heat map of ΔOD in first 10 ps.
(a) The OD and ΔOD spectra are identical to the ones previously shown and are only displayed for the ease of reference. **(b)** The heat map of the ΔOD according to the color scale on the right. The four resonances in (a) can be clearly distinguished. The qualitative shape of the spectrum is virtually unaffected by changes in the first 10 ps after the initial build-up at $t = 0$.

optical transitions. This suggests that overlapping contributions from multiple band-to-band transitions form the extinction spectrum. In detail, contributions from continuum absorption from different band-to-band transitions and the corresponding excitonic resonances at lower energies add up to the measured signal. Selected contributions from direct transitions to the CBM are sketched qualitatively in Figure 5.1 b to illustrate the above. After the initial optical excitation, predominantly in a direct optical transition, electrons relax to the CBM at the Γ-point and holes to the VBM at the X-point (see Figure 5.1 a.).

Transient Absorption Spectrum

That explanation of the OD spectrum in relation to the calculated band structure was tested via transient absorption spectroscopy, as described in Section 3.5. Upon excitation by an ultrashort 400 nm laser pulse with a pulse energy of 1 µJ at $T = 4$ K, the optical density is reduced at four distinct energies as shown exemplarily by the ΔOD spectrum at a time delay of 10 ps between pump and probe pulse.

These energies match the energies of optical transitions from the VB to the CBM as sketched in Figure 5.1 a. Photoexcited electrons quickly relax to the CBM. Due to the partial occupation of the available states, the probability of further transitions from any other state to the CBM is reduced by a factor of $(1 - f_e)$ compared to the system in its ground state with f_e denoting the Fermi-Dirac distribution of electrons.[131] This is referred to as PSF and results in the negative ΔOD resonances at the energies of optical transitions from the VB to the CBM. Four such transitions at 2.30, 2.55, 2.87, and 3.35 eV lie in the probed energy range. This can be seen best at a cryogenic temperature of $T = 4$ K where reduced homogeneous broadening reveals clearly separated resonances. Besides the width of the observed resonances, the $T = 4$ K spectrum is representative for all temperatures up to 300 K. As BiOI is an indirect semiconductor, electrons and holes occupy states at different points in reciprocal space. The energy threshold for direct transitions at the X-point, the location of the VBM, is much higher than at the CBM. Consequently, PSF by the holes affects only direct transitions far in the UV outside of the spectral range probed in this experiment.

It should be noted that the ΔOD spectrum at $t = 10$ ps in Figure 5.1 c is representative for the full dynamics in the first picoseconds - the time-range of interest for the following discussion (see Figure 5.2). Furthermore, ΔOD spectra taken at different pump energies (300 nm and 500 nm) do not vary significantly from the spectrum for 400 nm excitation.

Transient Absorption Changes on the Nanosecond Timescale

The normalized time traces in Figure 5.3 show the transients for the four resonances from Figure 5.1 c. At the moment of excitation, the signal amplitude rises to its maximum within the time of the pulse duration. The subsequent decay as electrons and holes recombine is

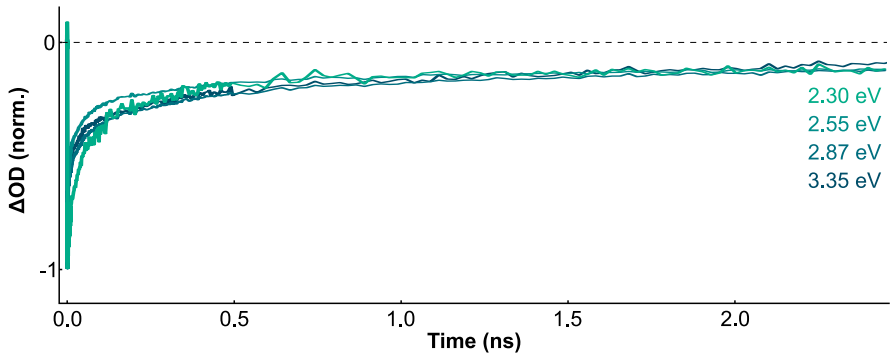

Figure 5.3: Normalized transient differential optical density of BiOI at T = 4 K.
The four transients at the energies of the resonances in the ΔOD spectrum, 2.30, 2.55, 2.87, and 3.35 eV, are virtually the same for the first 2.5 ns after excitation by an ultrashort 400 nm laser pulse with a pulse energy of 1 µJ.

much slower on the order of nanoseconds. It is striking that the normalized transients at the energies of the four PSF resonances show virtually the same evolution in time on the nanosecond timescale. This is perfectly consistent with the fact that all four resonances result from PSF through the same electron density. While the amplitudes of the resonances differ, the qualitative decay for all four of them scales with $f_e(\mathbf{k}_{\mathrm{CBM}})$. At high excitation densities, an initial fast decay may occur due to multiple carrier interactions like Auger-processes as explained in Section 2.2.1. Once many-carrier interaction events at short times after excitation have decreased the overall carrier density, the decay is slow as recombination in an indirect semiconductor requires the absorption or emission of a phonon for momentum conservation.

Up to this point, the understanding of the spectroscopic data requires no electric field for any physical model. It is, however, necessary for the following discussion of the ultrafast charge carrier dynamics.

5.2 Ultrafast Field Screening by Photoexcited Charge Carriers

The ultrafast dynamics revealed in the ΔOD transients shown in Figure 5.4 a can be understood as the superposition of two contributions: (i) A slowly varying transient due to PSF follows a steady decay. In addition, there is (ii) a damped temporal oscillation. Figure 5.4 b displays that oscillatory modulation after subtracting the PSF-related black fit in Figure 5.4 a. Both contributions exhibit a sudden rise at $t = 0$ when the pump pulse excites the sample.

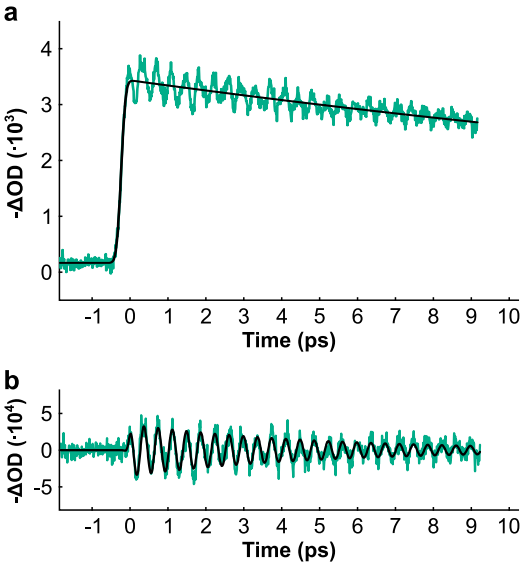

Figure 5.4: Differential optical density transient at 2.30 eV.
(a) The full transient at $T = 4\,\mathrm{K}$ in the first picoseconds after excitation by an ultrashort $\lambda = 400\,\mathrm{nm}$ pump pulse at $t = 0\,\mathrm{ps}$. The black fit represents the underlying contribution from PSF. **(b)** The temporal modulation after subtraction of the black fit in (a) takes the form of a damped temporal oscillation.

These findings from the transient at cryogenic temperatures and the further discussion are representative for temperatures up to room temperature. Temperature-related changes include only moderate variations in the oscillation frequency and dephasing rate as discussed in detail in Section 5.3.

The Fourier-transformed signal in Figure 5.5 a reveals two underlying frequencies at 2.7 THz and 4.6 THz. These are the frequencies of optical phonons in BiOI, suggesting the creation of coherent phonons by ultrashort laser pulses. Interestingly, a comparison with the theoretical study of Talirz *et al.*[75] reveals that out of all optical phonon modes, the two that are closest to the measured frequencies follow a clear pattern of vibronic motion: All atomic dislocations of the coherent phonon modes excited by an ultrashort laser pulse in BiOI oscillate only along the [001]-axis, the stacking direction of the alternatingly charged crystal layers. The back and forth motion is depicted by the individual snapshots of one full oscillation cycle in Figure 5.5 b. The dislocations illustrated by the sine-waves in the background are exclusively along the (vertical) [001]-axis. That implies that whatever mechanism creates these coherent phonons must act along that axis and thus relates to the anisotropy introduced by the crystal structure.

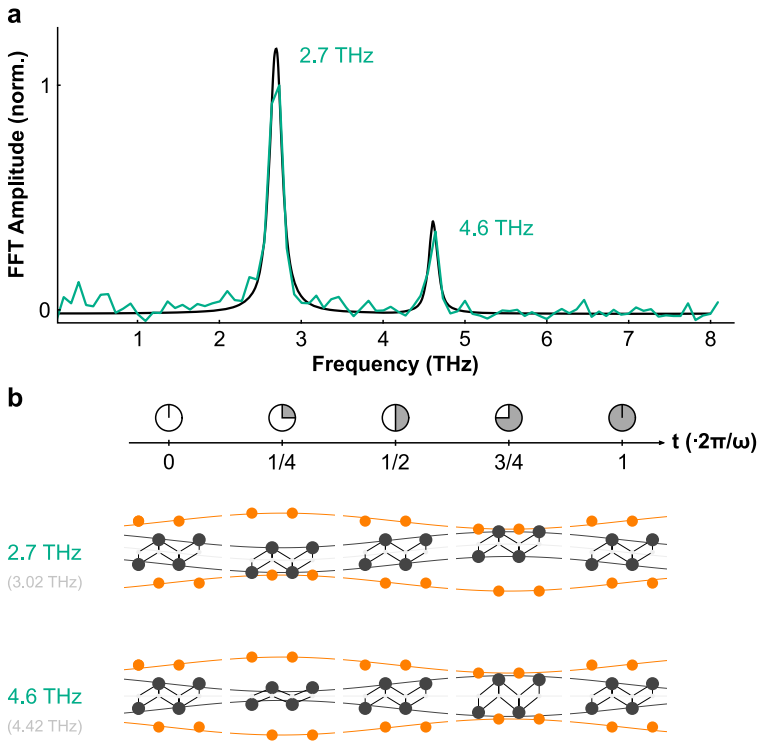

Figure 5.5: Fourier-transformed differential optical density transient at 2.30 eV.
(a) Two resonances, at 2.7 THz and 4.6 THz, mark the frequencies of the excited coherent phonons in BiOI. The data (green) were fitted by two Lorentz-peaks (black). **(b)** The energetically closest phonon modes predicted by Talirz *et al.*[75] are at 3.02 THz and 4.42 THz, respecively. The associated atomic motions next to the resonances involve only vertical displacements which correspond to motion along the [001] crystallographic axis. These modes are shown for two unit cells each at different times during the oscillation. The low-frequency oscillation describes the vibration of the oppositely charged layers against each other. The high-frequency mode corresponds to a 'breathing' mode in which the layers expand and contract periodically.

As the initial stimulus must be faster than the coherent oscillation itself, it is ultrafast, taking less than $(4.6\,\mathrm{THz})^{-1} \approx 220\,\mathrm{fs}$.

Interestingly, the photoinduced coherent phonon frequencies are virtually independent of the pump pulse energy. For many other materials, like tellurium or pure bismuth, optical excitations promote an electron from a bonding to an anti-bonding state. Such mechanisms weaken the bonds, and thus the lattice softens. As a consequence, the phonon frequency decreases with increasing photoexcited charge carrier densities.[166,221–223] The fact that no such shift occurs in BiOI is consistent with the fact that the VBM and the CBM have an anti-bonding character (see Section 2.1.4).

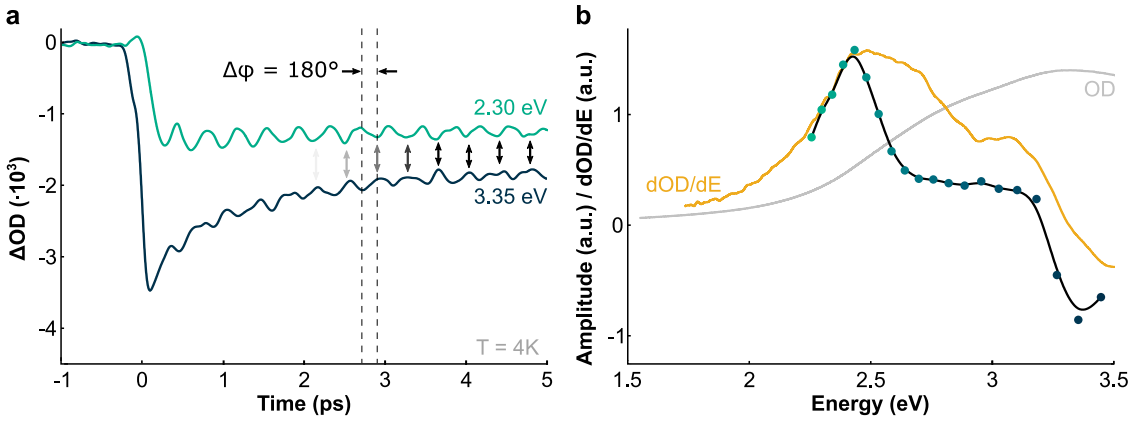

Figure 5.6: Phase and amplitude of ΔOD modulation.
(a) Selected transients at 2.3 eV where $\mathrm{d}OD/\mathrm{d}E$ is positive and at 3.35 eV where $\mathrm{d}OD/\mathrm{d}E$ is negative exhibit a phase difference of $\Delta\phi = 180^\circ$ measured at $T = 300$ K. **(b)** The energy-dependent amplitude of the oscillation (black) with the pre-sign accounting for the relative phase resembles the derivative of the OD (orange).

The ionic displacements associated with the coherent phonons result in a time-variant oscillating modulation of the band gap with the frequency of the excited coherent phonons. That band gap variation translates to the observed changes in ΔOD. This is consistent with the observation that the oscillation is apparent in a broad wavelength range as indicated in Figure 5.2. In detail, it is 180° phase-shifted between energy regions with a positive derivative compared to those with a negative derivative of OD (see Figure 5.6 a). Furthermore and in consistency, the amplitude of the oscillation resembles the first derivative of the OD spectrum as shown in Figure 5.6 b.

Creation of Coherent Phonons

Coherent phonons can either be excited via impulsive or by displacive mechanisms.[154,158–160] As discussed in Section 2.1.3, the initial phase is an essential indicator for the respective excitation pathway. Figure 5.7 shows the transient in the picoseconds before and after the excitation by the pump pulse at $t = 0$ that was reconstructed from the autocorrelation function. An oscillation maximum marks the onset of the oscillation at that time. As discussed in Section 2.3.2, this implies that coherent phonons are created in a displacive process that shifts the atomic equilibrium positions by coupling to a photoexcited charge carrier population. Vice versa, this rules out impulsive excitation via Raman scattering that would bring along a

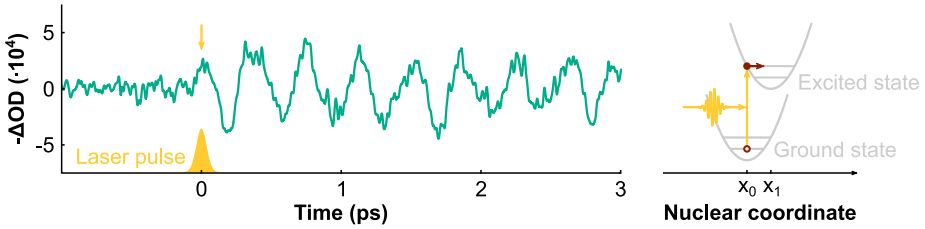

Figure 5.7: Initial phase of coherent phonons in BiOI.
The temporal osciallatory modulation of the differential optical density starts with a maximum at $t = 0$, the moment of excitation by the pump pulse (illustrated in yellow).

sine-like modulation of the optical density. It should, however, be noted that potential time delays discussed in this analysis closely approach the temporal resolution of the experiment. Therefore, a control experiment confirmed that 800 nm excitation does not release coherent phonons - even at significantly higher pump powers. This substantiates the claim that the phonons couple to real, not virtual, charge carrier populations.

Considering both, the anisotropy of the coherent phonons and their displacive excitation through coupling to photoinduced charge carriers is consistent with the following: An ultrashort pump pulse excites electrons from the VB to the CB. These free charges are separated in the built-in electric field between neighboring crystal layers. The associated ultrafast screening of the electric field alters the potential energy landscape of the semiconductor, which repositions the equilibrium positions of the atoms in the lattice. These are much heavier than the charge carriers and cannot follow this ultrafast process.[170] Rather, after the ultrafast screening of the electric field, the ions suddenly find themselves out of equilibrium and begin to oscillate around their new equilibrium position in phase with each other. This collective motion is referred to as coherent phonons.

Electric Fields in Semiconductors

In the presence of electric fields, phenomena like the ultrafast Stark[224] effect or the Franz-Keldysh effect[225,226] occur in semiconductors. However, these effects do not manifest themselves in BiOI for the following reasons: They appear when an external electric field introduces a slow variation in comparison to the periodicity of the crystal. In BiOI, however, the built-in

dipolar electric field changes on the exact same length scale as the dimension of the unit cell along the [001]-axis. It can therefore not be treated as a slowly varying perturbation in space.

An ultrafast Stark shift that would lead to a derivative-like ΔOD spectrum is not observed in the spectrum in Figure 5.1 c.[227–229] The Franz-Keldysh effect describes how an external field causes an oscillatory shape of the absorption spectrum above the band gap following an Airy function. Screening of the internal field would thus result in a spectrally oscillatory ΔOD spectrum including a succession of positive and negative signals at the Airy function extrema.[230] In contrast to that, the recorded spectrum exhibits only negative ΔOD peaks. Furthermore, the Airy oscillations decay in amplitude and increase in frequency for higher energies.[231] For BiOI, the opposite trend proves true for both amplitude and frequency. In light of the above, it is apparent that neither the ultrafast Stark effect nor the Franz-Keldysh effect but PSF induces the measured ΔOD resonances.

5.3 Dephasing of Coherent Phonons

Once created, the coherent phonon population begins to dephase with time. As described in Section 2.3, two scattering mechanisms contribute to the loss of coherence: Firstly, phonons are conserved in elastic scattering events associated with the time constant $T_2^\star$, but they experience a phase shift. After such a phase jump, they are incoherent with the remaining coherent phonons. Secondly, phonons can be annihilated (or created) in inelastic scattering events described by a lifetime T_1. The dominant annihilation mechanisms are (i) the anharmonic decay of one optical phonon into two or more acoustic phonons and (ii) absorption of a phonon by a charge carrier via phonon-carrier scattering. Together, these two mechanisms are the major contributors to the total dephasing rate $\Gamma = 1/2T_1 + 1/T_2^\star$ and result in the temporal exponential decay of the ΔOD oscillation amplitude.

5.3.1 Phonon-Phonon Scattering: Anharmonic Decay of Phonons

Especially the anharmonic decay of one optical phonon into two acoustic phonons under the conservation of energy and momentum, illustrated in Figure 5.8 a, contributes significantly to the total dephasing rate. The full phonon dispersion relation in Figure 2.5 shows all the

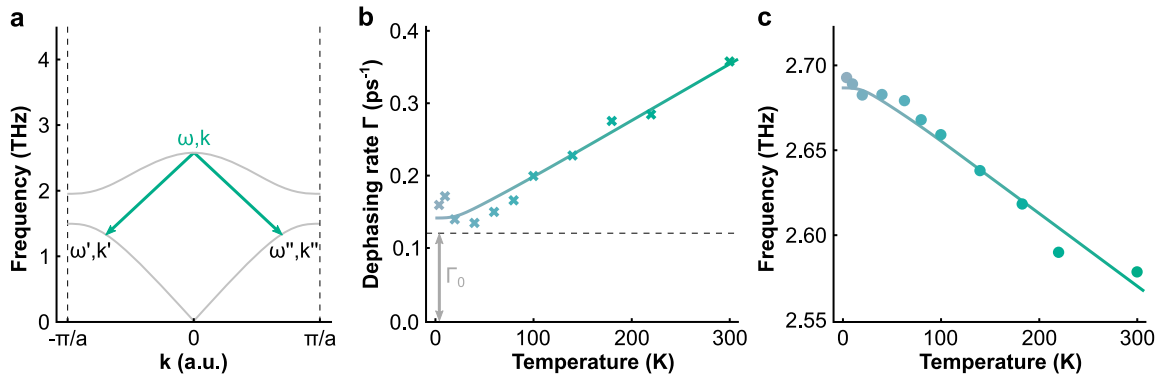

Figure 5.8: Anharmonic decay of optical phonons in BiOI.
(a) Schematic representation of the symmetric anharmonic decay of an optical phonon into two acoustic phonons of equal energy and opposite wave vectors. The temperature-dependent coherent phonon **(b)** dephasing rate and **(c)** frequency.

phonon modes that an optical phonon can decay into. While the harmonic approximations can model many properties of phonons, it cannot address processes like such decays. The cubic term of the anharmonic Hamiltonian describes three-particle processes like the decay into two acoustic phonons. Mathematically, this is expressed through one annihilation and two creation operators. Quartic, quintic, and higher anharmonic terms modeling many-body processes involving four or more phonons are reported to be less likely and become dominant only at higher temperatures than in this study.[172–175]

Both the total dephasing rate Γ (see Figure 5.8 b) and the phonon frequency (see Figure 5.8 c) are temperature-dependent. As calculated by Klemens,[172] the cubic term reflecting anharmonic effects to the vibrational potential also depends on temperature. This consequently leads to the observed increase of the dephasing rate and the decrease of the frequency with increasing temperature. The dephasing rate and the frequency shift represent the imaginary and real parts of the proper self-energy of the system, respectively.[176–178] That temperature dependence of the anharmonic vibrational potential manifests itself in the temperature dependence of phonon dephasing rate and frequency.[172,176,177,179] The corresponding data points extracted from the transient absorption spectroscopy measurements are described well by the Equations 2.48 and 2.49. The solid lines in Figure 5.8 b and 5.8 c are the fits according to those functions. It is worth to note the offset $\Gamma_0 = 0.12\,\mathrm{ps}^{-1}$ in Figure 5.8 b that yields the dephasing rate from alternative temperature-independent dephasing mechanisms including pure dephasing

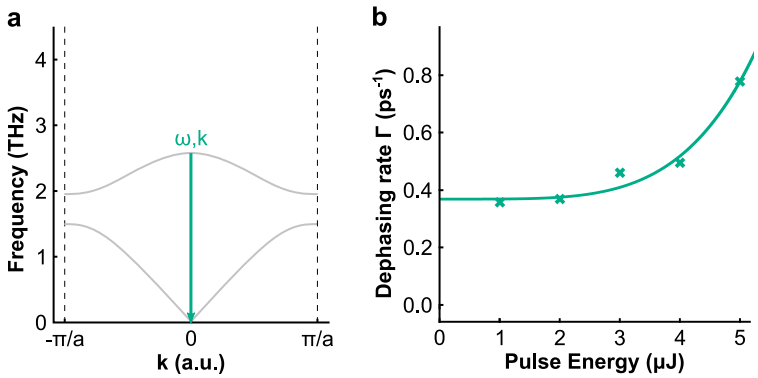

Figure 5.9: Phonon-carrier scattering in BiOI.
(a) A phonon can be annihilated through the absorption by a charge carrier. **(b)** The pump fluence-dependent dephasing rate inreases for high pump pulse energies when such processes become dominant.

with lifetime $T_2^\star$ and phonon-carrier scattering which is explained in the following section. The anharmonic decay mechanism dominates the dephasing rate at room temperature of $\Gamma = 0.36\,\mathrm{ps}^{-1}$. This value is comparable to dephasing times in other materials of a few picoseconds.[163,167,177,217,232,233]

5.3.2 Phonon-Carrier Scattering

The previous section demonstrates that besides the anharmonic decay of coherent phonons, there are further contributors to the dephasing of coherent phonons, namely phonon-carrier scattering (see Figure 5.9 a). As Figure 5.9 b shows, the dephasing rate is virtually excitation power-independent for moderate pump powers but increases for higher pump fluences.

Only at high pump fluences and thus high induced carrier and phonon densities, the dephasing rate increases as the probability for phonon-carrier scattering rises significantly. It does not contribute significantly to the total dephasing rate at low fluences.

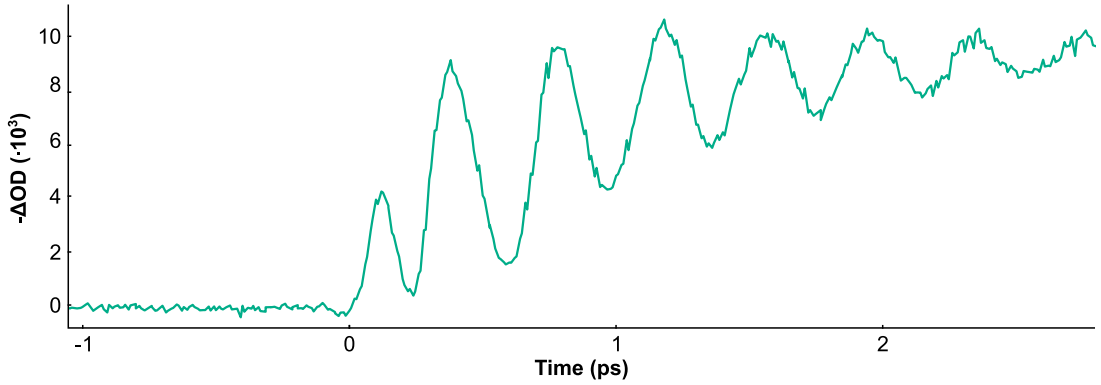

Figure 5.10: Differential optical density transient at 2.3 eV and an increased pump pulse energy. Transient at a pump pulse energy of 13 µJ. The osciallatory modulation at increased pump pulse energies increases in its amplitude relative to the absolute signal strength.

Figure 5.10 shows the transient at 2.30 eV for a strongly increased pump pulse energy of 13 µJ. In comparison to Figure 5.4 a, it is evident that the amplitude of the oscillations significantly increases relative to the total signal strength due to PSF. At these increased pump fluences it becomes apparent how strongly lattice vibrations influence the optical properties of the material. This suggests extraordinarily strong carrier-phonon coupling in BiOI.

6 | Polaronic Effects in BiOI

To this point, the previously reported results demonstrate the following: BiOI is a system of stacked 2D layers with weak, ionic inter-layer and strong, covalent intra-layer bonds. This has various far-reaching consequences: First, carriers delocalize only in-plane while the out-of-plane mobilities are low. Among multiple other effects, this limits the photocatalytic activity in thick BiOI NPs. Secondly, excitations by femtosecond laser pulses launch coherent phonons via ultrafast electric screening of the dipolar electric fields between the neighboring, oppositely charged layers.[220] These induce substantial modulations in the OD of BiOI. This shows how the expansion and contraction of the lattice parameters alters the band gap and proves that charge carriers couple strongly to the lattice.

In this context, it is critical to account for the fact that the initial charge separation and lifetimes of the coherent phonons occur on the (sub-)picosecond timescale. In contrast, photocatalysis and other potential applications reliant on charge separation involve processes taking up to seconds. Despite the understanding gained in the two previous chapters, it is crucial to know how the initially separated charges progress until they recombine or fulfill their purpose regarding the aspired application.

This chapter addresses that question using pump-probe spectroscopy with a focus on the charge carrier dynamics after the dephasing of the coherent phonons in BiOI. It is based on the findings from Reference [196].

6.1 Anisotropic Polarons and Self-Trapping

The presence of free charge carriers and their strong coupling to the lattice have critical consequences for the carrier dynamics studied via transient absorption spectroscopy on the 3 ML NPs. Their OD spectrum and the underlying contributions from the different band-to-band transitions explained in Chapter 5 are shown in Figure 6.1 a for the ease of reference. A 400 nm femtosecond laser pulse was used to excite the BiOI NPs.

At room temperature (300 K), the pump-pulse-induced change in the OD exhibits four distinct resonances at 2.30, 2.55, 2.87, and 3.35 eV in the initial spectrum (1 to 10 ps, see Figure 6.1 b). Chapter 5 explained in detail that these resonances arise from PSF by electrons at the CBM. Consequently, the absorption is reduced at the energies of direct optical transitions from valence bands to the CBM.[220] The oscillatory modulation assigned to coherent phonons

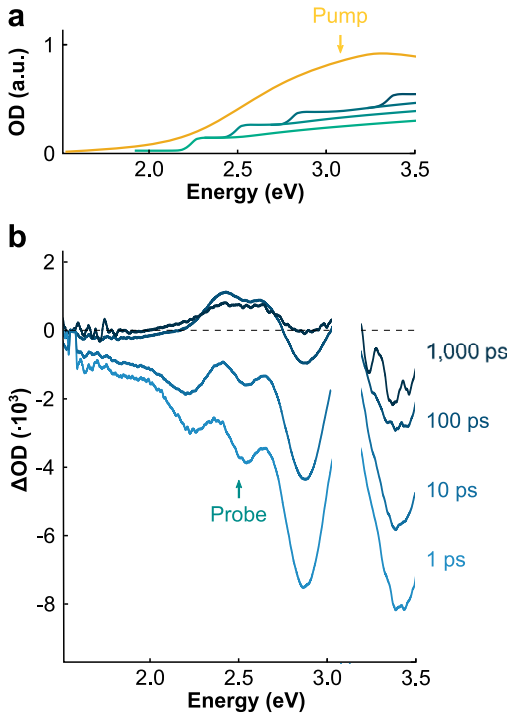

Figure 6.1: Transient absorption spectra of BiOI NPs at T = 4 K.
(a) Absorption spectrum of BiOI (orange) and the underlying contributions from multiple band-to-band transitions schematically shown in blue to green colors. The arrow indicating the pump energy refers to the spectra shown in (b) and corresponds to an excitation at 400 nm. **(b)** Transient absorption spectra: While the ΔOD at early times (1 and 10 ps) exhibit four distinct negative resonances due to PSF, at later times (100 and 1000 ps) a broad positive resonance arises.

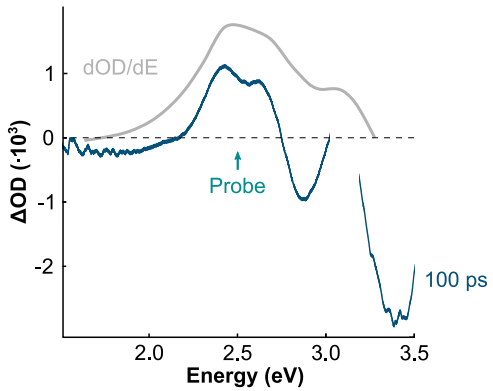

Figure 6.2: 100 ps ΔOD spectrum.
The ΔOD at later times results from the overlap of the four negative resonances with a broad positive one centered at around 2.48 eV. This positive resonance resembles the first derivative of the OD spectrum shown in gray.

determines the evolution of that spectrum in the first few picoseconds. At later times, however, an additional broad positive resonance centered at around 2.48 eV (500 nm) emerges in the ΔOD spectrum. Neither PSF nor coherent phonons in BiOI can explain that signal.

Interestingly enough, the first derivative of the OD shown in Figure 6.2 in gray matches the position and shape of that positive resonance extraordinarily well. The spectrum at $t = 100$ ps is a representative time stamp for that comparison. This indicates that the origin of the broad positive signal might lie in a reduction of the band gap and an associated red-shift of the absorption spectrum. Such shifts due to e. g. band gap renormalization or the quantum confined Stark effect often occur in pump-probe experiments.[125,228,234] In contrast to the observed slow build-up of the signal, these signals typically arise quasi-instantaneously after excitation by a short laser pulse.

While the slow emergence of the broad resonance is incompatible with these effects, it is consistent with polaronic effects in BiOI: A so-called polaron forms when a free charge carrier distorts its surrounding lattice via Coulomb interaction.[235–237] The dimensionless Fröhlich coupling constant from Equation 2.36

$$\alpha_{\mathrm{e,h}} = \frac{e^2}{8\pi\varepsilon_0\hbar\omega_{\mathrm{LO}}}\sqrt{\frac{2m_{\mathrm{e,h}}^{\mathrm{r.\,l.}}\omega_{\mathrm{LO}}}{\hbar}}\left(\frac{1}{\varepsilon_{\mathrm{b}}}-\frac{1}{\varepsilon_{\mathrm{s}}}\right) \tag{6.1}$$

with the effective mass in a rigid lattice $m^{\text{r. l.}}$ and the low and high frequency values of the dielectric function ε_{b} and ε_{s} is a measure for the strength of that interaction.[238] It depicts the Fröhlich coupling between charge carriers and LO phonons.[63] The previous chapter demonstrated that carrier-phonon coupling in BiOI is strong. It is, therefore, logical to assume that it supports the formation of polarons. Indeed, the coupling constant along the [001]-axis, the direction of the ionic bonds and the coherent vibrations, reported earlier[220] is above 5. This value is high compared to other semiconductor materials and characterizes small polarons in that direction.[69,239,240] The polaronic distortion of the lattice yields an energetically favorable state when electrostatic gains prevail over the energy cost in terms of lattice strain. In that way, the carriers dig their own potential well.[150,239,241] The relaxation of the lattice during the transfer into that polaronic state of lower energy reduces the band gap by

$$\Delta E_{\text{G}} = \alpha \hbar \omega_{\text{LO}} \tag{6.2}$$

with the LO phonon frequency ω_{LO}.[63] Consequently, the self-trapping through polaron formation results in a red-shift of the absorption spectrum which contributes to the ΔOD spectrum in pump-probe experiments. In detail, such shifts would theoretically introduce contributions in the shape of the first derivative of the OD like observed here and shown in Figure 6.2.[228] The striking agreement between that derivative and the ΔOD spectra at delay times of multiple picoseconds or more corroborates the formation of polarons and the associated red-shift in BiOI NPs.

The transient at 2.48 eV, the energy of that broad resonance, gives detailed insights into the dynamics leading to the polaron formation (see Figure 6.3 a and 6.3 b). It reveals three time regimes: (i) The signal quickly reaches its negative extremum due to PSF on the timescale of the instrument response function at $t = 0$ when the ultrashort pump pulse ($\sim$ 85 fs) excites the sample. It marks the onset of the coherent vibration modulating the ΔOD. (ii) The oscillatory modulation dephases within a few picoseconds. (iii) After full dephasing of that oscillation, a new effect comes into play: The rise of a positive signature in ΔOD associated with a time-constant of 14 ps results in the ΔOD spectrum discussed above. Similar to other reported polarons[151,242] and magnetic polarons,[243] the relaxation into the self-created energetically lower state takes its time. The formation occurs within a few to hundreds of picoseconds

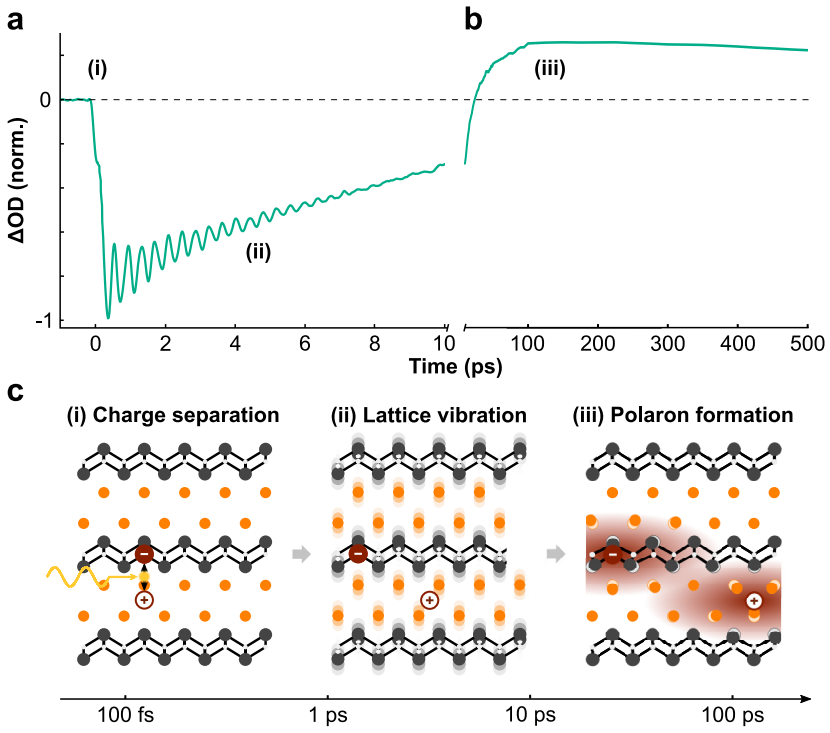

Figure 6.3: Polaron formation in BiOI NPs.
The 2.48 eV transient is shown on two time scales: **(a)** Ultrafast processes on the picosecond timescale include (i) the initial charge separation of electrons and holes in the built-in dipolar electric fields and (ii) the subsequently launched coherent phonons. **(b)** At later times, (iii) a positive signal builds up that is linked to the formation of polarons. **(c)** Schematic representation of the three fundamental subsequent mechanisms: (i) The initial charge separation, (ii) the coherent lattice vibration, and (iii) the formation of polarons and self-trapping of the charges in their respective layers.

rather than immediately with the photoexcitation. This indicates that the polarons can only form when the initial (coherent) lattice vibration has fully decayed. Intuitively, a charge can sustain a lattice distortion more easily in an equilibrated lattice with moderate vibrations. Such a long polaron formation time is consistent with theoretical predictions for materials with large Fröhlich coupling constants α.[153] Figure 6.3 c is a schematic representation of these three consecutive processes: (i) Electrons and holes separate in the built-in dipolar electric fields between neighboring oppositely charged layers. They launch coherent phonons via ultrafast electric field screening. (ii) The as-created coherent phonons persist for multiple picoseconds until they dephase and decay. (iii) Subsequently, electron- and hole-polarons form by distorting their surrounding lattice. At its core, the creation of coherent phonons and the formation of polarons result from the ionic character of the crystal in [001]-direction

and the associated strong carrier-phonon interaction in BiOI. The analogy between these two phenomena becomes apparent from the quantum mechanical description of polarons as a carrier coupling to a virtual phonon cloud.[143–145]

It is crucial to account for the anisotropic crystal structure to understand that a polaron in BiOI distorts an ellipsoidal volume: The in-plane electron (hole) coupling constant $\alpha = 1.8$ (2.9) is much smaller, and the polaron radius of 4.24 nm (2.59 nm) much larger than the respective out-of-plane values. That corresponds to a large in-plane polaron spreading over multiple unit cells. In contrast, the out-of-plane value of $\alpha > 5$ results in a small polaron in that direction typically localized in a volume smaller than or equal to that of the unit cell. These values are based on the effective in-plane masses and dielectric constants calculated by Ran *et al.*[8] Due to the localized states in [001]-direction, there are no reports of accurately calculated out-of-plane masses. This calculation approximates them to be significantly larger (at least by one order of magnitude) than the free electron mass. Consequently, optically excited charges in BiOI NPs get self-trapped in their respective layer by forming polarons, comparable to self-trapping that is known to occur in organic crystals with large coupling constants α.[150,235,241,244,245] Consistently, that explains the findings from Chapter 4: Self-trapped charges in the bulk body of thick BiOI NPs cannot reach the reactive sites at the NP surfaces and therefore do not contribute to the production of hydrogen in photocatalytic experiments.

6.2 Temperature-Dependent Polaron Formation

Additionally, the broad ΔOD resonance assigned to polaron formation exhibits a strong temperature dependence: Figure 6.4 shows the 2.48 eV transients at different temperatures between 300 K and 4 K. The positive signal gradually reduces with decreasing temperature until there is no apparent positive signal at $T = 4$ K. There are two reasons for that phenomenon: Firstly, according to Bose-Einstein statistics, fewer phonons exist at lower temperatures. Intuitively, that explains that polarons, quantum mechanically described as LO phonon-dressed carriers,[143–145] cannot form efficiently at reduced temperatures as there are fewer phonons available. Theoretically and consistently with these findings, that yields an infinite polaron formation time at $T = 0$ K when neglecting acoustic phonons.[153] From a classical point of

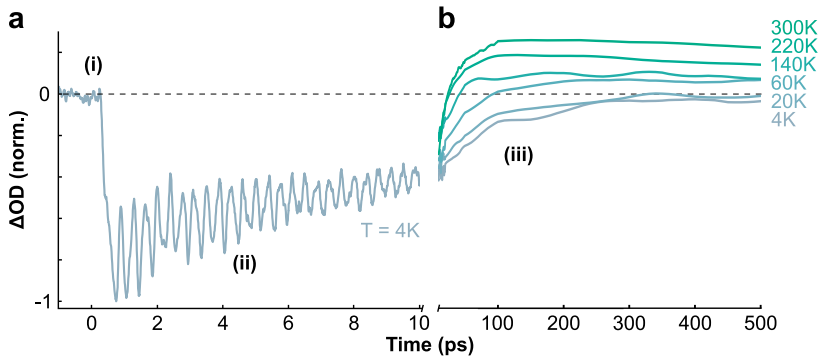

Figure 6.4: Temperature-dependent polaron formation.
(a) The initial dynamics including (i) the ultrafast charge separation launching coherent phonons that result in (ii) an oscillatory modulation of the ΔOD at $T = 4\,\mathrm{K}$. **(b)** The subsequent rise of a positive resonance linked to the formation of polarons successivly decreases with decreasing temperature.

view, the absence of optical phonons at cryogenic temperatures results in a frozen lattice. The increased energy cost of lattice distortions counteracts polaron formation.[246] Secondly, the polaron model above treats free charge carriers and their interaction with the surrounding lattice. At decreased temperatures, however, that is not valid anymore. Especially at thermal energies below the exciton binding energy, electron-hole pairs predominantly exist in the form of excitons. That temperature-dependent trend is consistent with similar materials like lead halide perovskites.[247]

7 | Conclusion

In summary, this work provides a robust understanding of the fundamental charge carrier dynamics in BiOI NPs. This chapter concludes the findings presented above and highlights the most relevant consequences. To provide a meaningful contribution, it covers the whole life-cycle of electron-hole pairs in BiOI. In detail, it explains

(i) how the crystal structure determines the optical properties of BiOI, especially the excitation of electron-hole pairs,

(ii) their ultrafast separation in the built-in electric fields launching coherent phonons,

(iii) and the formation of polarons until the final recombination or catalytic reaction.

The following puts those phenomena into context with the anisotropic crystal structure of BiOI.

Structural and Optical Properties

The time-integrated optical and catalytical properties of BiOI were studied in nanoparticles of precisely controlled size and shape. Due to its anisotropic crystal structure, BiOI preferentially forms NPs with lateral widths of hundreds of nanometers. In contrast, they are ultrathin along the [001]-axis, the direction of ionic bonds between mutually stacked positively charged bismuth-oxide $[Bi_2O_2]^{2+}$ and negatively charged double iodide $2 \times I^-$ layers. Surface ligands assisting the hydrothermal reaction could regulate crystal growth along the stacking direction and allow precise thickness-tuning of the BiOI NPs between 3 and 17 MLs.

In contrast to most typical semiconductors, BiOI NPs do not exhibit absorption blue shifts due to quantum confinement effects, even for a thickness of only 3 MLs. Localized states arise in the direction of the ionic bonds along the [001]-axis and thus, no quantization effects occur. The thickness-independent band gap is consistent with theoretical predictions.[28] Furthermore, the ionic bonds lead to a large lattice contribution to the high dielectric function, which totals to $\varepsilon \approx 45$.[8,116] In combination with small effective in-plane masses, that brings along a small exciton binding energy of less than 5 meV and explains the absence of sharp excitonic resonances in the absorption spectra of BiOI NPs. Eventually, free charge carriers exist at room temperature. These are immobile out-of-plane due to localization but are delocalized in-plane.

Ultimately, optically excited electron-hole pairs in BiOI can drive chemical reactions like water splitting. Despite the small thicknesses of some few MLs, carriers in thick NPs cannot reach the reactive sites at the surface. Rather, they are hindered by their localization and can only move in-plane. Therefore, the photocatalytic activity normalized to the catalyst mass significantly increases by a factor of three for a NP thickness reduction from 17 to 3 MLs. Consequetly, BiOI NPs only reveal their full potential as photocatalysts at thickness of around 3 MLs.

Coherent Phonons

The creation of coherent phonons in BiOI NPs was studied via transient absorption spectroscopy. In a first step, this method was applied to identify individual optical interband

transitions from the VB to the CBM. They are clearly distinguishable and reveal the underlying superposition of optical resonances adding up to the broad optical density spectrum of BiOI. Optical transitions in the visible range involve states at and around the CBM at the Γ-point. Relaxation of electrons to the CBM results in four ΔOD resonances between 2.30 and 3.35 eV. The energy required for direct optical transitions is much higher at the VBM, and therefore, holes do not contribute to the visible ΔOD spectrum.

After excitation by a femtosecond laser pulse, the dipolar electric field separates electrons and holes between the oppositely charged crystal layers in BiOI. The separation is ultrafast and screens the built-in electric field within less than ~ 0.2 ps. Consequently, the heavy ionic cores cannot follow that quickly but suddenly find themselves out of equilibrium. That launches a coherent oscillation around their new equilibrium position which is equivalent to the creation of coherent phonons. Importantly, these involve only vibrations in [001]-direction along the electric field lines. This is a direct consequence of the orientation of the electric fields orthogonal to the positive $[Bi_2O_2]^{2+}$ and negative $2 \times I^-$ layers in BiOI and thus the electron-hole separation in that direction. Finally, this evidence provides the necessary understanding for the application of BiOI in photocatalysis or other purposes reliant on efficient charge separation.

Eventually, the as-created coherent phonons dephase via two dominant mechanisms: First, the anharmonic decay of one optical phonon into two acoustic phonons under the conservation of energy and momentum results in a temperature-dependent dephasing rate. Secondly, phonon-carrier scattering, especially the annihilation of a phonon in that process, contributes to dephasing especially at increased charge carrier densities.

Polaronic Effects

Transient absorption spectroscopy revealed the charge carrier dynamics on the pico- to nanosecond scale. This connects the ultrafast processes, including the initial charge separation launching coherent phonons and their dephasing, with the final charge carrier recombination or their participation in photocatalytic reactions that take up to seconds.

Due to strong carrier-phonon coupling in BiOI, a photoexcited charge carrier in BiOI distorts its surrounding lattice and forms a polaron. The strength of that interaction is expressed through the Fröhlich coupling constant α, which is large ($\alpha > 5$) along the direction of the ionic bonds in BiOI. The relaxation into an energetically favorable state lowers the band gap of the material. The associated shift of the absorption spectrum manifests itself as a broad resonance in time-resolved ΔOD spectra. Its rise is associated with a time constant of 14 ps, which measures the polaron formation time.

That polaron is highly anisotropic, which is a direct consequence of the crystal structure: Strong carrier-lattice coupling along the ionic bonds results in a small polaron covering less than one unit cell in that direction while it spreads further in-plane. After the initial separation, electrons and holes self-trap in their respective layer by digging their own potential well and forming polarons. Thus, only charges created at the surface can participate in photocatalytic reactions.

References

[1] F. M. Mulder. "Implications of diurnal and seasonal variations in renewable energy generation for large scale energy storage." In: *Journal of Renewable and Sustainable Energy* 6.3 (2014), p. 033105. DOI: 10.1063/1.4874845 (cited on page 1).

[2] V. Quaschning. *Understanding Renewable Energy Systems*. 2nd ed. Routledge, 2016. DOI: 10.4324/9781315769431 (cited on page 1).

[3] H. B. Callen. "Thermodynamics and an Introduction to Thermostatistics, 2nd ed." In: *American Journal of Physics* 66.2 (1998), pp. 164–167. DOI: 10.1119/1.19071 (cited on page 1).

[4] G. Deutscher. *The Entropy Crisis*. WORLD SCIENTIFIC, 2008. DOI: 10.1142/6684 (cited on page 1).

[5] J. Shamsi, A. S. Urban, M. Imran, L. De Trizio, and L. Manna. "Metal Halide Perovskite Nanocrystals: Synthesis, Post-Synthesis Modifications, and Their Optical Properties." In: *Chemical Reviews* 119.5 (2019), pp. 3296–3348. DOI: 10.1021/acs.chemrev.8b00644 (cited on page 1).

[6] J. S. Manser, J. A. Christians, and P. V. Kamat. "Intriguing Optoelectronic Properties of Metal Halide Perovskites." In: *Chemical Reviews* 116.21 (2016), pp. 12956–13008. DOI: 10.1021/acs.chemrev.6b00136 (cited on pages 1, 21).

[7] C. Wu, Q. Zhang, G. Liu, Z. Zhang, D. Wang, B. Qu, Z. Chen, and L. Xiao. "From Pb to Bi: A Promising Family of Pb-Free Optoelectronic Materials and Devices." In: *Advanced Energy Materials* 10.13 (2020), p. 1902496. DOI: 10.1002/aenm.201902496 (cited on pages 1, 2).

[8] Z. Ran, X. Wang, Y. Li, D. Yang, X.-G. Zhao, K. Biswas, D. J. Singh, and L. Zhang. "Bismuth and antimony-based oxyhalides and chalcohalides as potential optoelectronic materials." In: *npj Computational Materials* 4.1 (2018), p. 14. DOI: 10.1038/s41524-018-0071-1 (cited on pages 1, 19, 57, 63, 86, 90).

[9] H. Min, D. Y. Lee, J. Kim, G. Kim, K. S. Lee, J. Kim, M. J. Paik, Y. K. Kim, K. S. Kim, M. G. Kim, T. J. Shin, and S. Il Seok. "Perovskite solar cells with atomically coherent interlayers on SnO_2 electrodes." In: *Nature* 598.7881 (2021), pp. 444–450. DOI: 10.1038/s41586-021-03964-8 (cited on page 1).

[10] National Renewable Energy Laboratory. *Best research-cell efficiencies*. https://www.nrel.gov/pv/cell-efficiency.html, visited on 14/02/2022 (cited on page 1).

[11] H. Suzuki, N. Komatsu, T. Ogawa, T. Murafuji, T. Ikegami, and Y. Matano. *Organobismuth chemistry*. Elsevier, 2001 (cited on page 2).

[12] R. Mohan. "Green bismuth." In: *Nature Chemistry* 2.4 (2010), pp. 336–336. DOI: 10.1038/nchem.609 (cited on page 2).

[13] S. Rieger, B. J. Bohn, M. Döblinger, A. F. Richter, Y. Tong, K. Wang, P. Müller-Buschbaum, L. Polavarapu, L. Leppert, J. K. Stolarczyk, and J. Feldmann. "Excitons and narrow bands determine the optical properties of cesium bismuth halides." In: *Phys. Rev. B* 100.20 (2019), p. 201404. DOI: 10.1103/PhysRevB.100.201404 (cited on page 2).

[14] B. Ghosh, S. Chakraborty, H. Wei, C. Guet, S. Li, S. Mhaisalkar, and N. Mathews. "Poor Photovoltaic Performance of $Cs_3Bi_2I_9$: An Insight through First-Principles Calculations." In: *The Journal of Physical Chemistry C* 121.32 (2017), pp. 17062–17067. DOI: 10.1021/acs.jpcc.7b03501 (cited on pages 2, 7).

[15] J. K. Stolarczyk, S. Bhattacharyya, L. Polavarapu, and J. Feldmann. "Challenges and Prospects in Solar Water Splitting and CO2 Reduction with Inorganic and Hybrid Nanostructures." In: *ACS Catalysis* 8.4 (2018), pp. 3602–3635. DOI: 10.1021/acscatal.8b00791 (cited on pages 2, 7, 67).

[16] X. Chen, S. Shen, L. Guo, and S. S. Mao. "Semiconductor-based Photocatalytic Hydrogen Generation." In: *Chemical Reviews* 110.11 (2010). PMID: 21062099, pp. 6503–6570. DOI: 10.1021/cr1001645 (cited on pages 2, 7, 19).

[17] Q. Wang and K. Domen. "Particulate Photocatalysts for Light-Driven Water Splitting: Mechanisms, Challenges, and Design Strategies." In: *Chemical Reviews* 120.2 (2020), pp. 919–985. DOI: 10.1021/acs.chemrev.9b00201 (cited on page 6).

[18] H. Huang, X. Li, X. Han, N. Tian, Y. Zhang, and T. Zhang. "Moderate band-gap-broadening induced high separation of electron–hole pairs in Br substituted BiOI: a combined experimental and theoretical investigation." In: *Physical Chemistry Chemical Physics* 17.5 (2015), pp. 3673–3679. DOI: 10.1039/C4CP04842C (cited on pages 6, 67).

[19] H. Feng, Z. Xu, L. Wang, Y. Yu, D. Mitchell, D. Cui, X. Xu, J. Shi, T. Sannomiya, Y. Du, W. Hao, and S. X. Dou. "Modulation of Photocatalytic Properties by Strain in 2D BiOBr Nanosheets." In: *ACS Applied Materials & Interfaces* 7.50 (2015), pp. 27592–27596. DOI: 10.1021/acsami.5b08904 (cited on pages 6, 57).

[20] M. Guan, C. Xiao, J. Zhang, S. Fan, R. An, Q. Cheng, J. Xie, M. Zhou, B. Ye, and Y. Xie. "Vacancy associates promoting solar-driven photocatalytic activity of ultrathin bismuth oxychloride nanosheets." In: *Journal of the American Chemical Society* 135.28 (2013), pp. 10411–10417. DOI: 10.1021/ja402956f (cited on pages 6, 9, 42, 58).

[21] Y. Huang, H. Li, M.-S. Balogun, W. Liu, Y. Tong, X. Lu, and H. Ji. "Oxygen Vacancy Induced Bismuth Oxyiodide with Remarkably Increased Visible-Light Absorption and Superior Photocatalytic Performance." In: *ACS Applied Materials & Interfaces* 6.24 (2014), pp. 22920–22927. DOI: 10.1021/am507641k (cited on page 6).

[22] X. Hu, J. Hu, Q. Peng, X. Ma, S. Dong, and H. Wang. "Construction of 2D all-solid-state Z-scheme g-C_3N_4/BiOI/RGO hybrid structure immobilized on Ni foam for CO_2 reduction and pollutant degradation." In: *Materials Research Bulletin* 122 (2020), p. 110682. DOI: 10.1016/j.materresbull.2019.110682 (cited on page 6).

[23] F. Duan, X. Wang, T. Tan, and M. Chen. "Highly exposed surface area of 001 facets dominated BiOBr nanosheets with enhanced visible light photocatalytic activity." In: *Physical Chemistry Chemical Physics* 18.8 (2016), pp. 6113–6121. DOI: 10.1039/C5CP06711A (cited on pages 6, 57).

[24] W. Fan, H. Li, F. Zhao, X. Xiao, Y. Huang, H. Ji, and Y. Tong. "Boosting the photocatalytic performance of (001) BiOI: enhancing donor density and separation efficiency of photogenerated electrons and holes." In: *Chem. Commun.* 52.30 (2016), pp. 5316–5319. DOI: 10.1039/C6CC00903D (cited on pages 6, 57).

[25] N. Kijima, K. Matano, M. Saito, T. Oikawa, T. Konishi, H. Yasuda, T. Sato, and Y. Yoshimura. "Oxidative catalytic cracking of n-butane to lower alkenes over layered BiOCl catalyst." In: *Applied Catalysis A: General* 206.2 (2001), pp. 237–244. DOI: 10.1016/S0926-860X(00)00598-6 (cited on pages 6, 57).

[26] H. Zhang, L. Liu, and Z. Zhou. "Towards better photocatalysts: first-principles studies of the alloying effects on the photocatalytic activities of bismuth oxyhalides under visible light." In: *Physical Chemistry Chemical Physics* 14.3 (2012), pp. 1286–1292. DOI: 10.1039/C1CP23516H (cited on pages 6, 57).

[27] Q. Li, X. Zhao, J. Yang, C.-J. Jia, Z. Jin, and W. Fan. "Exploring the effects of nanocrystal facet orientations in g-C_3N_4/BiOCl heterostructures on photocatalytic performance." In: *Nanoscale* 7.45 (2015), pp. 18971–18983. DOI: 10.1039/C5NR05154A (cited on pages 6, 57).

[28] J. Wang, M. Zhang, J. Meng, Q. Li, and J. Yang. "Single-and few-layer BiOI as promising photocatalysts for solar water splitting." In: *RSC Advances* 7.39 (2017), pp. 24446–24452. DOI: 10.1039/C7RA01723E (cited on pages 6, 17, 18, 57, 62, 68, 90).

[29] Y. Wang, K. Deng, and L. Zhang. "Visible Light Photocatalysis of BiOI and Its Photocatalytic Activity Enhancement by in Situ Ionic Liquid Modification." In: *The Journal of Physical Chemistry C* 115.29 (2011), pp. 14300–14308. DOI: 10.1021/jp2042069 (cited on pages 6, 57).

[30] H. Cheng, B. Huang, and Y. Dai. "Engineering BiOX (X = Cl, Br, I) nanostructures for highly efficient photocatalytic applications." In: *Nanoscale* 6.4 (2014), pp. 2009–2026. DOI: 10.1039/C3NR05529A (cited on pages 6, 57, 67).

[31] H. Li, Z. Yang, J. Zhang, Y. Huang, H. Ji, and Y. Tong. "Indium doped BiOI nanosheets: Preparation, characterization and photocatalytic degradation activity." In: *Applied Surface Science* 423 (2017), pp. 1188–1197. DOI: 10.1016/j.apsusc.2017.06.301 (cited on page 6).

[32] T. S. Jamil, E. S. Mansor, and M. Azab El-Liethy. "Photocatalytic inactivation of E. coli using nano-size bismuth oxyiodide photocatalysts under visible light." In: *Journal of Environmental Chemical Engineering* 3.4, Part A (2015), pp. 2463–2471. DOI: 10.1016/j.jece.2015.09.017 (cited on page 6).

[33] Y. Xu, Z. Shi, L. Zhang, E. M. B. Brown, and A. Wu. "Layered bismuth oxyhalide nanomaterials for highly efficient tumor photodynamic therapy." In: *Nanoscale* 8.25 (2016), pp. 12715–12722. DOI: 10.1039/C5NR04540A (cited on pages 7, 67).

[34] M. R. Younis, G. He, J. Qu, J. Lin, P. Huang, and X.-H. Xia. "Inorganic Nanomaterials with Intrinsic Singlet Oxygen Generation for Photodynamic Therapy." In: *Advanced Science* 8.21 (2021), p. 2102587. DOI: 10.1002/advs.202102587 (cited on pages 7, 67).

[35] G.-J. Lee, Y.-C. Zheng, and J. J. Wu. "Fabrication of hierarchical bismuth oxyhalides (BiOX, X=Cl, Br, I) materials and application of photocatalytic hydrogen production from water splitting." In: *Catalysis Today* 307 (2018), pp. 197–204. DOI: 10.1016/j.cattod.2017.04.044 (cited on page 7).

[36] V. Pecunia, L. G. Occhipinti, and R. L. Z. Hoye. "Emerging Indoor Photovoltaic Technologies for Sustainable Internet of Things." In: *Advanced Energy Materials* 11.29 (2021), p. 2100698. DOI: 10.1002/aenm.202100698 (cited on pages 7, 20).

[37] Y.-W. Tai, J.-S. Chen, C.-C. Yang, and B.-Z. Wan. "Preparation of nano-gold on $K_2La_2Ti_3O_{10}$ for producing hydrogen from photo-catalytic water splitting." In: *Catalysis Today* 97.2 (2004). Catalysis for New Energy Resources and Environmental Protection, pp. 95–101. DOI: 10.1016/j.cattod.2004.04.054 (cited on page 8).

[38] C. M. Wolff, P. D. Frischmann, M. Schulze, B. J. Bohn, R. Wein, P. Livadas, M. T. Carlson, F. Jäckel, J. Feldmann, F. Würthner, et al. "All-in-one visible-light-driven water splitting by combining nanoparticulate and molecular co-catalysts on CdS nanorods." In: *Nature Energy* 3.10 (2018), pp. 862–869. DOI: 10.1038/s41560-018-0229-6 (cited on page 8).

[39] T. Simon, N. Bouchonville, M. J. Berr, A. Vaneski, A. Adrović, D. Volbers, R. Wyrwich, M. Döblinger, A. S. Susha, A. L. Rogach, et al. "Redox shuttle mechanism enhances photocatalytic H_2 generation on Ni-decorated CdS nanorods." In: *Nature materials* 13.11 (2014), pp. 1013–1018. DOI: 10.1038/nmat4049 (cited on page 8).

[40] A. Manzi, T. Simon, C. Sonnleitner, M. Döblinger, R. Wyrwich, O. Stern, J. K. Stolarczyk, and J. Feldmann. "Light-Induced Cation Exchange for Copper Sulfide Based CO_2 Reduction." In: *Journal of the American Chemical Society* 137.44 (2015). PMID: 26479775, pp. 14007–14010. DOI: 10.1021/jacs.5b06778 (cited on page 8).

[41] T. Takata, K. Shinohara, A. Tanaka, M. Hara, J. Kondo, and K. Domen. "A highly active photocatalyst for overall water splitting with a hydrated layered perovskite structure." In: *Journal of Photochemistry and Photobiology A: Chemistry* 106.1 (1997), pp. 45–49. DOI: 10.1016/S1010-6030(97)00037-3 (cited on page 8).

[42] S.-C. Moon, H. Mametsuka, S. Tabata, and E. Suzuki. "Photocatalytic production of hydrogen from water using TiO_2 and B/TiO_2." In: *Catalysis Today* 58.2 (2000), pp. 125–132. DOI: 10.1016/S0920-5861(00)00247-9 (cited on page 8).

[43] S.-C. Moon, H. Mametsuka, E. Suzuki, and M. Anpo. "Stoichiometric Decomposition of Pure Water over Pt-Loaded Ti/B Binary Oxide under UV-Irradiation." In: *Chemistry Letters* 27.2 (1998), pp. 117–118. DOI: 10.1246/cl.1998.117 (cited on page 8).

[44] T. Simon, M. T. Carlson, J. K. Stolarczyk, and J. Feldmann. "Electron Transfer Rate vs Recombination Losses in Photocatalytic H_2 Generation on Pt-Decorated CdS Nanorods." In: *ACS Energy Letters* 1.6 (2016), pp. 1137–1142. DOI: 10.1021/acsenergylett.6b00468 (cited on page 8).

[45] K. Wenderich and G. Mul. "Methods, Mechanism, and Applications of Photodeposition in Photocatalysis: A Review." In: *Chemical Reviews* 116.23 (2016). PMID: 27960266, pp. 14587–14619. DOI: 10.1021/acs.chemrev.6b00327 (cited on page 8).

[46] A. Bravais. *Les systemes formes par des pointes distribues regulierement sur un plan ou dans l'espace*. Vol. 19. J. Ecole. Polytech., 1850, pp. 1–128 (cited on page 8).

[47] C. Kittel. *Introduction to solid state physics*. Vol. 9. New York: Wiley, 1996 (cited on pages 8, 9, 13).

[48] N. W. Ashcroft and N. D. Mermin. *Solid State Physics*. Vol. 9. New York: Saunders College Publishing, 1976. DOI: 10.1002/piuz.19780090109 (cited on pages 8, 9, 14, 15).

[49] L. Zhao, X. Zhang, C. Fan, Z. Liang, and P. Han. "First-principles study on the structural, electronic and optical properties of BiOX (X = Cl, Br, I) crystals." In: *Physica B: Condensed Matter* 407.17 (2012), pp. 3364–3370. DOI: 10.1016/j.physb.2012.04.039 (cited on pages 8, 67).

[50] Z.-Y. Zhao and W.-W. Dai. "Structural, Electronic, and Optical Properties of Eu-Doped BiOX (X = F, Cl, Br, I): A DFT+U Study." In: *Inorganic Chemistry* 53.24 (2014), pp. 13001–13011. DOI: 10.1021/ic5021059 (cited on pages 8, 9).

[51] M. D. Prasad, M. G. Krishna, and S. K. Batabyal. "Structurally Engineered Two-Dimensional Layered Bismuth Oxyiodide Surfaces as a "Dip Photocatalyst" for a Photocatalytic Reaction." In: *Crystal Growth & Design* 20.8 (2020), pp. 4909–4918. DOI: 10.1021/acs.cgd.9b01141 (cited on pages 8, 67).

[52] L. Ye, Y. Su, X. Jin, H. Xie, and C. Zhang. "Recent advances in BiOX (X = Cl, Br and I) photocatalysts: synthesis, modification, facet effects and mechanisms." In: *Environmental Science: Nano* 1.2 (2014), pp. 90–112. DOI: 10.1039/C3EN00098B (cited on pages 8, 67).

[53] L. Protesescu, S. Yakunin, M. I. Bodnarchuk, F. Krieg, R. Caputo, C. H. Hendon, R. X. Yang, A. Walsh, and M. V. Kovalenko. "Nanocrystals of cesium lead halide perovskites ($CsPbX_3$, X= Cl, Br, and I): novel optoelectronic materials showing bright emission with wide color gamut." In: *Nano letters* 15.6 (2015), pp. 3692–3696. DOI: 10.1021/nl5048779 (cited on page 8).

[54] W. L. Huang and Q. Zhu. "Electronic structures of relaxed BiOX (X=F, Cl, Br, I) photocatalysts." In: *Computational Materials Science* 43.4 (2008), pp. 1101–1108. DOI: 10.1016/j.commatsci.2008.03.005 (cited on pages 8, 9, 18, 57, 67).

[55] D. S. Bhachu, S. J. Moniz, S. Sathasivam, D. O. Scanlon, A. Walsh, S. M. Bawaked, M. Mokhtar, A. Y. Obaid, I. P. Parkin, and J. Tang. "Bismuth oxyhalides: synthesis, structure and photoelectrochemical activity." In: *Chemical science* 7.8 (2016), pp. 4832–4841. DOI: 10.1039/C6SC00389C (cited on page 9).

[56] A. M. Ganose, M. Cuff, K. T. Butler, A. Walsh, and D. O. Scanlon. "Interplay of Orbital and Relativistic Effects in Bismuth Oxyhalides: BiOF, BiOCl, BiOBr, and BiOI." In: *Chemistry of Materials* 28.7 (2016), pp. 1980–1984. DOI: 10.1021/acs.chemmater.6b00349 (cited on pages 9, 18).

[57] J. Xiong, G. Cheng, G. Li, F. Qin, and R. Chen. "Well-crystallized square-like 2D BiOCl nanoplates: mannitol-assisted hydrothermal synthesis and improved visible-light-driven photocatalytic performance." In: *RSC Advances* 1.8 (2011), pp. 1542–1553. DOI: 10.1039/C1RA00335F (cited on pages 9, 42).

[58] Y. Lei, G. Wang, S. Song, W. Fan, and H. Zhang. "Synthesis, characterization and assembly of BiOCl nanostructure and their photocatalytic properties." In: *CrystEngComm* 11.9 (2009), pp. 1857–1862. DOI: 10.1039/B909013B (cited on page 9).

[59] N. T. Hahn, S. Hoang, J. L. Self, and C. B. Mullins. "Spray Pyrolysis Deposition and Photoelectrochemical Properties of n-Type BiOI Nanoplatelet Thin Films." In: *ACS Nano* 6.9 (2012), pp. 7712–7722. DOI: 10.1021/nn3031063 (cited on page 9).

[60] J. Han, G. Zhu, M. Hojamberdiev, J. Peng, and P. Liu. "Temperature effect on phase transition and morphological transformation of BiOI microspheres to Bi_5O_7I microstructures." In: *Materials Letters* 169 (2016), pp. 122–125. DOI: 10.1016/j.matlet.2016.01.100 (cited on page 9).

[61] A. C. Mera, Y. Moreno, J.-Y. Pivan, O. Peña, and H. D. Mansilla. "Solvothermal synthesis of BiOI microspheres: Effect of the reaction time on the morphology and photocatalytic activity." In: *Journal of Photochemistry and Photobiology A: Chemistry* 289 (2014), pp. 7–13. DOI: 10.1016/j.jphotochem.2014.05.015 (cited on page 9).

[62] H. Peng, C. K. Chan, S. Meister, X. F. Zhang, and Y. Cui. "Shape Evolution of Layer-Structured Bismuth Oxychloride Nanostructures via Low-Temperature Chemical Vapor Transport." In: *Chemistry of Materials* 21.2 (2009), pp. 247–252. DOI: 10.1021/cm802041g (cited on page 9).

[63] K. W. Böer and U. W. Pohl. *Semiconductor Physics*. Vol. 1. Berlin: Springer, 2018. DOI: 10.1007/978-3-319-69150-3 (cited on pages 10, 16, 84).

[64] J. E. Jones and S. Chapman. "On the determination of molecular fields. - I. From the variation of the viscosity of a gas with temperature." In: *Proceedings of the Royal Society of London. Series A, Containing Papers of a Mathematical and Physical Character* 106.738 (1924), pp. 441–462. DOI: 10.1098/rspa.1924.0081 (cited on page 10).

[65] J. E. Jones and S. Chapman. "On the determination of molecular fields. - II. From the equation of state of a gas." In: *Proceedings of the Royal Society of London. Series A, Containing Papers of a Mathematical and Physical Character* 106.738 (1924), pp. 463–477. DOI: 10.1098/rspa.1924.0082 (cited on page 10).

[66] J. E. Lennard-Jones. "Cohesion." In: *Proceedings of the Physical Society* 43.5 (1931), pp. 461–482. DOI: 10.1088/0959-5309/43/5/301 (cited on page 10).

[67] G. Mie. "Zur kinetischen Theorie der einatomigen Körper." In: *Annalen der Physik* 316.8 (1903), pp. 657–697. DOI: 10.1002/andp.19033160802 (cited on page 10).

[68] R. Hooke. *Lectures de potentia restitutiva, or of spring explaining the power of springing bodies*. John Martyn, 1678 (cited on page 10).

[69] C. F. Klingshirn. *Semiconductor optics*. Berlin and Heidelberg: Springer, 2012. DOI: 10.1007/978-3-540-38347-5 (cited on pages 11, 13, 15–17, 23, 27, 33, 34, 84).

[70] Bose. "Plancks Gesetz und Lichtquantenhypothese." In: *Zeitschrift für Physik* 26.1 (1924), pp. 178–181. DOI: 10.1007/BF01327326 (cited on page 11).

[71] M. Dresselhaus, G. Dresselhaus, S. B. Cronin, and A. G. Souza Filho. *Solid State Properties: From Bulk to Nano*. Berlin: Springer, 2018. DOI: 10.1007/978-3-662-55922-2 (cited on pages 12, 28).

[72] K. Kopitzki and P. Herzog. *Einführung in die Festkörperphysik*. Vol. 4. Stuttgart: Springer, 1989. DOI: 10.1007/978-3-322-91792-8 (cited on pages 12, 43).

[73] M. Hase, M. Kitajima, S.-i. Nakashima, and K. Mizoguchi. "Dynamics of Coherent Anharmonic Phonons in Bismuth Using High Density Photoexcitation." In: *Phys. Rev. Lett.* 88.6 (2002), p. 067401. DOI: 10.1103/PhysRevLett.88.067401 (cited on page 12).

[74] S. Dutta, T. Das, and S. Datta. "Impact of bi-axial strain on the structural, electronic and optical properties of photo-catalytic bulk bismuth oxyhalides." In: *Physical Chemistry Chemical Physics* 20.1 (2018), pp. 103–111. DOI: 10.1039/C7CP07366F (cited on page 12).

[75] L. Talirz, S. Kumbhar, E. Passaro, A. V. Yakutovich, V. Granata, F. Gargiulo, M. Borelli, M. Uhrin, S. P. Huber, S. Zoupanos, C. S. Adorf, C. W. Andersen, O. Schütt, C. A. Pignedoli, D. Passerone, J. VandeVondele, T. C. Schulthess, B. Smit, G. Pizzi, and N. Marzari. "Materials Cloud, a platform for open computational science." In: *Scientific Data* 7.1 (2020), p. 299. DOI: 10.1038/s41597-020-00637-5 (cited on pages 12, 72, 73).

[76] A. Sommerfeld. "Zur Elektronentheorie der Metalle auf Grund der Fermischen Statistik." In: *Zeitschrift für Physik* 47.1 (1928), pp. 1–32. DOI: 10.1007/BF01391052 (cited on page 14).

[77] P. Y. Yu and M. Cardona. *Fundamentals of Semiconductors, Graduate Texts in Physics*. Vol. 4. Berlin Heidelberg: Springer, 2010. DOI: 10.1007/978-3-642-00710-1_2 (cited on page 14).

[78] F. Bloch. "Über die Quantenmechanik der Elektronen in Kristallgittern." In: *Zeitschrift für Physik* 52.7 (1929), pp. 555–600. DOI: 10.1007/BF01339455 (cited on page 14).

[79] T. Edvinsson. "Optical quantum confinement and photocatalytic properties in two-, one- and zero-dimensional nanostructures." In: *Royal Society Open Science* 5.9 (2018), p. 180387. DOI: 10.1098/rsos.180387 (cited on pages 16, 23).

[80] E. Fermi. "Eine statistische Methode zur Bestimmung einiger Eigenschaften des Atoms und ihre Anwendung auf die Theorie des periodischen Systems der Elemente." In: *Zeitschrift für Physik* 48.1 (1928), pp. 73–79. DOI: 10.1007/BF01351576 (cited on pages 17, 24).

[81] P. A. M. Dirac and R. H. Fowler. "On the theory of quantum mechanics." In: *Proceedings of the Royal Society of London. Series A, Containing Papers of a Mathematical and Physical Character* 112.762 (1926), pp. 661–677. DOI: 10.1098/rspa.1926.0133 (cited on pages 17, 24).

[82] W.-W. Dai and Z.-Y. Zhao. "Electronic structure and optical properties of BiOI as a photocatalyst driven by visible light." In: *J Catalysts* 6.9 (2016), p. 133. DOI: 10.3390/catal6090133 (cited on pages 17, 19, 57, 62).

[83] K.-L. Zhang, C.-M. Liu, F.-Q. Huang, C. Zheng, and W.-D. Wang. "Study of the electronic structure and photocatalytic activity of the BiOCl photocatalyst." In: *Applied Catalysis B: Environmental* 68.3 (2006), pp. 125–129. DOI: 10.1016/j.apcatb.2006.08.002 (cited on pages 18, 67).

[84] X. Zhang, Z. Ai, F. Jia, and L. Zhang. "Generalized One-Pot Synthesis, Characterization, and Photocatalytic Activity of Hierarchical BiOX (X = Cl, Br, I) Nanoplate Microspheres." In: *The Journal of Physical Chemistry C* 112.3 (2008), pp. 747–753. DOI: 10.1021/jp077471t (cited on page 18).

[85] H. An, Y. Du, T. Wang, C. Wang, W. Hao, and J. Zhang. "Photocatalytic properties of BiOX (X = Cl, Br, and I)." In: *Rare Metals* 27.3 (2008), pp. 243–250. DOI: 10.1016/S1001-0521(08)60123-0 (cited on page 18).

[86] W. Wang, F. Huang, and X. Lin. "xBiOI–(1–x)BiOCl as efficient visible-light-driven photocatalysts." In: *Scripta Materialia* 56.8 (2007), pp. 669–672. DOI: 10.1016/j.scriptamat.2006.12.023 (cited on page 18).

[87] W. Wang, F. Huang, X. Lin, and J. Yang. "Visible-light-responsive photocatalysts xBiOBr–(1–x)BiOI." In: *Catalysis Communications* 9.1 (2008), pp. 8–12. DOI: 10.1016/j.catcom.2007.05.014 (cited on page 18).

[88] L. Chen, S.-F. Yin, R. Huang, Y. Zhou, S.-L. Luo, and C.-T. Au. "Facile synthesis of BiOCl nano-flowers of narrow band gap and their visible-light-induced photocatalytic property." In: *Catalysis Communications* 23 (2012), pp. 54–57. DOI: 10.1016/j.catcom.2012.03.001 (cited on page 18).

[89] W. Su, J. Wang, Y. Huang, W. Wang, L. Wu, X. Wang, and P. Liu. "Synthesis and catalytic performances of a novel photocatalyst BiOF." In: *Scripta Materialia* 62.6 (2010), pp. 345–348. DOI: 10.1016/j.scriptamat.2009.10.039 (cited on page 18).

[90] H. Deng, J. Wang, Q. Peng, X. Wang, and Y. Li. "Controlled Hydrothermal Synthesis of Bismuth Oxyhalide Nanobelts and Nanotubes." In: *Chemistry – A European Journal* 11.22 (2005), pp. 6519–6524. DOI: 10.1002/chem.200500540 (cited on page 18).

[91] T. Leijtens, G. E. Eperon, N. K. Noel, S. N. Habisreutinger, A. Petrozza, and H. J. Snaith. "Stability of Metal Halide Perovskite Solar Cells." In: *Advanced Energy Materials* 5.20 (2015), p. 1500963. DOI: 10.1002/aenm.201500963 (cited on page 18).

[92] X. Li, T. Kako, and J. Ye. "2-Propanol photodegradation over lead niobates under visible light irradiation." In: *Applied Catalysis A: General* 326.1 (2007), pp. 1–7. DOI: 10.1016/j.apcata.2007.02.023 (cited on page 19).

[93] X. Li and J. Ye. "Photocatalytic Degradation of Rhodamine B over $Pb_3Nb_4O_{13}$/Fumed SiO_2 Composite under Visible Light Irradiation." In: *The Journal of Physical Chemistry C* 111.35 (2007), pp. 13109–13116. DOI: 10.1021/jp072752m (cited on page 19).

[94] H. G. Kim, O. S. Becker, J. S. Jang, S. M. Ji, P. H. Borse, and J. S. Lee. "A generic method of visible light sensitization for perovskite-related layered oxides: Substitution effect of lead." In: *Journal of Solid State Chemistry* 179.4 (2006), pp. 1214–1218. DOI: 10.1016/j.jssc.2006.01.024 (cited on page 19).

[95] A. Walsh, G. W. Watson, D. J. Payne, R. G. Edgell, J. Guo, P.-A. Glans, T. Learmonth, and K. E. Smith. "Electronic structure of the α and δ phases of Bi_2O_3: A combined ab initio and x-ray spectroscopy study." In: *Phys. Rev. B* 73.23 (2006), p. 235104. DOI: 10.1103/PhysRevB.73.235104 (cited on page 19).

[96] A. Walsh and G. W. Watson. "Polymorphism in Bismuth Stannate: A First-Principles Study." In: *Chemistry of Materials* 19.21 (2007), pp. 5158–5164. DOI: 10.1021/cm0714279 (cited on page 19).

[97] A. Walsh, Y. Yan, M. N. Huda, M. M. Al-Jassim, and S.-H. Wei. "Band Edge Electronic Structure of $BiVO_4$: Elucidating the Role of the Bi s and V d Orbitals." In: *Chemistry of Materials* 21.3 (2009), pp. 547–551. DOI: 10.1021/cm802894z (cited on page 19).

[98] A. Walsh, D. J. Payne, R. G. Egdell, and G. W. Watson. "Stereochemistry of post-transition metal oxides: revision of the classical lone pair model." In: *Chem. Soc. Rev.* 40 (9 2011), pp. 4455–4463. DOI: 10.1039/C1CS15098G (cited on page 19).

[99] T. Kako, Z. Zou, M. Katagiri, and J. Ye. "Decomposition of Organic Compounds over $NaBiO_3$ under Visible Light Irradiation." In: *Chemistry of Materials* 19.2 (2007), pp. 198–202. DOI: 10.1021/cm0611284 (cited on page 19).

[100] J. Tang, Z. Zou, and J. Ye. "Efficient photocatalytic decomposition of organic contaminants over $CaBi_2O_4$ under visible-light irradiation." In: *Angewandte Chemie* 116.34 (2004), pp. 4563–4566. DOI: 10.1002/ange.200353594 (cited on page 19).

[101] R. Solarska, A. Heel, J. Ropka, A. Braun, L. Holzer, J. Ye, and T. Graule. "Nanoscale calcium bismuth mixed oxide with enhanced photocatalytic performance under visible light." In: *Applied Catalysis A: General* 382.2 (2010), pp. 190–196. DOI: 10.1016/j.apcata.2010.04.043 (cited on page 19).

[102] C. Zhang and Y. Zhu. "Synthesis of Square Bi_2WO_6 Nanoplates as High-Activity Visible-Light-Driven Photocatalysts." In: *Chemistry of Materials* 17.13 (2005), pp. 3537–3545. DOI: 10.1021/cm0501517 (cited on page 19).

[103] H. Fu, L. Zhang, W. Yao, and Y. Zhu. "Photocatalytic properties of nanosized Bi_2WO_6 catalysts synthesized via a hydrothermal process." In: *Applied Catalysis B: Environmental* 66.1 (2006), pp. 100–110. DOI: 10.1016/j.apcatb.2006.02.022 (cited on page 19).

[104] Y. Shimodaira, H. Kato, H. Kobayashi, and A. Kudo. "Photophysical Properties and Photocatalytic Activities of Bismuth Molybdates under Visible Light Irradiation." In: *The Journal of Physical Chemistry B* 110.36 (2006). PMID: 16956264, pp. 17790–17797. DOI: 10.1021/jp0622482 (cited on page 19).

[105] X. P. Lin, F. Q. Huang, W. D. Wang, and K. L. Zhang. "A novel photocatalyst $BiSbO_4$ for degradation of methylene blue." In: *Applied Catalysis A: General* 307.2 (2006), pp. 257–262. DOI: 10.1016/j.apcata.2006.03.057 (cited on page 19).

[106] D. J. Payne, R. G. Egdell, A. Walsh, G. W. Watson, J. Guo, P.-A. Glans, T. Learmonth, and K. E. Smith. "Electronic Origins of Structural Distortions in Post-Transition Metal Oxides: Experimental and Theoretical Evidence for a Revision of the Lone Pair Model." In: *Phys. Rev. Lett.* 96.15 (2006), p. 157403. DOI: 10.1103/PhysRevLett.96.157403 (cited on page 19).

[107] R. E. Brandt, V. Stevanović, D. S. Ginley, and T. Buonassisi. "Identifying defect-tolerant semiconductors with high minority-carrier lifetimes: beyond hybrid lead halide perovskites." In: *MRS Communications* 5.2 (2015), pp. 265–275. DOI: 10.1557/mrc.2015.26 (cited on pages 19–21).

[108] B. A. Connor, L. Leppert, M. D. Smith, J. B. Neaton, and H. I. Karunadasa. "Layered Halide Double Perovskites: Dimensional Reduction of $Cs_2AgBiBr_6$." In: *Journal of the American Chemical Society* 140.15 (2018). PMID: 29575889, pp. 5235–5240. DOI: 10.1021/jacs.8b01543 (cited on page 19).

[109] E. Wlaźlak, A. Blachecki, M. Bisztyga-Szklarz, S. Klejna, T. Mazur, K. Mech, K. Pilarczyk, D. Przyczyna, M. Suchecki, P. Zawal, and K. Szaciłowski. "Heavy pnictogen chalcohalides: the synthesis, structure and properties of these rediscovered semiconductors." In: *Chemical Communications* 54.86 (2018), pp. 12133–12162. DOI: 10.1039/c8cc05149f (cited on page 19).

[110] R. E. Brandt, J. R. Poindexter, P. Gorai, R. C. Kurchin, R. L. Z. Hoye, L. Nienhaus, M. W. B. Wilson, J. A. Polizzotti, R. Sereika, R. Žaltauskas, L. C. Lee, J. L. MacManus-Driscoll, M. Bawendi, V. Stevanović, and T. Buonassisi. "Searching for "Defect-Tolerant" Photovoltaic Materials: Combined Theoretical and Experimental Screening." In: *Chemistry of Materials* 29.11 (2017), pp. 4667–4674. DOI: 10.1021/acs.chemmater.6b05496 (cited on pages 19–21).

[111] P. Umari, E. Mosconi, and F. De Angelis. "Relativistic GW calculations on $CH_3NH_3PbI_3$ and $CH_3NH_3SnI_3$ Perovskites for Solar Cell Applications." In: *Scientific Reports* 4.1 (2014), p. 4467. DOI: 10.1038/srep04467 (cited on page 20).

[112] M. Pazoki, M. B. Johansson, H. Zhu, P. Broqvist, T. Edvinsson, G. Boschloo, and E. M. J. Johansson. "Bismuth Iodide Perovskite Materials for Solar Cell Applications: Electronic Structure, Optical Transitions, and Directional Charge Transport." In: *The Journal of Physical Chemistry C* 120.51 (2016), pp. 29039–29046. DOI: 10.1021/acs.jpcc.6b11745 (cited on page 20).

[113] H. J. Queisser. "Recombination at deep traps." In: *Solid-State Electronics* 21.11 (1978), pp. 1495–1503. DOI: 10.1016/0038-1101(78)90231-9 (cited on page 21).

[114] L. M. Herz. "Charge-Carrier Dynamics in Organic-Inorganic Metal Halide Perovskites." In: *Annual Review of Physical Chemistry* 67.1 (2016), pp. 65–89. DOI: 10.1146/annurev-physchem-040215-112222 (cited on pages 21, 26).

[115] T. N. Huq, L. C. Lee, L. Eyre, W. Li, R. A. Jagt, C. Kim, S. Fearn, V. Pecunia, F. Deschler, J. L. MacManus-Driscoll, and R. L. Z. Hoye. "Electronic Structure and Optoelectronic Properties of Bismuth Oxyiodide Robust against Percent-Level Iodine-, Oxygen-, and Bismuth-Related Surface Defects." In: *Advanced Functional Materials* 30.13 (2020), p. 1909983. DOI: 10.1002/adfm.201909983 (cited on page 21).

[116] R. L. Z. Hoye, L. C. Lee, R. C. Kurchin, T. N. Huq, K. H. L. Zhang, M. Sponseller, L. Nienhaus, R. E. Brandt, J. Jean, J. A. Polizzotti, A. Kursumović, M. G. Bawendi, V. Bulović, V. Stevanović, T. Buonassisi, and J. L. MacManus-Driscoll. "Strongly Enhanced Photovoltaic Performance and Defect Physics of Air-Stable Bismuth Oxyiodide (BiOI)." In: *Advanced Materials* 29.36 (2017), p. 1702176. DOI: 10.1002/adma.201702176 (cited on pages 21, 57, 63, 90).

[117] J. Singh. *Electronic and Optoelectronic Properties of Semiconductor Structures*. Cambridge: Cambridge University Press, 2003. DOI: 10.1017/CBO9780511805745 (cited on pages 21, 24).

[118] C. Hu. *Modern semiconductor devices for integrated circuits*. Vol. 2. Prentice Hall Upper Saddle River, NJ, 2010 (cited on page 21).

[119] J. Shah. *Ultrafast spectroscopy of semiconductors and semiconductor nanostructures*. Vol. 115. Springer Science & Business Media, 1996. DOI: 10.1007/978-3-662-03770-6 (cited on pages 22, 24, 25).

[120] W. Heitler. *The quantum theory of radiation*. Vol. 5. International Series of Monographs on Physics. Oxford: Oxford University Press, 1936 (cited on page 23).

[121] M. Fox. *Optical Properties of Solids*. 2nd ed. New York: Oxford University Press, 2010 (cited on pages 23, 28, 29, 32, 33).

[122] B. J. Bohn, T. Simon, M. Gramlich, A. F. Richter, L. Polavarapu, A. S. Urban, and J. Feldmann. "Dephasing and quantum beating of excitons in methylammonium lead iodide perovskite nanoplatelets." In: *ACS Photonics* 5.2 (2018), pp. 648–654. DOI: 10.1021/acsphotonics.7b01292 (cited on pages 24, 29).

[123] G. Moody, C. Kavir Dass, K. Hao, C.-H. Chen, L.-J. Li, A. Singh, K. Tran, G. Clark, X. Xu, G. Berghäuser, E. Malic, A. Knorr, and X. Li. "Intrinsic homogeneous linewidth and broadening mechanisms of excitons in monolayer transition metal dichalcogenides." In: *Nature Communications* 6.1 (2015), p. 8315. DOI: 10.1038/ncomms9315 (cited on page 24).

[124] V. A. Hintermayr, L. Polavarapu, A. S. Urban, and J. Feldmann. "Accelerated Carrier Relaxation through Reduced Coulomb Screening in Two-Dimensional Halide Perovskite Nanoplatelets." In: *ACS Nano* 12.10 (2018), pp. 10151–10158. DOI: 10.1021/acsnano.8b05029 (cited on pages 24, 25, 28, 30).

[125] M. B. Price, J. Butkus, T. C. Jellicoe, A. Sadhanala, A. Briane, J. E. Halpert, K. Broch, J. M. Hodgkiss, R. H. Friend, and F. Deschler. "Hot-carrier cooling and photoinduced refractive index changes in organic–inorganic lead halide perovskites." In: *Nature Communications* 6.1 (2015), p. 8420. DOI: 10.1038/ncomms9420 (cited on pages 24, 83).

[126] J. Shah. *Hot carriers in semiconductor nanostructures: Physics and applications*. Elsevier, 1992. DOI: 10.1016/C2009-0-22204-5 (cited on page 25).

[127] O. Flender, J. R. Klein, T. Lenzer, and K. Oum. "Ultrafast photoinduced dynamics of the organolead trihalide perovskite $CH_3NH_3PbI_3$ on mesoporous TiO_2 scaffolds in the 320–920 nm range." In: *Phys. Chem. Chem. Phys.* 17 (29 2015), pp. 19238–19246. DOI: 10.1039/C5CP01973G (cited on page 25).

[128] J. Feldmann, G. Peter, E. O. Göbel, P. Dawson, K. Moore, C. Foxon, and R. J. Elliott. "Linewidth dependence of radiative exciton lifetimes in quantum wells." In: *Phys. Rev. Lett.* 59.20 (1987), pp. 2337–2340. DOI: 10.1103/PhysRevLett.59.2337 (cited on page 25).

[129] B. Deveaud, F. Clérot, N. Roy, K. Satzke, B. Sermage, and D. S. Katzer. "Enhanced radiative recombination of free excitons in GaAs quantum wells." In: *Physical Review Letters* 67 (1991), pp. 2355–2358. DOI: 10.1103/PhysRevLett.67.2355 (cited on page 25).

[130] M. Gramlich, B. J. Bohn, Y. Tong, L. Polavarapu, J. Feldmann, and A. S. Urban. "Thickness-Dependence of Exciton–Exciton Annihilation in Halide Perovskite Nanoplatelets." In: *The Journal of Physical Chemistry Letters* 11.13 (2020), pp. 5361–5366. DOI: 10.1021/acs.jpclett.0c01291 (cited on pages 26, 61).

[131] S. Schmitt-Rink, D. Chemla, and D. Miller. "Linear and nonlinear optical properties of semiconductor quantum wells." In: *Advances in Physics* 38.2 (1989), pp. 89–188. DOI: 10.1080/00018738900101102 (cited on pages 26, 70).

[132] G. Dresselhaus. "Absorption Coefficients for Exciton Absorption Lines." In: *Phys. Rev.* 106.1 (1957), pp. 76–78. DOI: 10.1103/PhysRev.106.76 (cited on page 27).

[133] G. Dresselhaus. "Effective mass approximation for excitons." In: *Journal of Physics and Chemistry of Solids* 1.1 (1956), pp. 14–22. DOI: 10.1016/0022-3697(56)90004-X (cited on page 27).

[134] G. H. Wannier. "The Structure of Electronic Excitation Levels in Insulating Crystals." In: *Phys. Rev.* 52 (1937), pp. 191–197. DOI: 10.1103/PhysRev.52.191 (cited on page 27).

[135] T. Kazimierczuk, D. Fröhlich, S. Scheel, H. Stolz, and M. Bayer. "Giant Rydberg excitons in the copper oxide Cu2O." In: *Nature* 514.7522 (2014), pp. 343–347. DOI: 10.1038/nature13832 (cited on page 28).

[136] J. H. Davies. *The Physics of Low-dimensional Semiconductors: An Introduction*. Cambridge University Press, 1997. DOI: 10.1017/CBO9780511819070 (cited on pages 28, 30).

[137] J. Frenkel. "On the Transformation of light into Heat in Solids. I." In: *Phys. Rev.* 37 (1931), pp. 17–44. DOI: 10.1103/PhysRev.37.17 (cited on page 28).

[138] R. J. Elliott. "Intensity of Optical Absorption by Excitons." In: *Phys. Rev.* 108.6 (1957), pp. 1384–1389. DOI: 10.1103/PhysRev.108.1384 (cited on pages 29, 61).

[139] B. J. Bohn, Y. Tong, M. Gramlich, M. L. Lai, M. Döblinger, K. Wang, R. L. Z. Hoye, P. Müller-Buschbaum, S. D. Stranks, A. S. Urban, L. Polavarapu, and J. Feldmann. "Boosting Tunable Blue Luminescence of Halide Perovskite Nanoplatelets through Postsynthetic Surface Trap Repair." In: *Nano Letters* 18.8 (2018). PMID: 29990435, pp. 5231–5238. DOI: 10.1021/acs.nanolett.8b02190 (cited on pages 29, 61).

[140] M. Velický and P. S. Toth. "From two-dimensional materials to their heterostructures: An electrochemist's perspective." In: *Applied Materials Today* 8 (2017). 2D Materials in Electrochemistry, pp. 68–103. DOI: 10.1016/j.apmt.2017.05.003 (cited on page 30).

[141] V. A. Hintermayr, A. F. Richter, F. Ehrat, M. Döblinger, W. Vanderlinden, J. A. Sichert, Y. Tong, L. Polavarapu, J. Feldmann, and A. S. Urban. "Tuning the Optical Properties of Perovskite Nanoplatelets through Composition and Thickness by Ligand-Assisted Exfoliation." In: *Advanced Materials* 28.43 (2016), pp. 9478–9485. DOI: 10.1002/adma.201602897 (cited on page 30).

[142] J. A. Sichert, Y. Tong, N. Mutz, M. Vollmer, S. Fischer, K. Z. Milowska, R. García Cortadella, B. Nickel, C. Cardenas-Daw, J. K. Stolarczyk, A. S. Urban, and J. Feldmann. "Quantum Size Effect in Organometal Halide Perovskite Nanoplatelets." In: *Nano Letters* 15.10 (2015). PMID: 26327242, pp. 6521–6527. DOI: 10.1021/acs.nanolett.5b02985 (cited on pages 30, 61).

[143] U. B. R. v. Baltz. "Polaronen." In: *Madelung O. (eds) Festkörperprobleme 12. Advances in Solid State Physics*. Vol. 12. Berlin, Heidelberg: Springer, 1972. DOI: 10.1007/BFb0107703 (cited on pages 32, 86).

[144] J. M. Ziman. *Principles of the Theory of Solids*. 2nd ed. Cambridge: Cambridge University Press, 1972. DOI: 10.1017/CBO9781139644075 (cited on pages 32, 86).

[145] G. Tang, L. Zhang, and J. Wang. "Thermal rectification in a double quantum dots system with a polaron effect." In: *Phys. Rev. B* 97.22 (2018), p. 224311. DOI: 10.1103/PhysRevB.97.224311 (cited on pages 32, 86).

[146] O. Madelung. *Semiconductors - basic data*. 2nd ed. Springer, 1996. DOI: 10.1007/978-3-642-97675-9 (cited on pages 32, 33).

[147] T. Itoh, M. Nishijima, A. I. Ekimov, C. Gourdon, A. L. Efros, and M. Rosen. "Polaron and Exciton-Phonon Complexes in CuCl Nanocrystals." In: *Physical Review Letters* 74.9 (1995), pp. 1645–1648. DOI: 10.1103/PhysRevLett.74.1645 (cited on page 33).

[148] J. Appel. "Polarons." In: *Solid State Physics*. Ed. by F. Seitz, D. Turnbull, and H. Ehrenreich. Vol. 21. Academic Press, 1968, pp. 193–391. DOI: 10.1016/S0081-1947(08)60741-9 (cited on page 33).

[149] G. D. Mahan and J. J. Hopfield. "Piezoelectric Polaron Effects in CdS." In: *Physical Review Letters* 12.10 (1964), pp. 241–243. DOI: 10.1103/PhysRevLett.12.241 (cited on page 33).

[150] I. Austin and N. Mott. "Polarons in crystalline and non-crystalline materials." In: *Advances in Physics* 18.71 (1969), pp. 41–102. DOI: 10.1080/00018736900101267 (cited on pages 33, 84, 86).

[151] L. P. R. de Cotret, M. R. Otto, J.-H. Pöhls, Z. Luo, M. G. Kanatzidis, and B. J. Siwick. "Direct visualization of polaron formation in the thermoelectric SnSe." In: *Proceedings of the National Academy of Sciences* 119.3 (2022), e2113967119. DOI: 10.1073/pnas.2113967119 (cited on pages 33, 84).

[152] K. Miyata, T. L. Atallah, and X.-Y. Zhu. "Lead halide perovskites: Crystal-liquid duality, phonon glass electron crystals, and large polaron formation." In: *Science Advances* 3.10 (2017), e1701469. DOI: doi:10.1126/sciadv.1701469 (cited on page 33).

[153] L.-C. Ku and S. A. Trugman. "Quantum dynamics of polaron formation." In: *Phys. Rev. B* 75.1 (2007), p. 014307. DOI: 10.1103/PhysRevB.75.014307 (cited on pages 33, 85, 86).

[154] M. Hase, K. Mizoguchi, H. Harima, S.-i. Nakashima, and K. Sakai. "Dynamics of coherent phonons in bismuth generated by ultrashort laser pulses." In: *Phys. Rev. B* 58.9 (1998), pp. 5448–5452. DOI: 10.1103/PhysRevB.58.5448 (cited on pages 34, 39, 74).

[155] O. V. Misochko. "Coherent phonons and their properties." In: *Journal of Experimental and Theoretical Physics* 92.2 (2001), pp. 246–259. DOI: 10.1134/1.1354682 (cited on page 34).

[156] X. Hu and F. Nori. "Quantum phonon optics: Coherent and squeezed atomic displacements." In: *Physical Review B* 53.5 (1996), pp. 2419–2424. DOI: 10.1103/PhysRevB.53.2419 (cited on page 34).

[157] R. J. Glauber. "Coherent and Incoherent States of the Radiation Field." In: *Physical Review* 131.6 (1963), pp. 2766–2788. DOI: 10.1103/PhysRev.131.2766 (cited on page 34).

[158] K. Ishioka and O. V. Misochko. "Coherent Lattice Oscillations in Solids and Their Optical Control." In: *Progress in Ultrafast Intense Laser Science: Volume V*. Ed. by K. Yamanouchi, A. Giulietti, and K. Ledingham. Berlin, Heidelberg: Springer Berlin Heidelberg, 2010, pp. 47–63. DOI: 10.1007/978-3-642-03825-9_3 (cited on pages 34–36, 74).

[159] T. Dekorsy, G. C. Cho, and H. Kurz. "Coherent phonons in condensed media." In: *Light Scattering in Solids VIII: Fullerenes, Semiconductor Surfaces, Coherent Phonons*. Ed. by M. Cardona and G. Güntherodt. Berlin, Heidelberg: Springer Berlin Heidelberg, 2000, pp. 169–209. DOI: 10.1007/BFb0084242 (cited on pages 34, 40, 74).

[160] M. Hase, K. Mizoguchi, H. Harima, S. Nakashima, M. Tani, K. Sakai, and M. Hangyo. "Optical control of coherent optical phonons in bismuth films." In: *Applied Physics Letters* 69.17 (1996), pp. 2474–2476. DOI: 10.1063/1.117502 (cited on pages 34, 74).

[161] M. Först and T. Dekorsy. "Coherent phonons in bulk and low-dimensional semiconductors." In: *Coherent Vibrational Dynamics*. Ed. by S. De Silvestri. Boca Raton: CRC Press, 2008, pp. 129–172. DOI: 10.1201/9781420017519 (cited on pages 34, 40).

[162] J. H. Kim, A. R. T. Nugraha, L. G. Booshehri, E. H. Hároz, K. Sato, G. D. Sanders, K. J. Yee, Y. S. Lim, C. J. Stanton, R. Saito, and J. Kono. "Coherent phonons in carbon nanotubes and graphene." In: *Chemical Physics* 413 (2013), pp. 55–80. DOI: 10.1016/j.chemphys.2012.09.017 (cited on page 34).

[163] G. C. Cho, W. Kütt, and H. Kurz. "Subpicosecond time-resolved coherent-phonon oscillations in GaAs." In: *Physical Review Letters* 65.6 (1990), pp. 764–766. DOI: 10.1103/PhysRevLett.65.764 (cited on pages 35, 78).

[164] S. De Silvestri, J. G. Fujimoto, E. P. Ippen, E. B. Gamble, L. R. Williams, and K. A. Nelson. "Femtosecond time-resolved measurements of optic phonon dephasing by impulsive stimulated raman scattering in α-perylene crystal from 20 to 300 K." In: *Chemical Physics Letters* 116.2 (1985), pp. 146–152. DOI: 10.1016/0009-2614(85)80143-3 (cited on page 35).

[165] R. Merlin. "Generating coherent THz phonons with light pulses." In: *Solid State Communications* 102.2 (1997). Highlights in Condensed Matter Physics and Materials Science, pp. 207–220. DOI: 10.1016/S0038-1098(96)00721-1 (cited on page 35).

[166] M. F. DeCamp, D. A. Reis, P. H. Bucksbaum, and R. Merlin. "Dynamics and coherent control of high-amplitude optical phonons in bismuth." In: *Phys. Rev. B* 64.9 (2001), p. 092301. DOI: 10.1103/PhysRevB.64.092301 (cited on pages 35, 73).

[167] T. Dekorsy, H. Auer, C. Waschke, H. J. Bakker, H. G. Roskos, H. Kurz, V. Wagner, and P. Grosse. "Emission of submillimeter electromagnetic waves by coherent phonons." In: *Physical Review Letters* 74.5 (1995), p. 738. DOI: 10.1103/PhysRevLett.74.738 (cited on pages 36, 40, 78).

[168] T. Dekorsky, W. Kütt, T. Pfeifer, and H. Kurz. "Coherent Control of LO-Phonon Dynamics in Opaque Semiconductors by Femtosecond Laser Pulses." In: *Europhysics Letters (EPL)* 23.3 (1993), pp. 223–228. DOI: 10.1209/0295-5075/23/3/011 (cited on pages 36, 40).

[169] T. Debnath, D. Sarker, H. Huang, Z.-K. Han, A. Dey, L. Polavarapu, S. V. Levchenko, and J. Feldmann. "Coherent vibrational dynamics reveals lattice anharmonicity in organic–inorganic halide perovskite nanocrystals." In: *Nature Communications* 12.1 (2021), p. 2629. DOI: 10.1038/s41467-021-22934-2 (cited on page 36).

[170] M. Born and R. Oppenheimer. "Zur Quantentheorie der Molekeln." In: *Annalen der Physik* 389.20 (1927), pp. 457–484. DOI: 10.1002/andp.19273892002 (cited on pages 36, 75).

[171] M. W. Graham, Y.-Z. Ma, A. A. Green, M. C. Hersam, and G. R. Fleming. "Pure optical dephasing dynamics in semiconducting single-walled carbon nanotubes." In: 134.3 (2011), p. 034504. DOI: 10.1063/1.3530582 (cited on page 36).

[172] P. G. Klemens. "Anharmonic Decay of Optical Phonons." In: *Phys. Rev.* 148.2 (1966), pp. 845–848. DOI: 10.1103/PhysRev.148.845 (cited on pages 37, 38, 77).

[173] F. Vallée and F. Bogani. "Coherent time-resolved investigation of LO-phonon dynamics in GaAs." In: *Phys. Rev. B* 43.14 (1991), pp. 12049–12052. DOI: 10.1103/PhysRevB.43.12049 (cited on pages 37, 77).

[174] S. Barman and G. P. Srivastava. "Long-wavelength nonequilibrium optical phonon dynamics in cubic and hexagonal semiconductors." In: *Phys. Rev. B* 69.23 (2004), p. 235208. DOI: 10.1103/PhysRevB.69.235208 (cited on pages 37, 77).

[175] B. K. Ridley. "The LO phonon lifetime in GaN." In: *Journal of Physics: Condensed Matter* 8.37 (1996), pp. L511–L513. DOI: 10.1088/0953-8984/8/37/001 (cited on pages 37, 77).

[176] M. Balkanski, R. F. Wallis, and E. Haro. "Anharmonic effects in light scattering due to optical phonons in silicon." In: *Phys. Rev. B* 28.4 (1983), pp. 1928–1934. DOI: 10.1103/PhysRevB.28.1928 (cited on pages 38, 77).

[177] P. Němec and P. Malý. "Temperature dependence of coherent phonon dephasing in $CsPbCl_3$ nanocrystals." In: *Phys. Rev. B* 72.23 (2005), p. 235324. DOI: 10.1103/PhysRevB.72.235324 (cited on pages 38, 77, 78).

[178] P. Verma, S. C. Abbi, and K. P. Jain. "Raman-scattering probe of anharmonic effects in GaAs." In: *Phys. Rev. B* 51.23 (1995), pp. 16660–16667. DOI: 10.1103/PhysRevB.51.16660 (cited on pages 38, 77).

[179] T. R. Hart, R. L. Aggarwal, and B. Lax. "Temperature Dependence of Raman Scattering in Silicon." In: *Phys. Rev. B* 1.2 (1970), pp. 638–642. DOI: 10.1103/PhysRevB.1.638 (cited on pages 38, 77).

[180] D. T. Morelli, T. M. Hartnett, and C. J. Robinson. "Phonon-defect scattering in high thermal conductivity diamond films." In: *Applied Physics Letters* 59.17 (1991), pp. 2112–2114. DOI: 10.1063/1.106096 (cited on page 39).

[181] M. Hase, K. Ishioka, M. Kitajima, K. Ushida, and S. Hishita. "Dephasing of coherent phonons by lattice defects in bismuth films." In: *Applied Physics Letters* 76.10 (2000), pp. 1258–1260. DOI: 10.1063/1.126002 (cited on page 39).

[182] L. N. Cooper. "Bound Electron Pairs in a Degenerate Fermi Gas." In: *Phys. Rev.* 104.4 (1956), pp. 1189–1190. DOI: 10.1103/PhysRev.104.1189 (cited on page 40).

[183] H. Dember. "Photoelectromotive force in cuprous oxide crystals." In: *Phys. Z* 32.1 (1995), pp. 554–556 (cited on page 40).

[184] T. Dekorsy, T. Pfeifer, W. Kütt, and H. Kurz. "Subpicosecond carrier transport in GaAs surface-space-charge fields." In: *Phys. Rev. B* 47.7 (1993), pp. 3842–3849. DOI: 10.1103/PhysRevB.47.3842 (cited on page 40).

[185] F. Haaf, A. Sanner, and F. Straub. "Polymers of N-vinylpyrrolidone: synthesis, characterization and uses." In: *Polymer Journal* 17.1 (1985), pp. 143–152. DOI: 10.1295/polymj.17.143 (cited on page 42).

[186] E. Abbe. "Beiträge zur Theorie des Mikroskops und der mikroskopischen Wahrnehmung." In: *Archiv für Mikroskopische Anatomie* 9.1 (1873), pp. 413–468. DOI: 10.1007/BF02956173 (cited on page 43).

[187] A. Lipson, S. G. Lipson, and H. Lipson. *Optical Physics*. 4th ed. Cambridge University Press, 2010. DOI: 10.1017/CBO9780511763120 (cited on page 43).

[188] D. B. Williams and C. B. Carter. *Transmission Electron Microscopy*. Boston: Plenum, 1996. DOI: 10.1007/978-1-4757-2519-3 (cited on page 44).

[189] P. Hirsch. *Electron Microscopy of Thin Crystals*. Washington: Butterworths, 1965 (cited on page 44).

[190] N. Yao and Z. L. Wang. *Handbook of microscopy for nanotechnology*. 1st ed. Boston, MA: Springer, 2005. DOI: 10.1007/1-4020-8006-9 (cited on page 45).

[191] M. S. Kandanapitiye, M. Gao, J. Molter, C. A. Flask, and S. D. Huang. "Synthesis, Characterization, and X-ray Attenuation Properties of Ultrasmall BiOI Nanoparticles: Toward Renal Clearable Particulate CT Contrast Agents." In: *Inorganic Chemistry* 53.19 (2014). PMID: 25283335, pp. 10189–10194. DOI: 10.1021/ic5011709 (cited on pages 46, 59).

[192] D. Strickland and G. Mourou. "Compression of amplified chirped optical pulses." In: *Optics Communications* 55.6 (1985), pp. 447–449. DOI: 10.1016/0030-4018(85)90151-8 (cited on page 51).

[193] The Royal Swedish Academy of Sciences. *Press release: The Nobel Prize in Physics 2018*. https://www.nobelprize.org/prizes/physics/2018/press-release/, visited on 03/04/2022 (cited on page 51).

[194] B. J. Bohn. *Exciton Dynamics in Lead Halide Perovskite Nanocrystals: Recombination, Dephasing and Diffusion*. Springer Nature, 2021 (cited on page 52).

[195] R. A. Jagt, T. N. Huq, K. M. Börsig, D. Sauven, L. C. Lee, J. L. MacManus-Driscoll, and R. L. Z. Hoye. "Controlling the preferred orientation of layered BiOI solar absorbers." In: *Journal of Materials Chemistry C* 8.31 (2020), pp. 10791–10797. DOI: 10.1039/D0TC02076A (cited on pages 57, 62).

[196] S. Rieger, S. Schönweitz, K. Frank, T. Fürmann, N. M. Kerschbaumer, V. Steidl, J. Fang, M. Döblinger, B. Nickel, J. K. Stolarczyk, and J. Feldmann. "Anisotropic polarons and self-trapping in bismuth oxyiodide (BiOI) nanoplatelets." In: (2022). in preparation (cited on pages 57, 81).

[197] M. G. L. Gustafsson. "Surpassing the lateral resolution limit by a factor of two using structured illumination microscopy." In: *Journal of Microscopy* 198.2 (2000), pp. 82–87. DOI: 10.1046/j.1365-2818.2000.00710.x (cited on page 58).

[198] Z.-Y. Zhao and W.-W. Dai. "Electronic Structure and Optical Properties of BiOI Ultrathin Films for Photocatalytic Water Splitting." In: *Inorganic Chemistry* 54.22 (2015). PMID: 26513342, pp. 10732–10737. DOI: 10.1021/acs.inorgchem.5b01714 (cited on page 58).

[199] K. M. Koczkur, S. Mourdikoudis, L. Polavarapu, and S. E. Skrabalak. "Polyvinylpyrrolidone (PVP) in nanoparticle synthesis." In: *Dalton Trans.* 44 (41 2015), pp. 17883–17905. DOI: 10.1039/C5DT02964C (cited on page 58).

[200] S. Ithurria, M. D. Tessier, B. Mahler, R. P. S. M. Lobo, B. Dubertret, and A. L. Efros. "Colloidal nanoplatelets with two-dimensional electronic structure." In: *Nature Materials* 10.12 (2011), pp. 936–941. DOI: 10.1038/nmat3145 (cited on page 61).

[201] P. Umari, E. Mosconi, and F. De Angelis. "Infrared Dielectric Screening Determines the Low Exciton Binding Energy of Metal-Halide Perovskites." In: *The Journal of Physical Chemistry Letters* 9.3 (2018). PMID: 29336156, pp. 620–627. DOI: 10.1021/acs.jpclett.7b03286 (cited on page 64).

[202] S. V. Gaponenko. *Optical Properties of Semiconductor Nanocrystals*. Cambridge Studies in Modern Optics. Cambridge University Press, 1998. DOI: 10.1017/CBO9780511524141 (cited on page 64).

[203] R. Li, F. Zhang, D. Wang, J. Yang, M. Li, J. Zhu, X. Zhou, H. Han, and C. Li. "Spatial separation of photogenerated electrons and holes among {010} and {110} crystal facets of $BiVO_4$." In: *Nature Communications* 4.1 (2013), p. 1432. DOI: 10.1038/ncomms2401 (cited on page 67).

[204] R. A. Kaindl, M. A. Carnahan, D. Hägele, R. Lövenich, and D. S. Chemla. "Ultrafast terahertz probes of transient conducting and insulating phases in an electron–hole gas." In: *Nature* 423.6941 (2003), pp. 734–738. DOI: 10.1038/nature01676 (cited on page 67).

[205] C. Sah, R. N. Noyce, and W. Shockley. "Carrier Generation and Recombination in P-N Junctions and P-N Junction Characteristics." In: *Proceedings of the IRE* 45.9 (1957), pp. 1228–1243. DOI: 10.1109/JRPROC.1957.278528 (cited on page 67).

[206] M. Liu, M. B. Johnston, and H. J. Snaith. "Efficient planar heterojunction perovskite solar cells by vapour deposition." In: *Nature* 501.7467 (2013), pp. 395–398. DOI: 10.1038/nature12509 (cited on page 67).

[207] K. L. Chopra, P. D. Paulson, and V. Dutta. "Thin-film solar cells: an overview." In: *Progress in Photovoltaics: Research and Applications* 12.2-3 (2004), pp. 69–92. DOI: 10.1002/pip.541 (cited on page 67).

[208] Y. Zhang and Z. Jin. "Effective electron–hole separation over a controllably constructed WP/UiO-66/CdS heterojunction to achieve efficiently improved visible-light-driven photocatalytic hydrogen evolution." In: *Physical Chemistry Chemical Physics* 21.16 (2019), pp. 8326–8341. DOI: 10.1039/C9CP01180C (cited on page 67).

[209] W. Ouyang, F. Teng, and X. Fang. "High Performance BiOCl Nanosheets/TiO_2 Nanotube Arrays Heterojunction UV Photodetector: The Influences of Self-Induced Inner Electric Fields in the BiOCl Nanosheets." In: *Advanced Functional Materials* 28.16 (2018), p. 1707178. DOI: 10.1002/adfm.201707178 (cited on page 67).

[210] Y. Guo, W. Shi, Y. Zhu, Y. Xu, and F. Cui. "Enhanced photoactivity and oxidizing ability simultaneously via internal electric field and valence band position by crystal structure of bismuth oxyiodide." In: *Applied Catalysis B: Environmental* 262 (2020), p. 118262. DOI: 10.1016/j.apcatb.2019.118262 (cited on page 67).

[211] J. Li, H. Li, G. Zhan, and L. Zhang. "Solar Water Splitting and Nitrogen Fixation with Layered Bismuth Oxyhalides." In: *Accounts of Chemical Research* 50.1 (2017), pp. 112–121. DOI: 10.1021/acs.accounts.6b00523 (cited on page 67).

[212] Z.-K. Tang, W.-J. Yin, Z. Le, B. Wen, D.-Y. Zhang, L.-M. Liu, and W.-M. Lau. "Spatial separation of photo-generated electron-hole pairs in BiOBr/BiOI bilayer to facilitate water splitting." In: *Scientific Reports* 6.1 (2016), p. 32764. DOI: 10.1038/srep32764 (cited on page 67).

[213] X. Jin, L. Ye, H. Xie, and G. Chen. "Bismuth-rich bismuth oxyhalides for environmental and energy photocatalysis." In: *Coordination Chemistry Reviews* 349 (2017), pp. 84–101. DOI: 10.1016/j.ccr.2017.08.010 (cited on page 67).

[214] K. Sharma, V. Dutta, S. Sharma, P. Raizada, A. Hosseini-Bandegharaei, P. Thakur, and P. Singh. "Recent advances in enhanced photocatalytic activity of bismuth oxyhalides for efficient photocatalysis of organic pollutants in water: A review." In: *Journal of Industrial and Engineering Chemistry* 78 (2019), pp. 1–20. DOI: 10.1016/j.jiec.2019.06.022 (cited on page 67).

[215] Z. Lou, P. Wang, B. Huang, Y. Dai, X. Qin, X. Zhang, Z. Wang, and Y. Liu. "Enhancing Charge Separation in Photocatalysts with Internal Polar Electric Fields." In: *ChemPhotoChem* 1.5 (2017), pp. 136–147. DOI: 10.1002/cptc.201600057 (cited on page 67).

[216] S. Shenawi-Khalil, V. Uvarov, Y. Kritsman, E. Menes, I. Popov, and Y. Sasson. "A new family of BiO(Cl_xBr_{1-x}) visible light sensitive photocatalysts." In: *Catalysis Communications* 12.12 (2011), pp. 1136–1141. DOI: 10.1016/j.catcom.2011.03.014 (cited on page 67).

[217] Z. Fu and M. Yamaguchi. "Coherent excitation of optical phonons in GaAs by broadband terahertz pulses." In: *Scientific Reports* 6 (2016), p. 38264. DOI: 10.1038/srep38264 (cited on pages 67, 78).

[218] D. K. Ferry. "Non-equilibrium longitudinal optical phonons and their lifetimes." In: *Applied Physics Reviews* 8.2 (2021), p. 021324. DOI: 10.1063/5.0044374 (cited on page 67).

[219] R. Liu, G. D. Sanders, C. J. Stanton, C. S. Kim, J. S. Yahng, Y. D. Jho, K. J. Yee, E. Oh, and D. S. Kim. "Femtosecond pump-probe spectroscopy of propagating coherent acoustic phonons in $In_xGa_{1-x}N$/GaN heterostructures." In: *Physical Review B* 72.19 (2005), p. 195335. DOI: 10.1103/PhysRevB.72.195335 (cited on page 67).

[220] S. Rieger, T. Fürmann, J. K. Stolarczyk, and J. Feldmann. "Optically Induced Coherent Phonons in Bismuth Oxyiodide (BiOI) Nanoplatelets." In: *Nano Letters* 21.18 (2021), pp. 7887–7893. DOI: 10.1021/acs.nanolett.1c00530 (cited on pages 67, 81, 82, 84).

[221] S. Hunsche, K. Wienecke, T. Dekorsy, and H. Kurz. "Impulsive Softening of Coherent Phonons in Tellurium." In: *Physical Review Letters* 75.9 (1995), pp. 1815–1818. DOI: 10.1103/PhysRevLett.75.1815 (cited on page 73).

[222] D. M. Fritz, D. A. Reis, B. Adams, R. A. Akre, J. Arthur, C. Blome, P. H. Bucksbaum, A. L. Cavalieri, S. Engemann, S. Fahy, R. W. Falcone, P. H. Fuoss, K. J. Gaffney, M. J. George, J. Hajdu, M. P. Hertlein, P. B. Hillyard, M. H.-v. Hoegen, M. Kammler, J. Kaspar, R. Kienberger, Krejci., M. Nicoul, R. Pahl, J. Rudati, H. Schlarb, D. P. Siddons, K. Sokolowski-Tinten, T. Tschentscher, D. v. d. Linde, and J. B. Hastings. "Ultrafast Bond Softening in Bismuth: Mapping a Solid's Interatomic Potential with X-rays." In: *Science* 315.5812 (2007), pp. 633–636. DOI: 10.1126/science.1135009 (cited on page 73).

[223] S. Dong, J. Lian, M. H. Jhon, Y. Chan, and Z.-H. Loh. "Pump-Power Dependence of Coherent Acoustic Phonon Frequencies in Colloidal CdSe/CdS Core/Shell Nanoplatelets." In: *Nano Letters* 17.5 (2017), pp. 3312–3319. DOI: 10.1021/acs.nanolett.7b01394 (cited on page 73).

[224] D. A. B. Miller, D. S. Chemla, T. C. Damen, A. C. Gossard, W. Wiegmann, T. H. Wood, and C. A. Burrus. "Band-Edge Electroabsorption in Quantum Well Structures: The Quantum-Confined Stark Effect." In: *Phys. Rev. Lett.* 53.22 (1984), pp. 2173–2176. DOI: 10.1103/PhysRevLett.53.2173 (cited on page 75).

[225] W. Franz. "Einfluß eines elektrischen Feldes auf eine optische Absorptionskante." In: *Zeitschrift für Naturforschung A* 13.6 (1958), pp. 484–489. DOI: doi:10.1515/zna-1958-0609 (cited on page 75).

[226] L. Keldysh. "Behavior of non-metallic crystals in strong electric fields." In: *Soviet Journal of Experimental and Theoretical Physics* 6 (1958), p. 763 (cited on page 75).

[227] S. Gélinas, A. Rao, A. Kumar, S. L. Smith, A. W. Chin, J. Clark, T. S. van der Poll, G. C. Bazan, and R. H. Friend. "Ultrafast Long-Range Charge Separation in Organic Semiconductor Photovoltaic Diodes." In: *Science* 343.6170 (2014), pp. 512–516. DOI: 10.1126/science.1246249 (cited on page 76).

[228] W. H. Knox, D. S. Chemla, D. A. B. Miller, J. B. Stark, and S. Schmitt-Rink. "Femtosecond ac Stark effect in semiconductor quantum wells: Extreme low- and high-intensity limits." In: *Phys. Rev. Lett.* 62.10 (1989), pp. 1189–1192. DOI: 10.1103/PhysRevLett.62.1189 (cited on pages 76, 83, 84).

[229] Y. Yang, M. Yang, K. Zhu, J. C. Johnson, J. J. Berry, J. van de Lagemaat, and M. C. Beard. "Large polarization-dependent exciton optical Stark effect in lead iodide perovskites." In: *Nature Communications* 7 (2016), p. 12613. DOI: 10.1038/ncomms12613 (cited on page 76).

[230] F. Cerdeira, C. Vázquez-López, E. Ribeiro, P. A. M. Rodrigues, V. Lemos, M. A. Sacilotti, and A. P. Roth. "Franz-Keldysh oscillations in the photomodulated spectra of an $In_{0.12}Ga_{0.88}As/GaAs$ strained-layer superlattice." In: *Phys. Rev. B* 42 (15 1990), pp. 9480–9485. DOI: 10.1103/PhysRevB.42.9480 (cited on page 76).

[231] E. Garmire. "Optical Nonlinearities in Semiconductors Enhanced by Carrier Transport." In: *Nonlinear Optics in Semiconductors I*. Ed. by E. Garmire and A. Kost. Vol. 58. Semiconductors and Semimetals. Elsevier, 1998, pp. 55–173. DOI: 10.1016/S0080-8784(08)62721-0 (cited on page 76).

[232] M. Hase, K. Ushida, and M. Kitajima. "Anharmonic Decay of Coherent Optical Phonons in Antimony." In: *Journal of the Physical Society of Japan* 84.2 (2015), p. 024708. DOI: 10.7566/JPSJ.84.024708 (cited on page 78).

[233] J. M. Chwalek, C. Uher, J. F. Whitaker, G. A. Mourou, and J. A. Agostinelli. "Subpicosecond time-resolved studies of coherent phonon oscillations in thin-film $YBa_2Cu_3O_{6+x}$ (x<0.4)." In: *Applied Physics Letters* 58.9 (1991), pp. 980–982. DOI: 10.1063/1.104462 (cited on page 78).

[234] J. Butkus, P. Vashishtha, K. Chen, J. K. Gallaher, S. K. K. Prasad, D. Z. Metin, G. Laufersky, N. Gaston, J. E. Halpert, and J. M. Hodgkiss. "The Evolution of Quantum Confinement in $CsPbBr_3$ Perovskite Nanocrystals." In: *Chemistry of Materials* 29.8 (2017), pp. 3644–3652. DOI: 10.1021/acs.chemmater.7b00478 (cited on page 83).

[235] L. D. Landau. "Electron motion in crystal lattices." In: *Sov Phys J* 3 (1933), p. 664 (cited on pages 83, 86).

[236] J. I. Frenkel. "On the absorption of light and the trapping of electrons and positive holes in crystalline dielectrics." In: *Sov Phys J* 9 (1936), p. 158 (cited on page 83).

[237] E. A. Muljarov and S. G. Tikhodeev. "Self-Trapped Excitons in Semiconductor Quantum Wires Inside a Polar Dielectric Matrix." In: 164.1 (1997), pp. 393–396. DOI: 10.1002/1521-396X(199711)164:1<393::AID-PSSA393>3.0.CO;2-H (cited on page 83).

[238] F. Zheng and L.-W. Wang. "Large polaron formation and its effect on electron transport in hybrid perovskites." In: *Energy & Environmental Science* 12.4 (2019), pp. 1219–1230. DOI: 10.1039/C8EE03369B (cited on page 84).

[239] R. Gross and A. Marx. *Festkörperphysik*. Berlin, Boston: De Gruyter, 2018. DOI: doi:10.1515/9783110559187 (cited on page 84).

[240] H. Sezen, H. Shang, F. Bebensee, C. Yang, M. Buchholz, A. Nefedov, S. Heissler, C. Carbogno, M. Scheffler, P. Rinke, and C. Wöll. "Evidence for photogenerated intermediate hole polarons in ZnO." In: *Nature Communications* 6.1 (2015), p. 6901. DOI: 10.1038/ncomms7901 (cited on page 84).

[241] A. Köhler and H. Bässler. *Electronic processes in organic semiconductors: An introduction*. John Wiley & Sons, 2015 (cited on pages 84, 86).

[242] A. Radoń, D. Łukowiec, and P. Włodarczyk. "Ultraslow electron-phonon scattering and polaron formation in magnetite." In: *Journal of Materiomics* 8.1 (2022), pp. 150–155. DOI: 10.1016/j.jmat.2021.04.008 (cited on page 84).

[243] D. Yakovlev. "Magnetic polaron formation in semimagnetic semiconductor heterostructures." In: *Acta Physica Polonica-Series A General Physics* 90.4 (1996), pp. 703–714. DOI: 10.12693/aphyspola.90.703 (cited on page 84).

[244] N. F. Mott and R. W. Gurney. *Electronic processes in ionic crystals*. Clarendon Press, 1948 (cited on page 86).

[245] A. Matsui, K. Mizuno, and M. Kobayashi. "Exciton Dynamics in Organic Molecular Crystals." In: *J. Phys. Colloques* 46.C7 (1985), pp. C7-19-C7–23. DOI: 10.1051/jphyscol:1985704 (cited on page 86).

[246] T. J. S. Evans, K. Miyata, P. P. Joshi, S. Maehrlein, F. Liu, and X. Y. Zhu. "Competition Between Hot-Electron Cooling and Large Polaron Screening in $CsPbBr_3$ Perovskite Single Crystals." In: *The Journal of Physical Chemistry C* 122.25 (2018), pp. 13724–13730. DOI: 10.1021/acs.jpcc.8b00476 (cited on page 87).

[247] G. Kaur, K. J. Babu, and H. N. Ghosh. "Temperature-Dependent Interplay of Polaron Formation and Hot Carrier Cooling Dynamics in $CsPbBr_3$ Nanocrystals: Role of Carrier–Phonon Coupling Strength." In: *The Journal of Physical Chemistry Letters* 11.15 (2020), pp. 6206–6213. DOI: 10.1021/acs.jpclett.0c01724 (cited on page 87).

List of Figures

List of Tables

List of Abbreviations

BBO	barium borate
CB	conduction band
CBM	conduction band minimum
CW	continuous-wave
DOS	density of states
HAADF	high angle annular dark field
NP	nanoplatelets
OD	optical density
OPA	optical parametric amplifier
PC	Pockels cell
PSF	phase-space filling
PVP	polyvinylpyrrodine
SEM	scanning electron microscopy
SHG	second harmonic generation
STEM	scanning transmission electron microscopy
TEM	transmission electron microscopy
UV	ultraviolet
VB	valence band
VBM	valence band maximum
WAXS	wide-angle X-ray scattering

Acknowledgments

First and foremost, I want to thank **Prof. Dr. Jochen Feldmann**. Thank you for all the fruitful discussions, your guidance during my time at your chair, the opportunity to work under such conditions as we have in the new Nano-Institute, and especially for never getting tired of pushing me into the right direction: In all our discussions you could always get to the bottom of our questions by taking a step back and seeing the bigger picture. I am deeply impressed by this quality, and I take these experiences with me as the possibly most valuable lesson from my time at your chair. I look back to challenging and essential years for my professional and personal development, for which I will always be grateful.

Prof. Dr. Jacek Stolarczyk: I am thankful for our time working together during my Master's and Ph.D. projects. Your support during such a long time was not only professionally but also personally enriching. Your immense expertise, especially your attention to detail and your ability to turn the worst sentence of any manuscript into the best one taught me a lot. I always enjoyed coming to your office, whether for scientific advice or trash talk. Most importantly though, I will remember you with your signature drink as the star of every (pre-Covid) PhOG Christmas party.

I thank **Dr. Lakshminarayana Polavarapu** for your guidance during my Master's project with your unique positive manner. That time motivated me to come back to the chair for my Ph.D.

PD Dr. Theobald *Pepper Jack* **Lohmüller**: I thank you for your huge support in the last years, all the Netflix-recommendations, entertaining stories and (not always constructive) fashion criticism.

My sincere thank goes to **Dr. Bernhard Bohn**, the most successful scientific 'Trittbrettfahrer' in the history of the chair. Since you started supporting me during my Master's project, you have become a role model, mentor and most importantly a great friend. Especially our time sharing an office in the Amalienstraße was 'meganice'.

I am thankful to **Tim Fürmann** and **Viola Steidl** for your impressive work in the chemistry lab and on the photocatalytic experiments which significantly contributed to this thesis. I always enjoyed working with you thanks to your friendly and straightforward manner.

Dr. Alexander Richter: I was so lucky to have you as a colleague when, in the first year of my Ph.D., I spent all that time with you in the lab desperately repairing, aligning, rebuilding, and moving lasers to the Nano-institute. There was not a single question ever that you could not answer. Thanks for being a great colleague and supporter.

I am thankful for all the great colleagues that I got to know during my Ph.D.: **Dr. Aurora Manzi**, **Dr. Stefanie Pritzl**, **Dr. Jiawen Fang**, **Simone Strohmair**, **Francis Schuknecht**, **Dr. Yiou Wang**, **Dr. Amrita Dey**, **Dr. Tushar Debnath**, **Ilka Vincon**, **Mariam Kurashvili**, **Philipp Bootz**, **Anja Barfüßer**, **Jinhua Zhang**, **Fei He**, **Matthias Kestler**, and many more.

Ina Flaucher, **Stefan Heiserer** and **Stephan Schönweitz**: It is always enriching to work with bright people, which is why I will keep our time working on your Master's projects in good memory. I truly enjoyed our collaboration on a professional and personal level.

Gerlinde Adam: Without your help, I would not have managed to handle even half of the administrative problems in my time at the chair. I will always stay thankful for your support, and I will keep repaying my debts through refrigerator magnets from my holidays.

Thank you, **Stefan Niedermaier** - your calm and efficient way of fixing any problem you can imagine saved me so much time and frustration during my time as a Ph.D. student.

Talee Barghouti: Thank you for your kind help with all my chemistry-related troubles.

I thank **Dr. Markus Döblinger** who provided the impressive high-resolution STEM images shown in this work.

I am thankful to **Kilian Frank** and **PD Dr. Bert Nickel** for the constructive and pleasant collaboration.

I sincerely thank **Jakob Lingg** for his constant support during my whole scientific career - from the very beginning until his input to this work.

To my work friend **Nicola Kerschbaumer**: In our time together as students and Ph.D. candidates, you became like family to me: both a grandmother and a much younger sister at the same time. Thank you for all the motivation, lunch walks, and coffee break discussions, for challenging me, and, most importantly, for a great time.

I cannot thank **Tanja** enough who was a part of this whole journey and brought so much music, great food, dancing, and joy to my life. Thank you for always inspiring and encouraging me.

Finally, I am deeply grateful to my mother **Barbara** and my brothers **Thomas** and **Christian** for your encouragement, motivation and giving me the confidence in myself and this work.